Localizing and Characterizing Cognitive Activity from Local Field Potentials in the Primate Prefrontal Cortex

Renée Johnston

THESIS SUBMITTED TO THE UNIVERSITY OF OTTAWA
IN PARTIAL FULFILMENT OF THE REQUIREMENTS FOR THE
DOCTORATE IN PHILOSOHPIY DEGREE
IN NEUROSCIENCE

DEPARTMENT OF NEUROSCIENCE
FACULTY OF MEDICINE
UNIVERSITY OF OTTAWA

© Renée Johnston, Ottawa, Canada, 2024

Ph. D. in Neuroscience (2024) University of Ottawa

Neuroscience Ottawa, Ontario, Canada

TITLE: Localizing and Characterizing Cognitive Activity from Local Field Potentials in the Primate Prefrontal Cortex

AUTHOR: Renée Johnston

M.A.Sc., Electrical University

Technical University of Nova Scotia

SUPERVISORS: Dr. Adam J. Sachs

NUMBER OF PAGES: 162

Abstract

For most of us, the seemingly mundane act of grabbing a glass, filling it with water, and quenching thirst is a task performed effortlessly. However, for individuals facing physical disabilities, this simple act can be impossible without the help of others. Despite remarkable technological advancements, such as robots using artificial intelligence to perform complex tasks, the potential to restore lost physical functions through brain-computer interface (BCI) systems remains an area demanding exploration.

Recent intracortical BCI investigations have predominantly examined the generation of movement from spiking activity within the motor and primary motor cortices, coupled with the stimulation of associated somatosensory areas. This approach holds the potential to facilitate functional electrical stimulation of muscles, empowering BCI users to command their limbs, therefore restoring lost connections. In contrast, this thesis investigates a different approach: identifying the goal of the BCI user directly from the prefrontal cortex. This intention could be used to control assistive devices, such as a robot arm, allowing them to choose the most suitable actions to complete the goal. Decoding cognitive functions from features based on local field potentials (LFPs), as opposed to single-unit spiking rate, will be explored and whenever possible utilized as these signals are considered more stable over time.

The success of a goal based BCI system depends on the quality and stability of the recorded signals from one or more implants. The recorded neural activity from small intracortical implants is contingent on the brain area they covered. The process of localizing and characterizing cognitive

activity associated with overarching goals before implantation holds the potential to assist in determining the most suitable location for a BCI implant.

This research first validates that LFPs from the prefrontal cortex can be used to decode important factors related to goals, such as saccade target locations and spatial positions. Furthermore, it introduces a methodology for localizing and characterizing cognitive activity, offering valuable insights for strategically planning optimal implant locations.

Résumé

Pour la plupart d'entre nous, l'acte apparemment banal de prendre un verre, de le remplir d'eau et d'étancher sa soif est une tâche accomplie sans effort. Cependant, pour les personnes souffrant d'un handicap physique, ce simple acte peut s'avérer impossible sans l'aide d'autrui. Malgré des avancées technologiques remarquables, telles que les robots utilisant l'intelligence artificielle pour effectuer des tâches complexes, la possibilité de restaurer les fonctions physiques perdues grâce à des systèmes d'interface cerveau-ordinateur (ICB) reste un domaine qui demande à être exploré.

Les recherches récentes sur l'ICB intracorticale ont principalement porté sur la génération de mouvements à partir de l'activité de pointes dans les cortex moteur et moteur primaire, associée à la stimulation des zones somatosensorielles associées. Cette approche pourrait faciliter la stimulation électrique fonctionnelle des muscles et permettre aux utilisateurs de l'ICB de commander leurs membres, rétablissant ainsi les connexions perdues. En revanche, cette thèse étudie une approche différente : l'identification de l'objectif de l'utilisateur de l'ICB directement à partir du cortex préfrontal. Cette intention pourrait être utilisée pour contrôler des appareils d'assistance, tels qu'un bras robotisé, en leur permettant de choisir les actions les plus appropriées pour atteindre l'objectif. Le décodage des fonctions cognitives à partir de caractéristiques basées sur les potentiels de champ locaux, par opposition au taux de stimulation d'une seule unité, sera exploré et, dans la mesure du possible, utilisé car ces signaux sont considérés comme plus stables dans le temps.

Le succès d'un système ICB basé sur l'objectif dépend de la qualité et de la stabilité des signaux enregistrés par un ou plusieurs implants. L'activité neuronale enregistrée à partir de petits implants

intracorticaux dépend de la zone cérébrale qu'ils couvrent. Le processus de localisation et de caractérisation de l'activité cognitive associée à des objectifs primordiaux avant l'implantation peut aider à déterminer l'emplacement le plus approprié pour un implant ICB.

Cette recherche valide d'abord que les potentiels de champ locaux du cortex préfrontal peuvent être utilisés pour décoder des facteurs importants liés aux objectifs, tels que les emplacements des cibles de saccades et les positions spatiales. En outre, elle introduit une méthodologie pour localiser et caractériser l'activité cognitive, offrant ainsi des informations précieuses pour planifier stratégiquement les emplacements optimaux des implants.

Acknowledgements

I would like to begin by expressing my gratitude to my supervisor, Dr. Adam Sachs, for his support and mentorship throughout my academic journey. Thank you for the invaluable opportunity to be a part of your lab and contribute to this esteemed university alongside exceptional professors. Your guidance and encouragement provided me with the confidence to navigate challenges and shape my research plan.

To my colleagues at the Sachs Lab, especially Dr. Chadwick Boulay and Dr. Guillaume Doucet, I extend my heartfelt thanks for dedicating extensive time to reviewing my work and consistently offering constructive feedback. Your mentorship has been invaluable, and I will forever remember and cherish the guidance you've provided.

I would like to express my sincere appreciation to Dr. Martinez-Trujillo at the Western University for the invaluable collaboration throughout this research endeavor. Your passion for research, expertise, and your valuable feedback on the manuscripts have significantly enriched the quality of my research.

Importantly, I am so grateful to my daughters Brielle and Abby, for your support throughout this journey. Your constant encouragement, patience, and love gave me the strength to face the challenges throughout the program. Your active participation in electroencephalography (EEG) testing, proofreading, and attentiveness during some of my presentation's rehearsals were instrumental in advancing my research. A significant portion of my achievement is attributable to you.

Finally, I want to address my heartfelt, deepest gratitude to my husband, Philippe, whose support has been the foundation of my PhD journey. Your understanding and encouragement made it possible for me to leave behind a stable career in the pursuit of my passion. Your generosity, positive attitude, beautiful energy, and confidence in me were instrumental throughout my graduate studies. I couldn't have done it without your love.

Contributions

This study demonstrated the possibility to decode saccade target intentions and spatial locations within a maze by utilizing local field potentials from the lateral prefrontal cortex of non-human primates. Considering that this region in macaques and humans share similar properties, our results suggest that this area could be a valuable implant location for a goal based intracortical brain-computer interface system used for spatial navigation in patients with disabilities.

Furthermore, a methodology was devised to explore and localize brain activity associated with cognitive functions recorded from various electrode types (EEG, sEEG, ECoG). This approach holds promise for identifying the optimal implant site that will yield valuable signals for decoding the user's overarching intention in a brain-computer interface system.

List of Peer-Reviewed Journal Articles

R. Johnston, G. Doucet, C. B. Boulay, K. Miller, J. C. Martinez-Trujillo, and A. J. Sachs. "**Decoding saccade intention from primate prefrontal cortical local field potentials using spectral, spatial, and temporal dimensionality reduction**", International Journal of Neural Systems, June 2021, doi:10.1142/S0129065721500234. **(Chapter 2)**

Author Contribution: Conceptualization - data collection, A.J.S.; writing (original draft), R.J., A.J.S.; data analysis, R.J., A.J.S.; figures, R.J. and G.D.; writing – review & editing, R.J., G.D., C.B.B, K.M, J.C.M., and A.J.S., supervision, A.J.S., J.C.M; funding acquisition, J.C.M.T. and A.J.S. Note that the thesis author was not involved with the conceptualization and data collection.

R. Johnston, M. Abbass, B. Corrigan, R. Gulli, J.C. Martinez-Trujillo, and A.J. Sachs, "**Decoding spatial locations from primate lateral prefrontal cortex neural activity during virtual navigation**", Journal of Neural Engineering, February 2023, doi:10.1088/1741-2552/acb5c2 **(Chapter 3)**

Author Contribution: Conceptualization - data collection, J.C.M, R.G., and B.C.; writing original, R.J.; data analysis, R.J., and M.A.; writing – review & editing, R.J., A.J.S. and J.C.M; supervision, A.J.S., J.C.M; funding acquisition, J.C.M.T. and A.J.S. Note that the thesis author was not involved with the conceptualization and data collection.

R. Johnston, C. B. Boulay, K. Miller, and A. J. Sachs. "**Mapping Cognitive Activity from Electrocorticography Local Field Potentials in Humans Performing NBack Task**", Submitted to Biomedical Physics and Engineering Express (May 2024). **(Chapter 5)**

Author Contribution: Conceptualization - data collection, K.M.; writing (original draft), R.J.; data analysis - methodology, R.J.; writing – review & editing, R.J., C.B.B, and A.J.S.; supervision, A.J.S.; funding acquisition, A.J.S. Note that the thesis author was not involved with the conceptualization and data collection.

Table of Contents

List of Figures

List of Tables

List of Abbreviations

ALS	Amyotrophic Lateral Sclerosis
BCI	Brain Computer Interface
CDA	Canonical Discriminant Analysis
CNS	Central Nervous System
dlPFC	Dorsolateral Prefrontal Cortex
DVA	Degrees of Visual Angle
EDF	European Data Format
FES	Functional Electrical Stimulation
ECoG	Electrocorticography
EEG	Electroencephalography
iBCI	Invasive Brain Computer Interface
FFT	Fast Fourier Transform
fMRI	Functional Magnetic Resonance Imaging
ICA	Independent Component Analysis
LFP	Local Field Potential
LPFC	Lateral Prefrontal Cortex
LSL	Labstreaming Layer
MEA	Microelectrode Array
MRI	Magnetic Resonance Imaging
NCC	Neuro-Cognitive Communicator
NHP	Non-Human Primate

OHRI	Ottawa Hospital Research Institute
PCA	Principal Component Analysis
PFC	Prefrontal Cortex
PSC1	First Principal Spectral Component
sec	seconds
sEEG	Stereo Electroencephalography
SID	Subset ID
SVM	Support Vector Machine
SWM	Spatial Working Memory
TID	Task ID
UI	User Interface
XDF	Extensible Data Format

Chapter 1

Background

1.1 Research Overview

Within the complex field of neuroscience, understanding where and how cognitive activity is decodable within the brain can lead to improvements or new developments of clinical applications. Controlling an assistive device by utilizing the overarching users' goals of a Brain Computer Interface (BCI) system has the potential to enhance their quality of life. While brain functions are distributed across various regions, the prefrontal cortex has reciprocal connections to many cortical and subcortical brain structures and is believed to play a key role in the day-to-day executive functions of primates' lives. Studying the complex patterns associated with cognitive activities, such as attention, working memory, movement planning, and decision-making, can deepen our knowledge on how factors linked to task goals can be used to decipher the overall intention. In this chapter, I will cover the fundamental themes of this thesis, providing essential context for a better understanding of the subsequent chapters.

The combined influence of movement intention and target location is pivotal in the functionality of current BCI systems. This thesis will demonstrate the potential to decode saccade intentions (Chapter 2) and to decode spatial locations within a maze (Chapter 3) from intracortical brain activity of the prefrontal cortex of macaques. Results from the analysis of brain activity from microelectrode arrays will show the possibility to successfully decode cognitive activity through the application of machine learning techniques.

In the context of BCI and other clinical mapping applications, the subsequent sections of this thesis will delineate how customized tasks can elicit detectable and locatable cognitive activity in humans. Chapter 4 will detail cognitive tasks and signal processing tools specifically crafted to explore brain activity synchronized with tasks events. The primary objective of performing this analysis is to decipher goal-encoding factors pertinent to the task. In the following chapter, the developed tools will be employed to validate this novel methodology for mapping cognitive activity from electrocorticography electrodes in humans engaged in a working memory task (Chapter 5).

1.2 Brain Computer Interface

1.2.1 Description

Physical impairments have significant impacts on affected individuals' quality of life including their independence, mobility, and control. Advancements in pharmacology, medical care, and adaptive computer technology are helpful but remain insufficient for people with advanced physical disabilities. Improvements in the communication assistive devices, enhancement in performance and energy efficiency of computers, refinement of surgical and medical procedures, coupled with a deeper understanding of the central nervous system (CNS), constitute key elements in supporting individuals that have lost the ability to move at will - a fundamental capability often taken for granted.

As defined by Wolpaw and Wolpaw. (2012), "A BCI is a system that measures central nervous system (CNS) activity and converts it into artificial output that replaces, restores, enhances, supplements, or improves natural CNS output and thereby changes the ongoing interactions

between the CNS and its external or internal environment." (Figure 1). The signals of brain activity can be acquired with various spatial and temporal resolutions, from indirect population signals integrated over millimeters and seconds, such as blood oxygen level dependent signals in functional magnetic resonance imaging (fMRI) (Sitaram et al. 2007), to directly measuring the electrical fluctuations of a single neuron's action potentials, over less than a millimeter and a

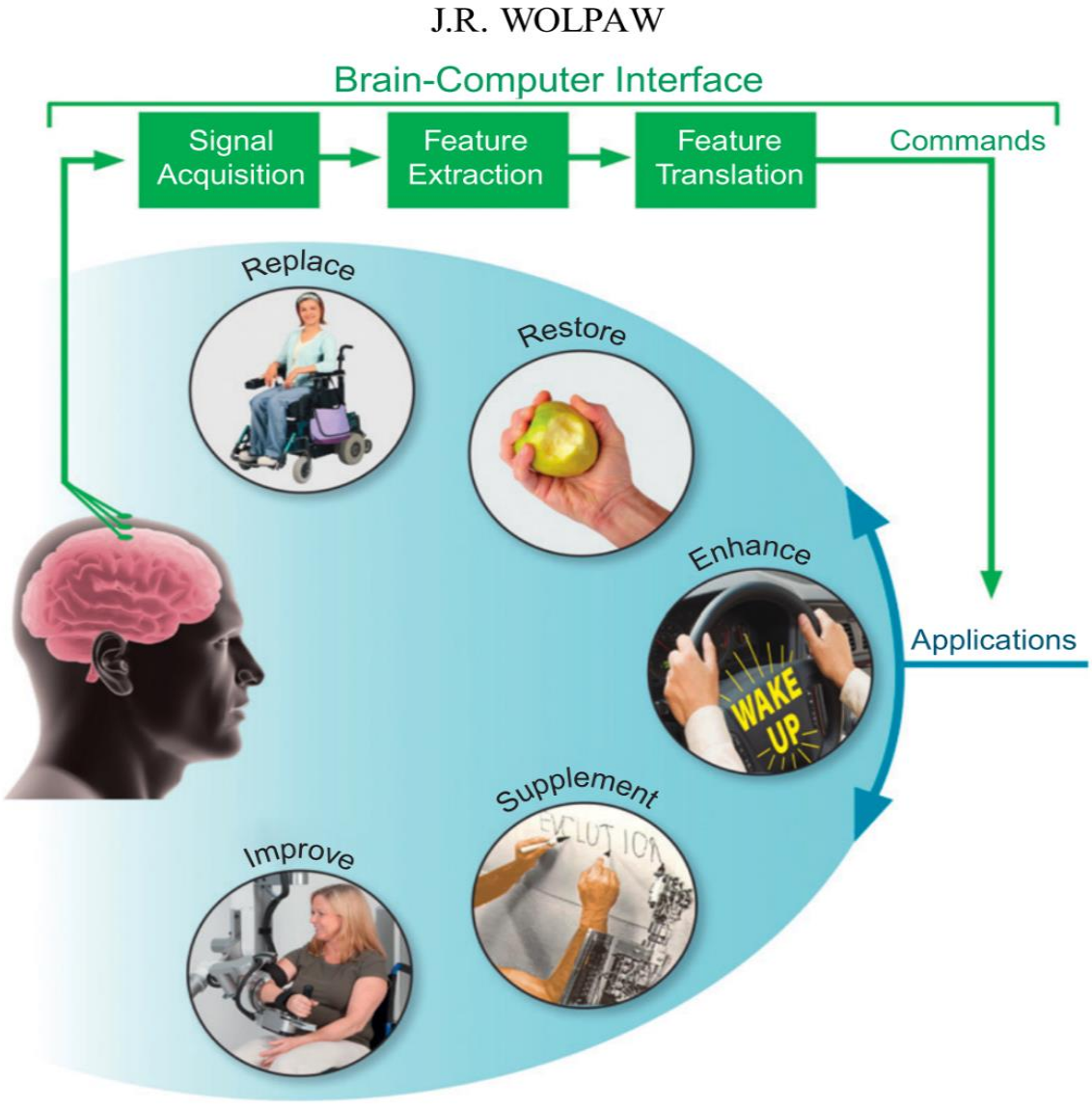

Figure 1. Brain Computer Interface schematic including five different categories of applications (Wolpaw and Wolpaw, 2012).

millisecond (Nam et al. 2018). Although the extracted features will vary across the different sources, all features can be translated into commands to be executed by an assistive device, with various performance and possible degrees of freedom.

Pandarinath et al. (2017) demonstrated the benefit of an intracortical BCI in assisting people with tetraplegia to restore communication. Using neural activity to control a computer cursor of an assistive communication device, three participants exceeded their typing rate and information throughput from previous invasive BCI (iBCI) tested in this context. During a testing period of three days, one of the participants could achieve a mean free typing rate of 24.4 correct characters per minute. The authors described this as "the highest typing rate to date by a person with a physical disability using a BCI". Since then, novel methods such as decoding the attempted handwriting movements from motor cortex activity, improved this brain-to-text typing rate (Willett 2021), with further advancements anticipated.

1.2.2 BCI Design, Applications, and Requirements

The main goals of a comprehensive BCI literature review from Kögel et al. (2019) were to look at the psycho-social, personal, and ethical aspects from the user's perspectives, to better understand future research requirements and relevance. It reported numerous applications of BCI, spanning from neurological rehabilitation following strokes, to communication, motor control, epilepsy treatment, and even incorporation into the gaming industry. The survey results showed that people with severe physical disabilities or patients with Amyotrophic Lateral Sclerosis (ALS; Kübler et al. 2005) would benefit from a well-designed BCI system, particularly if it is comfortable, user-friendly, and enhances their independence.

Another study to evaluate what individuals with spinal cord injury find important in BCI (Huggins et al. 2015) concluded that 96% of the low functional group (24 participants) are interested in BCI. Their top priority was for the interface to offer the following features: emergency communication, functions that meet their specific needs such as robotic control, achieving a desired speed of 20 letters per minute with 90% accuracy, and a straightforward setup process lasting approximately 10-20 minutes. From that survey, less than 50% of the low functional group would accept intracortical implants. This resistance over implantation is evidence of the need for researchers to clearly identify, communicate, and further improve the significant benefits (i.e., additional performance, increased degrees of freedom, low health risk) of using microelectrode array (MEA) over other less intrusive BCIs, while actively working on minimizing the drawbacks (i.e., signal degradation and large calibration time).

1.2.3 Motor Cortical BCI System

Cognitive motor control, such as real and imaginary movements, is dependent on the activity of the motor cortex (Georgopoulos et al. 1986, Georgopoulos and Carpenter 2015). However, whether neural activity relates to direct muscle activation or to abstract movement features is still controversial. Much work has been done to comprehend how reaching and grasping are represented by motor cortical cells. Moran and Schwartz (1999) looked at single-cell activity patterns during reaching and found that many cells can have a "preferred direction", as well as some time-varying activity associated with movement speed. The motor cortex population vector can predict movement dynamics and has been used successfully to control neuroprosthetics (Collinger et al. 2013). In this study, an individual with tetraplegia was implanted with two 96-channel MEAs in the motor cortex to control an anthropomorphic prosthetic limb. They found

consistent improvement in prosthetic limb control over 13 weeks. They continued research on the same participant (Wodlinger et al. 2015), changing their scope to extract hand-shape commands. The participant was able to control 10 degrees of freedom (10D) simultaneously despite degradation of the neuronal signals (reduced number of recording units and peak-to-peak amplitudes).

The outcome of another pilot for a neuromotor prostheses, known as BrainGate (Hochberg et al. 2006), proved that primary motor cortex neural activity in an individual with tetraplegia can be used to control a neural cursor and to perform basic actions with a robotic arm. A follow up trial, BrainGate2 (Ajiboye et al. 2017), reported for the first time the use of intracortical BCI with functional electrical stimulation (FES). The participant received an intracortical MEA in the hand area but also 36 implanted percutaneous electrodes to electrically stimulate his hand and arm muscles. The participant was able to use his paralyzed arm to feed himself.

Lastly, another study presented a 24-year-old man who could control an exoskeleton from bi-lateral wireless epidural recorders (Electrocorticography (ECoG) with 64 electrodes each) over the upper limb sensorimotor areas of his brain (Benabid et al. 2019). The patient found the prosthetic mobility rewarding, even if the BCI could only decode a maximum of 8 degrees of freedom (8D) bimanual tasks. The study lasted 24 months and showed no signal degradation and no side effects.

1.2.4 Goal based BCI System

The use of brain activity to control prosthetics can be done by decoding the different forces and rotations from the motor cortex. This method could potentially be improved by recognizing the user's goal as a command, then letting the specialized prosthetics adjust the forces and rotations

intelligently so that it is responsible to manage and execute the movement, including the application of an appropriate grip, force, and motion. In such a system, the BCI would first decode the user's intention based on, for example, the attended object in working memory correlated with motor execution activity. It would then start the activation of the prosthetic controller which would initiate and monitor the movement. The brain activity of the user would provide feedback to the prosthetic controller, mainly detecting if it is moving in the desired direction, by evaluating if the intention is still applicable and if the goal is being fulfilled.

1.3 A Brief Brain Mapping History

The desire to locate and decipher cognitive activity in the brain has an extensive and fascinating history predating modern neuroscience. In the 2nd century, the Roman physician Galen identified nerves as conduits for information after dissecting animal brains. René Descartes, a 17th-century philosopher, referred to the pineal gland as "the principal seat of the soul" (Bitbol-Hespériès, 2015). Two centuries later, now debunked phrenology was developed by Franz Joseph Gall, attempting to map personality traits to specific regions of the skull (Gall and Spurzheim, 1810). This represents one of the earliest known attempts to associate behavior with brain structure and paved the way for a series of subsequent findings and technologies that have advanced our understanding of the brain.

Individual neurons constitute the basic unit of the nervous system including the brain. In 1906, Ramon y Cajal and Camillo Golgi were awarded the Nobel Prize for their contributions to the histology of nerve cells. For the past century, the prevailing belief has been that the neuron serves as the structural and functional unit of the nervous system, known in neuroscience as the Neuron Doctrine. In the past decade, we have not only made significant progress in our understanding of

brain functions at the cellular and molecular levels, but with the help of technologies such as fMRI and EEG, we are also able to correlate cognitive activities with brain activation patterns in humans. The improvement of recording techniques has led to a novel perspective: physiological units, impacting our behavior and cognition, are made of ensembles of neurons rather than individual cells (Yuste 2015). This knowledge has become instrumental in diagnosing and treating neurological disorders, facilitating rehabilitation, and supporting the advancement of promising technologies such as BCIs.

1.3.1 Clinical Diagnosis and Treatment

Combining the integration of expected behaviors with our evolving understanding of the brain structures and their functions, we are now more proficient in attaining accurate and prompt diagnoses and treatments for neurological disorders.

For instance, in Parkinson's disease, deep brain stimulations involve placing electrodes in specific deep brain structures to modulate activity (Benabid, 2003). This can significantly improve symptoms, including tremors, by targeting and regulating the areas involved in dopamine generation.

Another recent study demonstrated the safety of stimulating the central lateral nucleus of the thalamus in individuals with traumatic brain injury. Moreover, the study revealed enhancement in executive control, with an important improvement in processing speed of at least 10% observed in all four participants (Schiff et al. 2023).

In epilepsy, modern intracortical recordings and advanced neuroimaging techniques can be used to identify the focal point of seizures. In some cases, surgical procedures may be employed to

alleviate or potentially cure the disorder, building on the pioneering work in epilepsy surgery by researchers such as Jasper and Penfield in the mid-20th century (Penfield and Jasper, 1954). Prior to invasive brain surgery to treat drug-refractory epilepsy or even brain tumors, online spatial-temporal functional mapping of activity was used to map cognitive functions. A study from Wang et al. (2016) showed the clinical utility of such an approach in mapping the human language function under clinical situations when time is limited and electrocortical stimulation mapping is impractical.

In the context of neurorehabilitation, brain mapping techniques such as fMRI can provide valuable knowledge of brain structures and functions. This information is then used to assess disfunction, develop rehabilitation strategies, and address neurological disorders or injuries. For example, Rugg and colleagues (Clare et al. 2013) used targeted training fMRI to map brain activity and identify neural correlates associated with memory functions in individuals with mild cognitive or memory impairment. Subsequently, targeted memory training and neurofeedback interventions were used to enable participants to modulate neural patterns associated with memory processes.

Table 1. The neurophysiological recording techniques referred to in this thesis. EEG: Electroencephalography, ECoG: Electrocorticography, sEEG: stereo Electroencephalography, MEA: microelectrode array.

	Electrodes Placement	Spatial Resolution	Temporal Resolution	Application
EEG	Scalp	Low	High	Diagnose: Epilepsy, Sleep disorders, Neurological Conditions Cognitive neuroscience research
ECoG	Brain surface	Medium	High	Presurgical mapping for epilepsy and tumors Cognitive neuroscience research
sEEG	Deep in Brain	Medium /High	High	Presurgical mapping for epilepsy (localizing seizure foci) Research on deep brain structures
MEA	In Cortex	High	High	Research on neural network activity Developing BCIs

1.3.2 Brain Computer Interfaces

In the context of invasive BCIs, the precise placement of electrode arrays, each measuring a few millimeters in both width and height, may greatly impact the subsequent functionality of the system leveraging this brain activity. In an innovative intraoperative method for online functional mapping using high-density ECoG recordings, Crone and colleagues (McMullen et al. 2020) effectively localized finger representations within the human primary somatosensory cortex.

1.4 Neurophysiological Electrical Signals

1.4.1 Recording Electrodes

Various brain recording devices offering a spectrum of spatial and temporal resolution can be used to research neural activity. The choice and location of electrodes within or near the brain depends

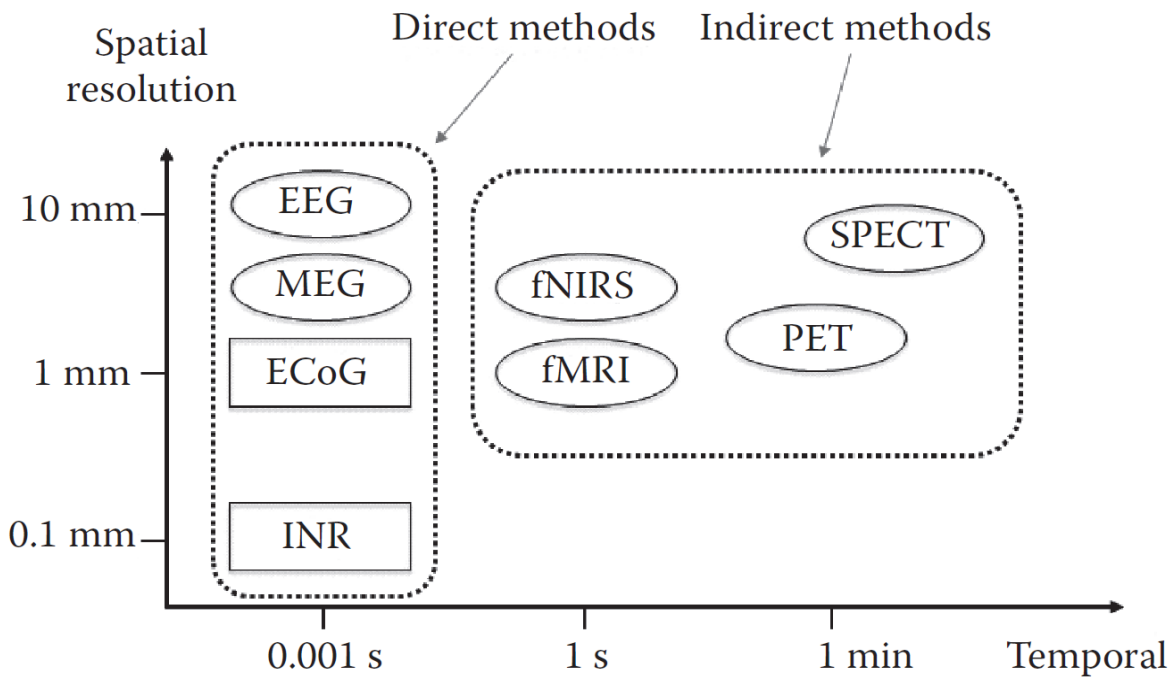

Figure 2. A comparison of the temporal and spatial resolution of direct and indirect methods for measuring brain activations (Nam et al. 2018).

on the research goals and the clinical needs. Table 1 outlines distinctive features of prevalent brain recording methods, including Electroencephalography (EEG), Electrocorticography (ECoG), stereo electroencephalography (sEEG), and Microelectrode array (MEA).

Recording signals that are localized, informative, and with a high signal to noise ratio often requires invasive techniques. A comparison of invasive and non-invasive signal recording (Figure 2) was reported by Nam et al. (2018). Intracortical neuronal recordings with their high spatial resolution provide more details and surpass all other recording techniques. This can be a significant advantage for MEA recordings if the goal is to decode precise motor or cognitive intent, where the signal is encoded in the activity of neurons localized in a small area of the brain.

In this thesis, Chapters 2-3 delve into the analysis of data acquired from microelectrodes in non-human primates. Chapter 4 employs EEG and sEEG neural signals to create and assess tools designed to characterize and pinpoint cognitive activity linked to intention. Finally, Chapter 5 assesses the validity of the toolset utilizing ECoG signals.

1.4.2 Brain Signals

1.4.2.1 Single-unit and multi-unit neuronal activity

The high spatial resolution of intracortical recordings enables the measurement of the extracellular action potentials, commonly known as ‘spikes’, from individual neurons or ‘single-units’ near the microelectrode tip (Gold et al. 2006). By sorting the recorded signal over time, it is possible to determine both the timing and the unit from which the spike originated. The frequency and timing of the spiking activity from individual single-units serve as distinctive features used in the classification of neural activity.

Spike sorting can be a time-consuming process, often impractical in real-time settings such as BCI systems. A simpler approach involves using the multi-unit activity which doesn't try to isolate an individual neuron's activity. Instead, it applies a voltage threshold on the high-frequency portion (>1000 Hz) of the extracellular intracortical recordings, identifying probable action potentials from the local network of neurons (Burns et al. 2010). The time and frequency of all detected spikes on the electrode can then be used as features for characterizing neural activity.

1.4.2.2 Local Field Potentials (LFPs)

In 1924, German psychiatrist Hans Berger invented the EEG and recorded brain electrical activity for the first time. Brain oscillations are believed to play a role in regulating excitability in neuronal assemblies, assisting in the selection and integration of features from stimuli that are relevant to the organism. This synchronization of activity enables the brain to coordinate information processing and communication among brain regions, thereby facilitating attention, perception, memory formation, and other cognitive activities.

LFPs are low-frequency signals (< 500 Hz) reflecting the collective activity of the surrounding population of neurons. These extracellular voltage fluctuations offer insights into essential integrative synaptic processes which can't be measured from the activity of a few neurons alone (Einevoll et al. 2013). These signals are recorded through electrodes in or near the brain, found in devices like MEA, EEG, sEEG, or ECoG.

Oscillatory signals from LFPs are typically characterized by their frequency, amplitude, and phase. Using time-frequency analysis such as Fast Fourier Transform (FFT) on the LFPs, the amplitude of oscillations within a frequency band can provide information on the synchronization within local brain networks. In the analysis of brain activity, the commonly extracted frequency bands

from LFPs include theta, beta, alpha, and gamma, with frequency ranges of 4-8Hz, 8-12Hz, 12-30Hz, and 30-100Hz respectively. These extracted features, synchronized with task events, can provide insights on brain areas involved in cognitive activity (Chapters 4 and 5) or can be used to decode factors related to user's intention (Chapters 2 and 3). For example, Ramsey et al. (2006) showed that gamma power increased during mental calculation and remained high until the task was terminated, proving that the lateral prefrontal cortex (LPFC) is active for the duration of mental processing. Note that the intricate interactions between neurotransmitter, neuronal activity, and the brain rhythms are complex and remain under investigation.

Theta The low frequency theta oscillations have been observed not only in primates' hippocampus, but also in cortical and other subcortical structures. These slow waves are thought to bind areas of the brain together during memory formation and retrieval. In human studies, they are associated with various cognitive activities including the formation of episodic memories (Lega et al. 2012) and virtual navigation (Ekstrom et al. 2005). Theta modulation over the prefrontal cortex during memory encoding, along with the impact of working memory load, remains uncertain due to inconsistent conclusions found in different studies (Herweg et al. 2020). These investigations have reported both increases and/or decreases in theta oscillations during successful trials. Such variability complicates the understanding of the precise role of this rhythm in cognitive activity.

Alpha As described by Buzsáki (2006), Hans Berger first discovered brain oscillations which were induced by awake but calm subjects closing their eyes. He called the large-amplitude rhythm the alpha waves (approximately 10 waves per second). While engaged in cognitive functions, certain regions of our brains are active while others are inactive. Functional inhibition of inactive regions is thought to be achieved by alpha oscillations (8-13Hz; Jensen and Mazaheri 2010). Haegens et

al. (2011) demonstrated that an increase in alpha oscillations is linked to a decrease in spiking activity observed in sensorimotor regions. The desynchronization of specific brain regions could influence processing by releasing inhibitions in assemblies coding the attended location.

Beta The exact functional role of beta is not fully understood. Research has found that this rhythm is strong during rest or after a movement yet tends to desynchronize during active movement (Baker et al. 2003, Davis et al. 2012). These oscillations found in the frontal cortex are associated with top-down control of behavior (Buschman and Miller 2007) and change over time during a task (Stoll et al. 2016). Additionally, Stoll et al. (2016) reported an elevation in beta power derived from intracranial LFPs in monkeys when cognitive control was required.

Gamma Buzsáki (2006) reported that if a brain network is under inhibition mediated by fast-acting $GABA_A$ receptors, a gamma rhythm (40-100 Hz) will emerge. Since interneurons with such receptors are commonly found throughout the brain, these oscillations can emerge from almost any brain structure. Gamma oscillations are transient and typically arise from the coordinated interaction between excitation and inhibition (Buzsáki and Wang, 2012). Oscillations in this frequency band are found in many cortical areas, arising in response to different stimuli or tasks and being associated with various cognitive functions (Fries, 2009).

Fonken et al. (2016) and Buzsáki et al. (2012) described some of the characteristics of the ECoG signals during cognitive tasks. According to these studies, the gamma rhythm tends to increase during sensory input and motor preparation. It is typically influenced by sensory info held in working memory with its power being correlated with the number of objects in working memory (Roux et al. 2012). In the prefrontal cortex of monkeys engaged in a working memory task, the power in this band is anti-correlated with the power in lower bands (8-30 Hz; Bhattacharya et al.

2022). In Chapters 4 and 5, I will use features from EEG and ECoG signals to characterize and localize brain areas involved in working memory executive functions.

1.4.2.3 Principal Spectral Components

Manning et al. (2009) suggested that broad changes in the power spectra of the LFP could be a good predictor of local neuronal spiking. The analysis of the LFP spectra through principal component analysis, specifically the projection on the first vector (PSC1), serves as a broadband feature that revealed distinct motor cortex representation for individual finger movements in humans (Miller et al. 2009). The evaluation of this feature is detailed in the subsequent chapter (section 2.3.4) and applied across chapters 2 through 5 of this thesis.

1.5 Cognitive Functions

Our cognitive system has the capacity to guide our thoughts and actions toward pre-determined objectives. This is achieved by executing control measures such as shifting attention, responding to conflicts, balancing speed versus accuracy, controlling errors, and inhibiting responses when necessary (Logan et al. 2014). In the context of working memory, these measures are used to maintain a constant working memory representation, blocking interferences while keeping the working memory current when goals undergo changes (Boag et al. 2021).

In Chapter 4, I will detail the tools and methodology designed to identify the optimal location for a goal-based iBCI implant. To achieve this objective, a set of tasks was programmed to trigger working memory, movement intention, and visual spatial attention. The brain activity of the subjects, while engaged in these tasks, can then be analyzed to identify the brain area most involved with the cognitive functions.

Table 2. Oscillatory activity related to different phases of working memory (Roux et al. 2014).

	Encoding	Maintenance	Retrieval
Theta		• Involved in the temporal organization of WM items. • Decrease in dorsolateral prefrontal cortex (dlPFC) with WM load.	
Alpha	• Increased excitability needed for goal-oriented stimulus processing is reflected in decreased alpha power. • Stronger power coupled with the forgotten trials (parietal regions).	• Activity is not relevant for WM information but protects WM items from non-relevant information.	
Gamma	• Reflect a feedforward drive in the visual hierarchy.	• Amplitude of oscillations associated with number of items to be memorized (parietal and PFC).	• Highly positively correlated with retrieval success.
Other	• Formation of visual memories controlled by gamma power phase-locked to alpha oscillations.	• Synchronization at theta, alpha and gamma frequencies related to top-down control manipulation of WM items.	

1.5.1 Working Memory

Working memory is the temporary maintenance and manipulation of a limited amount of information and thus a key function supporting goal-directed behavior. Since it involves both retaining and processing the information, it is often broken down into three phases: (1) encoding, which is used to memorize a set of items, (2) maintenance, which temporarily holds the information, and (3) retrieval of the memorized items. As early as 1998, Tallon-Baudry and colleagues reported an increase of EEG gamma oscillations during a visual delayed-match-to-sample task. Kim's research (Kim, 2019) shows the main areas of the brain involved in the different phases of working memory. The author identified a dorsal attention network and a

frontoparietal control network which are involved differently during the phases of working memory. Interestingly, this study showed that the prefrontal cortex is part of the frontoparietal control network and is mostly involved with the retrieval activity of working memory. Based on current literature, Table 2 identifies the neural activity criteria associated with the different phases of working memory.

1.5.2 Spatial Working Memory (SWM)

Much like the general working memory, SWM is the cognitive process responsible for temporarily storing and manipulating spatial information. In terms of neurophysiology, it is recognized that the action potential firing pattern of place cells found in the hippocampus of rodents (O'Keefe and Dostrovsky 1971, Buzsáki and Moser 2013, Spellman et al. 2015) are known to encode spatial information in working memory. Similarly, for primates the activity of hippocampus cells has been associated with gaze-position (Rolls and Xiang 2006, Ekstrom et al. 2003), its firing pattern being modulated by the view, environment, and other cognitive factors (Rolls and Wirth 2018, Gulli et al. 2020).

In goal-directed behaviors, actions are chosen based on features extracted from the SWM. The topology and physical process of storing, maintaining, and updating the environment is still elusive even after years of extensive research (Klauer and Zhao, 2004). Studies have shown the impact of prefrontal cortex lesions in the successful execution of SWM functions (Curtis and D'Esposito, 2003) and that the firing rate of the PFC cells is modulated depending on SWM task demands (Jung et al. 1998, Corrigan et al. 2021). In addition, it was reported that cortical circuits between the hippocampus and prefrontal cortex in rodents are linked to working memory performance (Jones and Wilson 2005, Wang et al. 2006), where task relevant information is associated with the

synchronization of gamma oscillations (Spellman et al. 2015). During SWM function, the role of the hippocampus is to support the retrieval of learnt spatial information to simulate the future, while the PFC is particularly involved in the evaluation and the choice of future path (Javadi et al. 2017, Spiers et al. 2015). Chapter 3 of this thesis further explores the representation of spatial location within a maze in macaque PFC.

1.5.3 Planning of Movement

Before executing a movement, primates must assess their body's spatial position and the surrounding environment. They then ascertain the feasibility and appropriateness of possible actions to achieve their intended goal before initiating the movement. A focus definition of movement planning is a process that links the overarching goals of a movement to a control policy for executing the movement (Haith and Bestmann, 2020 (p.542 Cogn Neur)). As described by Henley (2021), the posterior parietal cortex integrates sensory information from visual, tactile, and proprioceptive pathways. This brain region will relay the integrated information to the prefrontal and premotor areas, where it undergoes further processing to formulate a movement plan. Ultimately, the motor cortex executes the planned movement.

In the context of a visuomotor task, Aoki et al. (1999) observed synchronization of gamma-range activity in the sensorimotor cortex of humans. They then proposed the possibility that gamma oscillations had a role to play in sensorimotor integration or attention. In another study, Cisek and Kalaska (2005) demonstrated that possible actions are initially represented in the dorsal premotor cortex. As evidence accumulates in favor of a specific action, the spiking signal corresponding to the chosen movement increases, while spiking signals associated with other options decrease.

Chapter 2 of this thesis demonstrates the capability to decode saccade intentions from the macaque PFC using features derived from LFPs.

1.5.4 Visual Attention

In the field of neuroscience, top-down processing refers to the influence of high-level cognitive factors, such as context, expectations, and prior knowledge, on the interpretation of sensory information and perception. Bottom-up refers to the sensory information from the environment progressing through the processing hierarchy, allowing the formation of a perception based on the sensory input. Buschman and Miller (2007) demonstrated that neurons from prefrontal areas were the initial ones to encode the target location during top-down processing of attention, whereas parietal neurons demonstrated this early representation during bottom-up attention processing.

Visual Spatial Attention The cognitive process of visual spatial attention entails focusing attention on a specific location in space, enabling primates to selectively attend to and process information from a particular area in the visual field. Primate experiments on covert spatial attention typically require the animal or participant to keep their gaze on a fixation point while monitoring the appearance of a cue at a spatial location. As anticipated and proven by Posner (1980), an observer is faster and more accurate at detecting a sensory input that emerges in the attended location. Fries et al. (2001) reported that visual cortex neurons were responsive to attended visual stimuli, as opposed to distractor stimuli, and exhibited increased synchronization in gamma-frequency (35-90 Hz) oscillations while reducing the synchronization at lower frequency (<17 Hz).

In Chapter 4, EEG brain signals are explored through a task specifically designed to evoke this cognitive function.

1.6 Decoding Intentions

The ability to decipher the end goal is essential for a system aiming to control a prosthetic device from the user's intention. Most iBCIs decode the intended movement from the spike signals of the motor cortex and translate the forces and rotations into commands to control assistive devices. Unraveling the overarching goal of a BCI user is not a trivial problem. Many factors can be used to recognize a target action including motor planning, decision-making, abstract rule selection, objects in working memory, and visual spatial attention.

1.6.1 Decoding Intentions from the Prefrontal Cortex

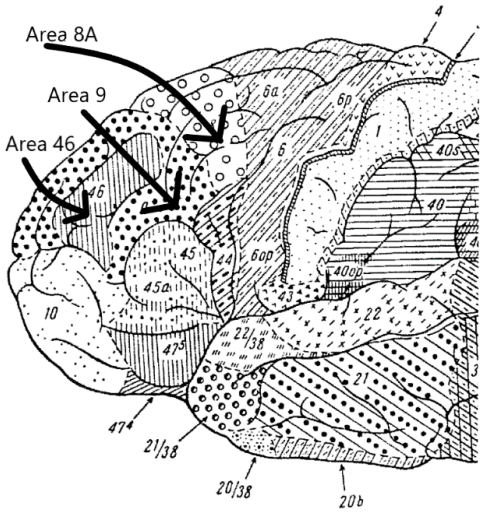

Figure 3. Cytoarchitectonic map of human frontal cortex from Petrides and Pandya (1999).

The prefrontal cortex has reciprocal connections to most of the cortical and subcortical structures, making it well suited to monitor and decode the intentions. In the "top-down system", context and goal-driven brain modulation is a result of the working memory used to coordinate executive function, attention, data maintenance, and manipulation within the prefrontal cortex. The dlPFC in humans (Broadman areas 46, 9 and 8A; Figure 3) is particularly implicated in these goal encoding functions (Jackson et al. 2021).

Behavioral decisions are based on our ability to abstract rules from our life experiences. "Intelligent behavior requires acquiring and following rules. Rules define how our behavior should adjust to different situations" (Buschman et al. 2012). Recent clinical research in humans found

that individuals with lesions in the dlPFC showed an inability to shift from one sorting rule to another (Milner, 1963). Moreover, visual spatial attention and working memory, both very important signals for decoding one's current goals, have been associated with the dlPFC (Fuster and Alexander 1971, Everling et al. 2002). Miller and colleagues (1996) measured the average firing rates of sample-selective neurons in the macaque prefrontal cortex during a visual working memory task. They discovered that these neurons are crucial for distinguishing and retaining stimuli in memory, as well as for evaluating how those stimuli match up to a given sample. Furthermore, the spontaneous activity of neuronal ensemble in the lateral prefrontal cortex of non-human primates could reliably predict the allocation of attention (Tremblay et al. 2015).

Within the dlPFC, Brodmann Area 8A (depicted in Figure 3) has connections with the parieto-occipital region, the auditory-related areas in the superior temporal gyrus, and the supra-temporal plane (Petrides and Pandya, 1999). Additionally, connections originate from the caudal superior temporal sulcal cortex. Multiple behavioral studies on macaques detailed the characteristics of LFPs and spikes of the neurons in this brain region but to our knowledge, no intracortical recording has been performed in humans during such cognitive tasks. The strong homology between area 8A of humans and macaques has allowed researchers to find strong neuronal correlates of rules encoding, working memory, and spatial attention in macaques, thus replicating human findings from less intrusive methods. For example, recording of neuronal activity from monkeys trained to use two abstract rules showed prevalent activity in the PFC (including dorsolateral) related to the coding of those rules (Wallis et al. 2001). Buschman et al. (2012) further found evidence, in macaque dlPFC, that oscillatory synchronization of LFPs formed neural ensembles representing rules.

Using event-related fMRI, Rowe et al. (2000) demonstrated that maintenance of spatial items in memory involved Brodmann area 8 and the parietal lobe, while selection of an item in memory was linked to Brodmann area 46. Recording of neurons' activity in the dorsolateral prefrontal cortex of macaques showed specific characteristics of spiking (brief bursts of gamma oscillations) related to sensory inputs held in working memory (Miller et al. 2018).

Neural signals correlating with spatial visual attention are also detectable within the dlPFC (Lennert and Martinez-Trujillo 2013, Tremblay et al. 2015). Note that Lennert and Martinez-Trujillo (2013) indicated that "Neurons in the primate dlPFC of one hemisphere are selective for the location of attended targets in both visual hemifields.". Decoding the saccade or just the intention of movement can provide key information on behavioral goal identification, especially providing insights on the location of spatial attention. Boulay et al. (2016) demonstrated that it was possible to decode intended saccade target location from the lateral prefrontal cortex (area 8A) of macaques, suggesting that it would be a suitable source of information for a goal-selection cognitive BCI. A similar approach was investigated by Jia et al. (2017) using intracortical oculomotor BCIs on monkeys to detect intended saccade. The high frequency LFPs from frontal and supplementary eye fields (with a small contribution of the dlPFC) provided real time, intended saccade location with high accuracy.

In the last decades, the prefrontal cortex has been an interesting source of information for the BCI systems. Ramsey et al. (2006) investigated the potential to use higher cognitive systems for BCI based on activity in the prefrontal cortex recorded with fMRI and ECoG signals. They showed that gamma power increased during mental calculation and remained high until the task was terminated, proving that the dlPFC is active for the duration of mental processing. Further to that

study, Vansteensel et al. (2010) demonstrated that the cognitive control network from ECoG signals over the dlPFC are a suitable source of information for BCI applications. They could distinguish between language versus mental calculation which was used to control a cursor. These results did not address how to decode goals but demonstrated some signal characteristics such as sustained and discrete activities from the dlPFC during cognitive tasks.

1.6.2 Decoding Intentions from Parietal Cortex

The use of brain areas other than motor cortex to control external devices was also investigated by Aflalo et al. (2015). They implanted a multi-electrode array in the posterior parietal cortex and demonstrated successful decoding of motor planning including the imagined goals, trajectories, and types of movement.

1.7 Statistical Analysis and Dimensionality Reduction

In this thesis, statistical analysis is performed to assess the significance of variations in LFP-based features between subsets of trials or different task epochs. Dimensionality reduction techniques are used to create new features that capture important components of brain activity, thereby enhancing machine learning decoding accuracy or decreasing processing demands in BCI applications.

1.7.1 One-way analysis of variance (ANOVA)

ANOVA is a statistical test used to assess if there are significant differences between means from multiple groups. It assumes that each observation within a group is normally distributed. In the context of one feature provided for each observation belonging to one of k classes, the model can be expressed as:

$$y_{ij} = \alpha_j + \varepsilon_{ij} ,$$

where y_{ij} is an observation, with *i* denoting the observation number and *j* indicating the class.

α_j is the population mean for the class *j*.

ε_{ij} is the random error, which is independent, normally distributed, and characterized by a zero mean and constant variance.

In the context of one feature provided for a minimum of two classes, the analysis of variance is used to test the hypothesis that all classes' means are equal (H_0: $\alpha_1 = \alpha_2 = \ldots = \alpha_k$) against the alternate possibility that at least one of the classes mean is different (H_1: $\alpha_i \neq \alpha_j$ for at least one *i* and *j*). The Matlab function "anova1" returns a *p*-value that serves as an indicator of the significance of differences between classes.

1.7.2 Support Vector Machine (SVM) Learning

Invented by Vapnik and Chervonenkis in the early 1960s and further developed at AT&T Bell Laboratories (Cortes and Vapnik, 1995), SVMs are supervised learning algorithms used for both data classification and regression analysis. For classification, it uses the training examples from two classes to discover a decision boundary (hyperplane) that maximizes the margin, which is the gap between the classes. The goal of identifying such a boundary is to improve generalization to unseen data, ensuring a robust classification. This algorithm can perform linear classification or nonlinear classification using a kernel trick, which involves mapping the training examples into a higher-dimensional feature space.

In the context of this thesis, the linear SVM algorithm was exclusively used to classify the sets features. In general, a training set is defined as a set of *n* points in the form $(x_1,y_1),\ldots,(x_n,y_n)$ where x_i represents a 2-D real vector for the observation *i*, and $y_i \in \{-1,1\}$ is the class to which this

observation belongs. The goal is to find the hyperplane that maximizes the margin, which is the distance to the closest point of each class. The hyperplane must adhere to the equation:

$$\mathrm{w}^T x_i + b = 0 \,,$$

where *x* is the input observation vector, *i* is the observation number, *w* is the normal vector to the hyperplane, and *b* is the offset or bias. This reduces to the optimization problem formulated as:

$$arg_{\mathrm{w},b} \min \frac{1}{2} \|\mathrm{w}\|^2 \quad \text{subject to} \quad y_i(\mathrm{w}^T x_i + b) \geq 1 \text{ for } i \in \{1, \ldots, n\}.$$

The objective is to determine the values of w and *b* that define the hyperplane with the maximum margin between the classes.

The basic algorithm is a binary classifier, but many implementations and libraries extend the use of SVMs for multi-class classification by using one-vs-one or one-vs-all (one-vs-rest) methods. In the one-vs-one approach, each binary classifier (for 4 classes: 6 binary classifiers, in general (n-1)! classifiers) votes for one of two classes and the class with most votes is the final prediction. For one-vs-all, a binary classifier is trained for each class against all the other classes (for 4 classes: 4 classifiers). The class with highest confidence is the final prediction. In this thesis, the SVM implementation used for multi-class classification utilizes the one-vs-all method.

Opting for SVMs over alternative machine learning algorithms offers advantages, such as its efficacy in scenarios with limited sample sizes as well as its ability to handle imbalanced datasets.

1.7.3 Dimensionality Reduction

In classification and decoding scenarios, dimensionality reduction is often used as a strategy to reduce data complexity, improve computational efficacy, identify pertinent features, visualize

important dimensions, simplify the problem, while retaining essential information from the original dataset.

Principal Component Analysis (PCA) This statistical procedure transforms a set of possibly correlated variables into a set of linearly uncorrelated variables called principal components. These components are arranged based on the variance they capture, with the principal component holding the maximum variance indicating the direction in which the data varies the most. For a comprehensive guide on the detailed procedures for assessing and applying PCA, consult the paper authored by Shlens (2014).

Canonical Discriminant Analysis (CDA) Linear Discriminant Analysis (LDA) is a statistical method used for classification, often introduced in the context of two-group discrimination. This supervised method finds a linear combination of features that characterizes or discriminates between two or more classes in the dataset. CDA serves as a more generalized extension, specially designed for analysis of more than two groups. As a multivariate statistical analysis method, it is designed to investigate differences between two or more predefined groups within a dataset. Its primary objective is to extract canonical variables, which represent linear combinations of variables that can best discriminate between these groups (Ramsay and Silverman, 1997).

1.8 Research Problem and Objectives

1.8.1 BCI Limitations

Current BCI technology is promising but based on survey results, does not meet users' needs (Huggins et al. 2015). It requires too much time for a care provider or technician to set up, calibrate,

and dismantle the system. Additionally, the functions provided are limited, exhibiting low and, at times, unacceptable performance.

With surface and cortical recordings, some artifacts may be mistaken for brain activity, such as artifacts from pulsatile vessels, electrocardiogram, electrical power (60 Hz) and unstable or loose electrode contacts. Some of these limitations and artifacts are not as problematic using intracortical recording but still need to be considered when processing the signals.

In intracortical recordings, single-unit stability is unreliable. Dickey et al. (2009) reported that 57% of the original units were stable after 7 days, going down to 39% after 15 days. Relying on single-unit activity means either detecting the unit stability over sessions or calibrating the BCI decoder each session with the currently active units. Using the intracortical LFPs, Milekovic et al. (2018) reported the ability of two BCI users to control a communication system gradually yet consistently (achieving 3.07 to 6.88 correct characters per minute). Remarkably, this was accomplished without the need for recalibration for up to 138 days and without a significant decline in performance. As for longevity of intrusive BCI, the same study reported that for the first time, a stable intracortical BCI based on LFPs was used by people with tetraplegia over a period of up to four and a half months.

Current knowledge of neuronal activity in the dlPFC is mostly based on animal research. Results on animals provide great insight, however it requires extensive time to train the animals on designed tasks which are limited to the animal's mental capacity. Moreover, the prefrontal cortex in humans is significantly larger and more complex than in macaques.

The latest BCI decoders have been able to identify a limited amount of movement intentions with up to ten degrees of freedom (Wodlinger et al. 2015). One of the significant obstacles to current research advancement in this area is the difficulty to capture and decode, in real time, neuronal activity in multiple areas of the human brain. Freely moving one arm would require the real time processing of motor cortex neurons from the shoulder, arm, hand, and fingers but also possibly to other brain areas like the cerebellum, brainstem, and subcortical structures. Capturing this level of activity within the brain is not possible for many reasons, such as under-sampling, safety, and technical feasibility. This problem is mitigated by algorithms that impose smoothness on the BCI output but may also benefit from signals reflecting the intended target.

1.8.2 Neuro-Cognitive Communicator (NCC) clinical trial

The Neuro-Cognitive Communicator is an Ottawa Hospital Research Institute (OHRI) sponsored exploratory study of an assistive neuro prosthetic device for patients with severe upper motor disabilities. In this study, two participants will be implanted with two microelectrode arrays (MEAs) located in the motor cortex and in area 8A within the dlPFC. A critical outcome of the operative phase of the trial is to accurately map the precise location of the cortex areas we intend to use for intracortical signal recordings. Determining the optimal placement of the NeuroPort MEA will rely on identifying locations modulated by cognitive activity through the analysis of recorded signals from microECoG grids. The recording sessions will take place while the participant is engaged in tailored cognitive tasks during the intraoperative phase of the trial.

The research conducted in this thesis was intricately connected to the preparation of this clinical trial which will focus on decoding goals and cognitive intentions from neural signals in the dlPFC and motor cortex of the trial participants. The intraoperative phase of the trial will take place within

the hospital, where participants may be medicated or recovering from surgery. Considering the stress levels, emotions, and the overall condition of the trial participant, the designed tasks are required to be brief, straightforward, and involve minimal physical movements and cognitive demands. The research associated with the preparatory phase encompasses the development of cognitive tasks and signal processing tools to identify the optimal placement for both microelectrode array implants. As described in Chapter 4, the development and evaluation of the processing chain will include the recording of EEG brain activity captured from volunteers engaged in the customized cognitive tasks. The validation of the mapping process will be elaborated in Chapter 5 using a relevant open source electrocorticography (ECoG) dataset.

1.8.3 Research Objectives

The first goal is to decode cognitive factors and show their usability in a goal based BCI system. I hypothesize that intracortical LFPs from the prefrontal cortex can provide useful features for a goal based BCI system. The second goal is to define a methodology to localize areas of the brain involved with goal encoding factors (i.e., cue processing, working memory, movement intentions). For this objective, I hypothesize that during cognitive tasks, extracted features from human ECoG signals can be used to locate the areas of the brain involved with the cognitive activity.

1.9 Conclusion

The brain is a remarkably complex organ that consistently adapts to ongoing stimuli and its environment. Despite this dynamic nature, the identification and the decoding of cognitive activity remain feasible through the analysis of brain signals with varying spatial and temporal resolutions.

The derived variables are expected to offer insights into the BCI user's intentions, enabling control over assistive technology.

In this chapter, essential background information is presented to facilitate the understanding of the research objectives, challenges, and methodologies employed in this thesis. The introduction starts by covering BCI systems, brain mapping, and their usability, followed by the exploration of potential brain signals recorded in proximity to, on, or within cortical matter. For BCIs, which attempt to decode the overarching goals of the user, an overview of important cognitive functions and decoding techniques, including machine learning and statistical analysis, is presented. Finally, the research objectives of this thesis with their hypothesis are iterated, aiming to address some of the existing limitations in BCI technology.

1.10 References

[1] Aflalo T, Kellis S, Klaes C, Lee B, Shi Y, Pejsa K, et al. Decoding motor imagery from the posterior parietal cortex of a tetraplegic human. Science Magazine [Internet]. 2015;348(6237):906–10.

[2] Ajiboye AB, Willett FR, Young DR, Memberg WD, Murphy BA, Miller JP, et al. Restoration of reaching and grasping movements through brain-controlled muscle stimulation in a person with tetraplegia: a proof-of-concept demonstration. The Lancet [Internet]. 2017;389(10081):1821–30.

[3] Aoki F, Fetz EE, Shupe L, Lettich E, Ojemann GA. Increased gamma-range activity in human sensorimotor cortex during performance of visuomotor tasks. Clinical Neurophysiology. 1999;110(3):524–37.

[4] Baker SN, Pinches EM, Lemon RN. Synchronization in monkey motor cortex during a precision grip task. II. Effect of oscillatory activity on corticospinal output. Journal of Neurophysiology. 2003;89(4):1941–53.

[5] Benabid AL. Deep brain stimulation for Parkinson's disease. Vol. 13, Current Opinion in Neurobiology. 2003. p. 696–706.

[6] Benabid AL, Costecalde T, Eliseyev A, Charvet G, Verney A, Karakas S, et al. An exoskeleton controlled by an epidural wireless brain-machine interface in a tetraplegic patient: a proof-of-concept demonstration. The Lancet Neurology [Internet]. 2019 Oct;0(0).

[7] Bhattacharya S, Brincat SL, Lundqvist M, Miller EK. Traveling waves in the prefrontal cortex during working memory. PLoS Computational Biology [Internet]. 2022;18(1):1–22.

[8] Bitbol-Hespériès A. Pineal Gland. In: Nolan L, ed. *The Cambridge Descartes Lexicon*. Cambridge University Press; 2015:593-596.

[9] Boag RJ, Stevenson N, Van Dooren R, Trutti AC, Sjoerds Z, Forstmann BU. Cognitive control of working memory: A model-based approach. Brain Sciences. 2021;11(6):21–5.

[10] Boulay CB, Pieper F, Leavitt M, Martinez-Trujillo J, Sachs AJ. Single-trial decoding of intended eye movement goals from lateral prefrontal cortex neural ensembles. Journal of Neurophysiology. 2016;115(1):486–99.

[11] Burns SP, Xing D, Shapley RM. Comparisons of the dynamics of local field potential and multiunit activity signals in macaque visual cortex. Journal of Neuroscience. 2010;30(41):13739–49.

[12] Buschman TJ, Denovellis EL, Diogo C, Bullock D, Miller EK. Synchronous Oscillatory Neural Ensembles for Rules in the Prefrontal Cortex. Neuron [Internet]. 2012;76(4):838–46.

[13] Buschman TJ, Miller EK. Top-down versus bottom-up control of attention in the prefrontal and posterior parietal cortices. Science. 2007;315(5820):1860–4.

[14] Buzsáki G. Rhythms of the Brain. Oxford University Press. 2006.

[15] Buzsáki G, Anastassiou CA, Koch C. The origin of extracellular fields and currents--EEG, ECoG, LFP and spikes. Nature reviews Neuroscience [Internet]. 2012;13(6):407–20.

[16] Buzsáki G, Moser EI. Memory, navigation and theta rhythm in the hippocampal-entorhinal system. Nature Neuroscience. 2013;16(2):130–8.

[17] Buzśaki G, Wang XJ. Mechanisms of gamma oscillations. Annual Review of Neuroscience. 2012;35:203–25.

[18] Cisek P, Kalaska JF. Neural correlates of reaching decisions in dorsal premotor cortex: Specification of multiple direction choices and final selection of action. Neuron. 2005;45(5):801–14.

[19] Clare L, Linden DEJ, Woods RT, Whitaker R, Evans SJ, Parkinson CH, et al. Goal-oriented cognitive rehabilitation for people with early-stage alzheimer disease: A single-blind randomized controlled trial of clinical efficacy. American Journal of Geriatric Psychiatry [Internet]. 2010;18(10):928–39.

[20] Collinger JL, Wodlinger B, Downey JE, Wang W, Tyler-Kabara EC, Weber DJ, et al. High-performance neuroprosthetic control by an individual with tetraplegia. The Lancet [Internet]. 2013;381(9866):557–64.

[21] Corrigan BW, Gulli RA, Doucet G, Roussy M, Luna R, Sachs AJ, et al. Different neural codes serve long and short-term memory functions in primate Hippocampus and Lateral Prefrontal Cortex during virtual navigation. bioRxiv [Internet]. 2021;2021.08.20.457136.

[22] Cortes, C., & Vapnik, V. Support-vector networks. Machine Learning. 1995;20(3):273-297.

[23] Curtis CE, D'Esposito M. Persistent activity in the prefrontal cortex during working memory. Trends in Cognitive Sciences. 2003;7(9):415–23.

[24] Davis NJ, Tomlinson SP, Morgan HM. The role of beta-frequency neural oscillations in motor control. Journal of Neuroscience. 2012;32(2):403–4.

[25] Dickey AS, Suminski A, Amit Y, Hatsopoulos NG. Single-unit stability using chronically implanted multielectrode arrays. Journal of Neurophysiology. 2009;102(2):1331–9.

[26] Einevoll GT, Kayser C, Logothetis NK, Panzeri S. Modelling and analysis of local field potentials for studying the function of cortical circuits. Nature Reviews Neuroscience. 2013;14(11):770–85.

[27] Ekstrom AD, Caplan JB, Ho E, Shattuck K, Fried I, Kahana MJ. Human hippocampal theta activity during virtual navigation. Hippocampus. 2005;15(7):881–9.

[28] Ekstrom AD, Kahana MJ, Caplan JB, Fields TA, Isham EA, Newman EL, et al. Cellular networks underlying human spatial navigation. Nature. 2003;425(6954):184–7.

[29] Everling S, Tinsley CJ, Gaffan D, Duncan J. Filtering of neural signals by focused attention in the monkey prefrontal cortex. Nature Neuroscience. 2002;5(7):671–6.

[30] Fonken YM, Rieger JW, Tzvi E, Crone NE, Chang E, Parvizi J, et al. Frontal and motor cortex contributions to response inhibition: evidence from electrocorticography. Journal of Neurophysiology [Internet]. 2016;115(4):2224–36.

[31] Fries P, Reynolds JH, Rorie AE, Desimone R. Modulation of oscillatory neuronal synchronization by selective visual attention. Science. 2001;291(5508):1560–3.

[32] Fries P. Neuronal gamma-band synchronization as a fundamental process in cortical computation. Annual Review of Neuroscience. 2009;32(April 2009):209–24.

[33] Fuster J, Alexander G. Neuron Activity Related to Short-Term Memory. Science, New Series. 1971;173(3997):652–4.

[34] Gall FJ, & Spurzheim, JG. Anatomie et physiologie du système nerveux en général, et du cerveau en particulier: Avec des observations sur la possibilité de reconnoître plusieurs dispositions intellectuelles et morales de l'homme et des animaux, par la configuration de leurs têtes. F. Schoell, 1810.

[35] Georgopoulos AP, Carpenter AF. Coding of movements in the motor cortex. Current Opinion in Neurobiology [Internet]. 2015;33:34–9.

[36] Georgopoulos AP, Schwartz AB, Kettner RE. Neuronal population coding of movement direction. Science. 1986 Sep 26;233(4771):1416-9.

[37] Gold C, Henze DA, Koch C, Buzsáki G. On the origin of the extracellular action potential waveform: A modeling study. Journal of Neurophysiology. 2006;95(5):3113–28.

[38] Gulli RA, Duong LR, Corrigan BW, Doucet G, Williams S, Fusi S, et al. Context-dependent representations of objects and space in the primate hippocampus during virtual navigation. Nature Neuroscience. 2020 Jan 1;23(1):103–12.

[39] Haegens S, Nácher V, Luna R, Romo R, Jensen O. α-Oscillations in the monkey sensorimotor network influence discrimination performance by rhythmical inhibition of neuronal spiking. Proceedings of the National Academy of Sciences of the United States of America. 2011;108(48):19377–82.

[40] Henley C. Foundations of Neuroscience [Internet]. Michigan State University Libraries; 2021. Available from: https://openbooks.lib.msu.edu/neuroscience/

[41] Herweg NA, Solomon EA, Kahana MJ. Theta Oscillations in Human Memory. Vol. 24, Trends in Cognitive Sciences. 2020. p. 208–27.

[42] Hochberg LR, Serruya MD, Friehs GM, Mukand JA, Saleh M, Caplan AH, et al. Neuronal ensemble control of prosthetic devices by a human with tetraplegia. Nature. 2006;442(7099):164–71.

[43] Huggins JE, Moinuddin AA, Chiodo AE, Wren PA. What would brain-computer interface users want: Opinions and priorities of potential users with spinal cord injury. Archives of Physical Medicine and Rehabilitation [Internet]. 2015;96(3):S38-S45.e5.

[44] Jackson JB, Feredoes E, Rich AN, Lindner M, & Woolgar A. Concurrent neuroimaging and neurostimulation reveals a causal role for dlPFC in coding of task-relevant information. Communications Biology, 2021:4(1).

[45] Javadi AH, Emo B, Howard LR, Zisch FE, Yu Y, Knight R, et al. Hippocampal and prefrontal processing of network topology to simulate the future. Nature Communications. 2017;8.

[46] Jensen O, Mazaheri A. Shaping functional architecture by oscillatory alpha activity: Gating by inhibition. Frontiers in Human Neuroscience. 2010;4(November):1–8.

[47] Jia N, Brincat SL, Salazar-Gómez AF, Panko M, Guenther FH, Miller EK. Decoding of intended saccade direction in an oculomotor brain-computer interface. Journal of Neural Engineering. 2017;14(4).

[48] Johnston R, Abbass M, Corrigan B, Gulli R, Martinez-Trujillo J, Sachs A. Decoding spatial locations from primate lateral prefrontal cortex neural activity during virtual navigation. Journal of Neural Engineering. 2023;20(1).

[49] Johnston R, Doucet G, Boulay C, Miller K, Martinez-Trujillo J, Sachs A. Decoding Saccade Intention from Primate Prefrontal Cortical Local Field Potentials Using Spectral, Spatial, and Temporal Dimensionality Reduction. International Journal of Neural Systems. 2021;31(6):1–19.

[50] Jones MW, Wilson MA. Theta rhythms coordinate hippocampal-prefrontal interactions in a spatial memory task. PLoS Biology. 2005;3(12):1–13.

[51] Jung MW, Qin Y, McNaughton BL, Barnes CA. Firing characteristics of deep layer neurons in prefrontal cortex in rats performing spatial working memory tasks. Cerebral Cortex. 1998;8(5):437–50.

[52] Kandel, E. R. Principles of Neural Science (5th ed.). McGraw Hill Professional. 2013:22-23.

[53] Kim H. Neural activity during working memory encoding, maintenance, and retrieval: A network-based model and meta-analysis. Human Brain Mapping. 2019;40(17):4912–33.

[54] Klauer KC, Zhao Z. Double dissociations in visual and spatial short-term memory. Journal of Experimental Psychology: General. 2004;133(3):355–81.

[55] Kögel J, Schmid JR, Jox RJ, Friedrich O. Using brain-computer interfaces: A scoping review of studies employing social research methods. BMC Medical Ethics. 2019;20(1):15–7.

[56] Kübler A, Nijboer F, Mellinger J, Vaughan TM, Pawelzik H, Schalk G, et al. Patients with ALS can use sensorimotor rhythms to operate a brain-computer interface. Neurology. 2005;64(10):1775–7.

[57] Lega BC, Jacobs J, Kahana M. Human hippocampal theta oscillations and the formation of episodic memories. Hippocampus. 2012;22(4):748–61.

[58] Lennert T, Martinez-Trujillo JC. Prefrontal neurons of opposite spatial preference display distinct target selection dynamics. Journal of Neuroscience. 2013;33(22):9520–9.

[59] Logan G, Van Zandt T, Verbruggen F, Wagenmakers E. On the ability to inhibit thought and action: General and special theories of an act of control. Psychology Review. 2014;121(1):66–95.

[60] Manning JR, Jacobs J, Fried I, Kahana MJ. Broadband shifts in local field potential power spectra are correlated with single-neuron spiking in humans. Journal of Neuroscience. 2009;29(43):13613–20.

[61] McMullen D, Thomas TM, Fifer MS, Candrea DN, Tenore F V, Nickl RW, et al. Novel intraoperative online functional mapping of somatosensory finger representations for targeted stimulating electrode placement. medRxiv. 2020.

[62] Milekovic T, Sarma AA, Bacher D, Simeral JD, Saab J, Pandarinath C, et al. Stable long-term BCI-enabled communication in ALS and locked-in syndrome using LFP signals. Journal of Neurophysiology. 2018;120(1):343–60.

[63] Miller EK, Erickson CA, Desimone R. Neural mechanisms of visual working memory in prefrontal cortex of the macaque. Journal of neuroscience. 1996 Aug 15;16(16):5154-67.

[64] Miller EK, Lundqvist M, Bastos AM. Working Memory 2.0. Neuron. 2018;100(2):463–75.

[65] Miller KJ, Zanos S, Fetz EE, Den Nijs M, Ojemann JG. Decoupling the cortical power spectrum reveals real-time representation of individual finger movements in humans. Journal of Neuroscience. 2009;29(10):3132–7.

[66] Moran DW, Schwartz AB. Motor cortical representation of speed and direction during reaching. Journal of Neurophysiology. 1999;82(5):2676–92.

[67] Nam, C. S., Nijholt, A., Lotte, F. Brain-Computer Interfaces Handbook: Technological and Theoretical Advances. CRC Press.2018.

[68] O'Keefe J, Dostrovsky J. Short Communications The hippocampus as a spatial map. Preliminary evidence from unit activity in the freely-moving rat. Brain Research [Internet]. 1971;34(1):171–5.

[69] Pandarinath C, Nuyujukian P, Blabe CH, Sorice BL, Saab J, Willett FR, et al. High performance communication by people with paralysis using an intracortical brain-computer interface. eLife [Internet]. 2017 Feb 21;6.

[70] Penfield W, Jasper H. Epilepsy and the functional anatomy of the human brain. Little, Brown & Co, Boston, Mass, 1954.

[71] Petrides M, Pandya D.N. Dorsolateral prefrontal cortex: comparative cytoarchitectonic analysis in the human and the macaque brain and corticocortical connection patterns. European Journal of Neuroscience. 1999;11(6):1011–36.

[72] Posner MI. Orienting of attention. The Quarterly journal of experimental psychology. 1980;32(1):3–25.

[73] Ramsey NF, Heuvel MP Van De, Kho KH, Leijten FSS. Towards Human BCI Applications Based on Cognitive Brain Systems: An Investigation of Neural Signals Recorded From the Dorsolateral Prefrontal Cortex. IEEE Transactions on Neural Systems and Rehabilitation Engineering. 2006;214–7.

[74] Ramsay, J., & Silverman, B. W. Functional data analysis (Springer series in statistics). 1997.

[75] Rolls ET, Wirth S. Spatial representations in the primate hippocampus, and their functions in memory and navigation. Progress in Neurobiology [Internet]. 2018;171(September):90–113.

[76] Rolls ET, Xiang JZ. Spatial View Cells in the Primate Hippocampus, and Memory. Hippocampal Place Fields: Relevance to Learning and Memory. 2006;200:175–200.

[77] Roux F, Uhlhaas PJ. Working memory and neural oscillations: Alpha-gamma versus theta-gamma codes for distinct WM information? Trends in Cognitive Sciences. 2014;18(1):16–25.

[78] Roux F, Wibral M, Mohr HM, Singer W, Uhlhaas PJ. Gamma-band activity in human prefrontal cortex codes for the number of relevant items maintained in working memory. Journal of Neuroscience. 2012;32(36):12411–20.

[79] Rowe JB, Toni I, Josephs O, Frackowiak RSJ, Passingham RE. The prefrontal cortex: Response selection or maintenance within working memory? Science Magazine. 2000;288:1656–60.

[80] Schiff ND, Giacino JT, Butson CR, Choi EY, Baker JL, Sullivan KPO, et al. Thalamic deep brain stimulation in traumatic brain injury : a phase 1 , randomized feasibility study. Vol. 29. Springer US; 2023.

[81] Shlens J. A Tutorial on Principal Component Analysis. 2014; Available from: http://arxiv.org/abs/1404.1100

[82] Sitaram R, Caria A, Veit R, Gaber T, Rota G, Kuebler A, et al. fMRI Brain-Computer Interface: A Tool for Neuroscientific Research and Treatment. Hindawi Publishing Corporation; 2007.

[83] Spellman T, Rigotti M, Ahmari SE, Fusi S, Gogos JA, Gordon JA. Hippocampal-prefrontal input supports spatial encoding in working memory. Nature. 2015;522(7556):309–14.

[84] Spiers HJ, Hayman RMA, Jovalekic A, Marozzi E, Jeffery KJ. Place field repetition and purely local remapping in a multicompartment environment. Cerebral Cortex. 2015;25(1):10–25.

[85] Stoll FM, Wilson CRE, Faraut MCM, Vezoli J, Knoblauch K, Procyk E. The Effects of Cognitive Control and Time on Frontal Beta Oscillations. Cerebral Cortex. 2016;26(4):1715–32.

[86] Tallon-Baudry C, Bertrand O, Peronnet F, Pernier J. Induced γ-band activity during the delay of a visual short-term memory task in humans. Journal of Neuroscience. 1998;18(11):4244–54.

[87] Tremblay S, Doucet G, Pieper F, Sachs A, Martinez-Trujillo J. Single-trial decoding of visual attention from local field potentials in the primate lateral prefrontal cortex is frequency-dependent. Journal of Neuroscience. 2015;35(24):9038–49.

[88] Tremblay S, Pieper F, Sachs A, Martinez-Trujillo J. Attentional Filtering of Visual Information by Neuronal Ensembles in the Primate Lateral Prefrontal Cortex. Neuron. 2015;85(1):202–15.

[89] Vansteensel MJ, Hermes D, Aarnoutse EJ, Bleichner MG, Schalk G, Van Rijen PC, et al. Brain-computer interfacing based on cognitive control. Annals of Neurology. 2010;67(6):809–16.

[90] Wang GW, Cai JX. Disconnection of the hippocampal-prefrontal cortical circuits impairs spatial working memory performance in rats. Behavioural Brain Research. 2006;175(2):329–36.

[91] Willett FR, Avansino DT, Hochberg LR, Henderson JM, Shenoy KV. High-performance brain-to-text communication via handwriting. Nature. 2021 May 13;593(7858):249-54.

[92] Wodlinger B, Downey JE, Tyler-Kabara EC, Schwartz AB, Boninger ML, Collinger JL. Ten-dimensional anthropomorphic arm control in a human brain-machine interface: Difficulties, solutions, and limitations. Journal of Neural Engineering [Internet]. 2015;12(1):16011.

[93] Wolpaw JR. Chapter 6 – Brain–computer interfaces [Internet]. 1st ed. Vol. 110, Handbook of Clinical Neurology. Elsevier B.V.; 2013. 67–74.

[94] Wallis JD, Anderson KC and Miller EK. Single neurons in prefrontal cortex encode abstract roles. Nature. 2001;411:953–956.

[95] Wang Y, Fifer MS, Flinker A, Korzeniewska A, Cervenka MC, Anderson WS, Boatman-Reich DF, Crone NE. Spatial-temporal functional mapping of language at the bedside with electrocorticography. Neurology. 2016;86(13):1181–9.

[96] Yuste R. From the neuron doctrine to neural networks. Nature Reviews Neuroscience [Internet]. 2015;16(8):487–97.

Chapter 2

Decoding Saccade Intention from Primate Prefrontal Cortical Local Field Potentials Using Spectral, Spatial, and Temporal Dimensionality Reduction

2.1 Abstract

Most invasive Brain Computer Interfaces (iBCIs) use spike and Local Field Potentials (LFPs) from the motor or parietal cortices to decode movement intentions. It has been debated whether harvesting signals from other brain areas that encode global cognitive variables, such as the allocation of attention and eye movement goals in a variety of spatial reference frames, may improve the outcome of iBCIs. Here we explore the ability of LFP signals, sampled from the lateral prefrontal cortex (LPFC) of macaque monkeys, to encode eye-movement intention during the pre-movement fixation period of a delayed saccade task. We use spectral dimensionality reduction to examine the spatiotemporal properties of the extracted non-rhythmic broadband activity and explore its usefulness in decoding saccade goals. The dynamics of the broadband signal in low spatial dimensions across the pre-movement fixation period uncovered saccade target separation; its discriminative potential was confirmed using support vector machine classifications. These findings reveal that broadband LFP from the LPFC can be used to decode intended saccade target location during pre-movement periods. We further provide a general workflow that can be implemented in iBCIs and it is relatively robust to the loss of spikes in individual electrodes.

2.2 Introduction

Clinical implementations of invasive brain computer interfaces translate neural activity into effector control to restore function to severely disabled individuals (Santhanam et al. 2006, Flint

et al. 2012, Pandarinath et al. 2017, Ajiboye et al. 2017, Willett et al. 2021). The majority of clinical iBCI implementations decode movement intention from neuronal activity in the motor cortex (Georgopoulos et al. 1986, Shenoy et al. 2013, Collinger et al. 2013, Corsi et al. 2019, Barios et al. 2019). Alternatively, recent studies used cognitive signals from motor or associative cortices to decode discrete movement intentions (Fan et al. 2014), states (Sumsky et al. 2017, Kao et al. 2017), transitions (Kang et al. 2015), and goals (Andersen et al. 2019, Shanechi et al. 2013). This may allow the iBCI system to better guide effectors considering the overall intention of an action, instead of relying solely on specific movement commands emanating from primary motor cortex. However, identifying the user's intention requires integrating information associated with planning, working memory, attention, and the decision state. The LPFC (areas 8A, 9 and 46) has been associated with integrating cognitive variables essential to goal directed voluntary behaviors, such as attention, working memory, target selection and learning (Tremblay et al. 2015, Mendoza-Halliday and Martinez-Trujillo 2017, Petrides and Pandya 1999, Petrides 2005, Miller et al. 1996, Miller and Cohen 2001). Therefore, LPFC has been proposed to be an appropriate signal source for a goal selective cognitive BCI (Boulay et al. 2016). Here we expand on the temporal dynamics and suitability of signals extracted from primate LPFC as candidates for cognitive iBCIs.

The spatial extent of signals acquired by iBCIs can vary from ~0.5 cm in electrocorticography (ECoG), to sub-millimeter in single neuron micro-electrode recordings (Ortiz-Rosario and Adeli 2013). However, isolating the electrical signal from single neurons with a micro-electrode is not always achievable, and signal quality inevitably degrades over time (Dickey et al. 2009). LFPs recorded from micro-electrodes could potentially provide a reasonable trade-off between the relative benefits of ECoG and single units. For example, LFPs have a much higher spatial

resolution and signal to noise ratio than ECoG. Furthermore, the LFP is more reliable and stable than single neuron activity (Milekovic et al. 2015). It is likely to remain viable after degradation of the spikes, thus lengthening the useful duration of the iBCI implant. Recent studies have therefore examined the utility of decoding movement intentions from motor cortex LFPs (Milekovic et al. 2015, Heldman and Moran 2020, Zhuang et al. 2010, Burns et al. 2014, Ortiz-Rosario et al. 2015). These studies demonstrate that the decoding accuracy obtained from using features based on LFPs can approach the accuracy obtained from those based on trains of action potentials (spikes).

There are comparatively fewer studies examining the utility of LFPs from non-motor cortices in iBCIs. Markovitz et al. (2011) investigated the possibility of decoding eye movement goals from LFPs extracted from macaque LPFC and demonstrated that the best decoder accuracy was obtained with shallow recording sites and for contralateral targets. Tremblay et al. (2015) showed that intracortical LFPs recorded from microelectrode arrays (MEAs) in LPFC of non-human primates, contain frequency-dependent information about sensory, cognitive, and motor signals. Moreover, Boulay et al. (2016) demonstrated that spike rates simultaneously recorded from multiple neurons of LPFC MEAs can be used to accurately decode saccadic eye movement goals.

Neural networks within the brain are organized in complex combinations of staged processing, with feedback, and feedforward mechanisms. This combination of staging and recursion, with different delays related to synaptic processing, gives rise to two dominant spectral motifs in the LFP: synchronous (narrow band) and asynchronous (broadband) neuronal activity. A previous study suggested that broadband shifts in the LFP power spectra are good predictors of local neuronal spiking (Manning et al. 2009). Accordingly, Miller et al. (2009) reported that broad

spectral changes in ECoG signals revealed spatially distinct representation for individual fingers and were dynamically modulated with high temporal resolution. They further argue that extracting the broadband spectral motif from the larger spatial scale of field potentials can benefit decoding by resolving overlapping high-frequency neuronal responses.

We first set out to determine whether eye movement goals could be decoded from the broadband component of the intracortical LFPs recorded from LPFC area 8A of macaques. To do so, we used a delayed saccade task, which is simple while also engaging the inhibitory mechanisms of the prefrontal cortex during the movement preparation. We focused on decoding the intended saccade target location without identifying the complex underlying sensory and cognitive mechanisms, which could include visual, motor, attention, and memory responses. We found that, during movement preparation, broadband LFP power increased, with no change in oscillatory activity. Moreover, these power modulations reliably encoded the target location.

We then integrated the spectral decomposition step into a novel dimensionality reduction workflow to optimize decoding in an iBCI setting. This workflow extracts features from the raw LFP signal using spectral, spatial, and temporal dimensionality reductions. The spectral processing was used to isolate the broadband activity from the raw LFPs. The spatial analysis provided weights for the active electrodes that maximized the separation of saccade target locations across the fixation period. The temporal dimensionality reduction was finally used to extract the non-stationary components of this activity over time. We show that our workflow (1) provides comparable or better decoding performance than averaged broadband LFPs, (2) optimizes decoding efficiency by reducing features sets, (3) is robust to novel data, and (4) is stable over

time. These results further confirm the importance of optimizing the broadband, asynchronous, LFP activity in BCI applications.

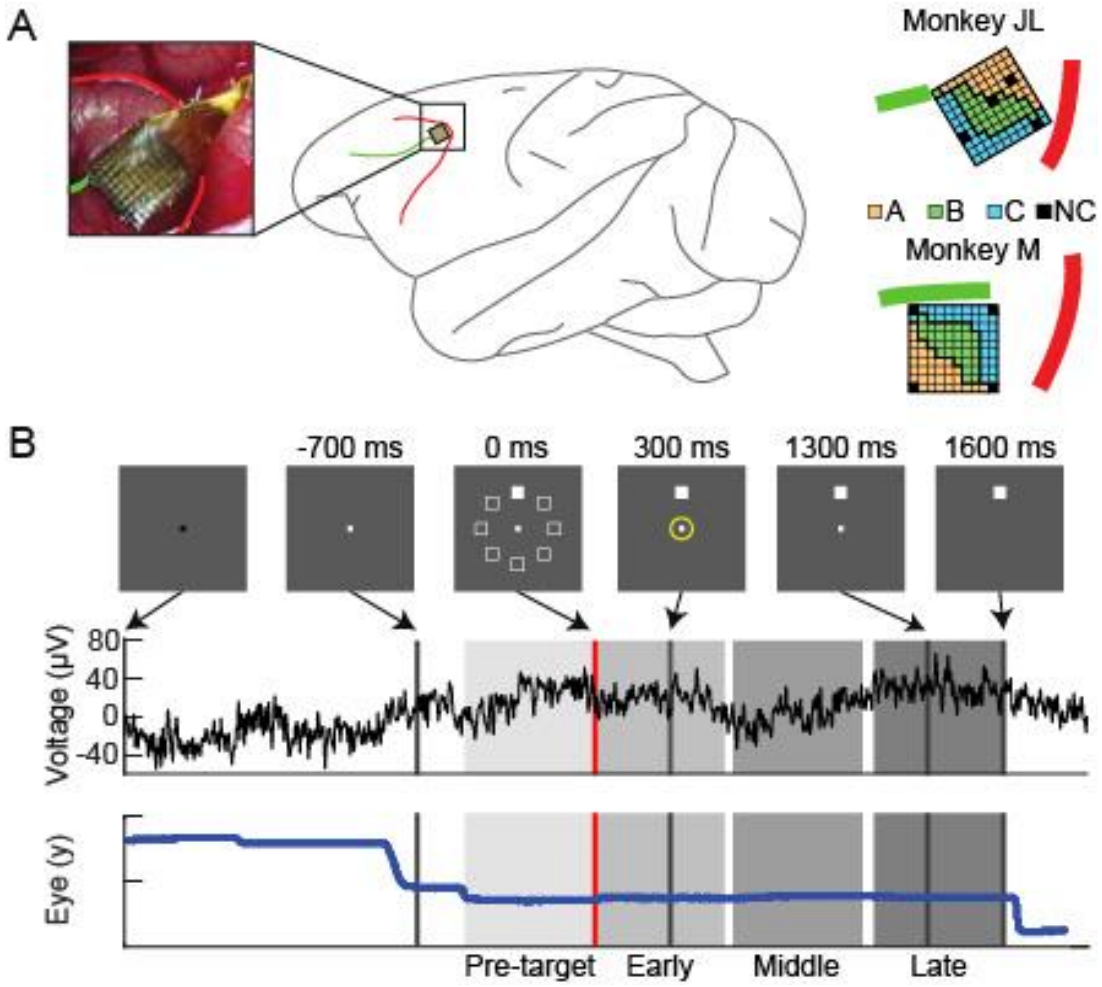

Figure 4. Experimental Approach. (A) The MEA is implanted in LPFC area 8A in a *Macaca fascicularis*. As described by Boulay et al. (2016), the MEA arrays are positioned on the monkey's cortex, anterior to the arcuate sulcus (red line) and caudal to the principal sulcus (green line). Each recording session captured activity from a set of 32 electrodes represented by A-B-C (NC refers to unused electrodes). (B) Data from an exemplary trial illustrate the task and data segmentation. The top row represents the visual information displayed to the monkey on a video projector at different stages of the trial (note that at time t=0 ms, only one of the possible 8 targets is displayed). The middle row shows the recorded LFP signal from one electrode of the array during this trial. The shaded grey windows represent the four segmented epochs defined as pre-target fixation followed by early, middle, and late fix with target. The bottom row shows the vertical tracing (y-axis component) of the monkey's eye position. The black vertical bars indicate the time of the trial events when the presented display changes, including trial initiation, fixation acquired, target onset at t=0 (red vertical bar), irrelevant cue onset and offset, and fixation offset which triggers the saccade event.

2.3 Methods

All the experimental protocols and procedures were in compliance with the rules and regulations of Canada and were approved by the McGill University Animal Care committee in 2006 and renewed yearly thereafter. On average, the animals were trained approximately six months followed by one year where they participated in experiments for this and other studies.

2.3.1 Stimulus and tasks details

Two *Macaca fascicularis* ("JL" and "M"; Figure 4A), were trained to perform a delayed saccade task (Figure 4B). Visual stimuli were generated using The Psychophysics Toolbox (Brainard 1997) with MATLAB, and presented on a video projector (NEC WT610, 1024 x 768 pixels, 85 Hz) 100 cm from the animal's eyes. During each experimental trial, lasting approximately 2 to 6 seconds, the monkeys were required to execute the following steps outlined in the top row of Figure 4B:

(i) Fixate gaze on a central fixation point which was a black square with a length of 0.2 degrees of visual angle (DVA). The trial initiation was visually indicated to the animal by a change in the color of the fixation point from black to white (t = -700 ms).

(ii) Keep gaze on the white central fixation point for 700 ms.

(iii) Maintain fixation while a 5.1 DVA square target appeared in one of eight radially arranged positions (45˚ steps) with their centers 12.7 DVA eccentric to the fixation point (t = 0 ms).

(iv) Prepare for the saccade by maintaining gaze on the fixation square for the following delay period of 1600 ms. During this time, a red, blue, or yellow annulus with a radius of 1.3 DVA would appear (t =300 ms) and remain visible for 1000 ms (t = 1300 ms). This cue was irrelevant to the task but acted as a non-directional visual distraction for the animal.

(v) Make a saccade to the displayed target within 200ms after the disappearance of the fixation point (t = 1600 ms).

(vi) Hold fixation at the target for 200 ms to then be rewarded with a sip of water or juice.

If the monkey broke fixation prior to the disappearance of the fixation point or did not directly gaze to the target after the fixation point vanished, the trial was considered an error trial, and the monkey did not receive its reward (Boulay et al. 2016). The monkeys were trained using standard operant conditioning. In the first few weeks, they would receive a reward for fixating on a central point. The time that the fixation was required would then be gradually increased. After this was well learnt, a second target would appear, and the reward would be held until the monkey would saccade to the second point once the fixation point would disappear. This experiment is intuitive and follows a primate's tendency to fixate on a salient feature. It was therefore a relatively simple task to train, and monkeys performed the task well (Table 3). Overall, the number of trials per target ranged from 7 for monkey JL – Block B (session 1) to 61 for monkey M – Block B. Observe that in Table 3 we are considering as errors all the trials the animal broke fixation on the central spot before the fixation point disappeared as well as those in which the saccade landed outside the target window. In some sessions the animals made many errors but mainly due to fixation breaks rather than landing outside the target window.

Table 3. Experiment session description detailing number of successful and failed trials with time offset from the recording of the first session (D1).

Monkey	Block of session	#Success Trials	#Failed Trials	Time (days)
JL	A	199	103	D38
JL	B session1	54	17	D1

JL	B session2	185	60	D36
JL	C	175	59	D37
M	A	250	98	D61
M	B	484	121	D69
M	C	216	44	D72

2.3.2 Apparatus and recording procedures

After successfully training the monkeys to sit in a primate chair, we implanted 3 small head posts on the skull. One was placed posterior to the supra-orbital ridge in the sagittal plane, the other two on the petrosal bone superior to the external occipital protuberance behind the left and right ear. The head posts interfaced with a circular halo-like aluminum head holder to fix the monkeys' head to the chair. The animals were trained to allow the experimenter to attach the head to the holder, avoiding head movements during the recording sessions. The holder allowed access to the top of the head, where the array-interface (pedestal) would be implanted. Eye-positions were collected and saved to disk using an infrared camera-based eye-tracker (EyeLink 1000, SR Research, Ontario, Canada).

2.3.3 MEA implants

We surgically implanted a 10×10 electrode array ('Utah-Probe'; Rousche and Normann, 1999) in the monkey's left LPFC anterior to the knee of the arcuate sulcus and caudal to the posterior end of the principal sulcus as shown in Figure 4A. The electrode tips were separated by at least 0.4 mm. Each electrode array contained three 32-channel subsets (Blocks A, B, C) and in each recording session we exclusively collected the data of one block of 32 electrodes (Table 3). The latter was due to a limitation in the number of recording channels our hardware had. The block

separations and unused electrodes within the MEA are unique to each array and hardwired by the manufacturer. The data was recorded using a Cerebus Neuronal Signal Processor (Blackrock Microsystems LLC, Utah, USA) *via* a Cereport adapter.

2.3.4 LFP acquisition and processing

We first did a 1x amplification in the headstage (ICS-96), after which the neuronal signal was band-pass filtered (analog Butterworth filter; 0.3 Hz/1-pole - 7.5 kHz/3-pole) and digitized (16 bit; 1µV per bit) at 30 kHz. Prior to analysis, the LFPs were downsampled to 1 kHz using a 4th-order Butterworth anti-aliasing filter with a 250 Hz cutoff frequency. The LFP signal *V*, from each electrode *n* at time *t*, was then re-referenced to the common average such that,

$$V_n(t) = V_n^0(t) \; - \; 1/N \; \sum_{i=1}^{N} V_i^0(t). \qquad (1)$$

In Eq. (1), V_n^0 is the original LFP signal and N=32 channels. To reduce the effect of ambient line noise, we used a 3rd-order Butterworth notch filter between 58 to 62 Hz (Porat, 1997). To analyze the LFP activity dynamics, a set of 4 different 512 ms epochs (q) was extracted from each trial. We defined τ_q for epoch q as the midpoint of the window relative to the target onset for each epoch: pre-target (τ_q = -256 ms), early (256 ms), middle (800 ms), and late (1344 ms). The following steps were subsequently applied to each electrode. The power spectral density (PSD) was calculated as:

$$P(f,q) = \left| \frac{1}{\sqrt{T}} \sum_{t=-\frac{T}{2}}^{\frac{T}{2}} V\left(\tau_q + \; t\right) H(t)\, e^{i2\pi f t} \right|^2 \qquad (2)$$

where T = 512 ms, f are the frequencies ranging from 1.95Hz to 500 Hz (size 256), and $H(t)$ is a Hann window of the form

$$H(t) = \frac{1}{2}\left(1 - \cos\left(\frac{2\pi t}{T}\right)\right). \qquad (3)$$

The power spectrum decoupling process is described in detail by Miller et al. (2009). Briefly, the PSD samples were normalized prior to decomposition such that:

$$\hat{P}(f,q) = \ln\big(P(f,q)\big) - \ln\left(\frac{1}{N_q}\sum_q P(f,q)\right) \quad (4)$$

where ln represents the natural logarithm, N_q is the number of windows considered (Number of epochs (4) x Number of trials). Frequencies below 200 Hz were retained, while those around power noise harmonics [58-62 Hz, 118-122 Hz, 178-182 Hz] were removing, adjusting its size to from 256 to 93. Principal component analysis (PCA; Jolliffe, 2002) was then applied to determine the eigenvalues λ_k and eigenvectors $\vec{e}_k$ of the correlation,

$$\hat{C}(f,f') = \sum_q \hat{P}(f,q)\hat{P}(f',q) \qquad (5)$$

such that $\hat{C}\vec{e}_k = \lambda_k\vec{e}_k$. We define the rotation matrix $A(f,k) = (\vec{e}_1, \ldots, \vec{e}_{N_f})$. The projections of the original spectrum onto the new basis vector *k* are:

$$W(k,q) = \sum_f A(f,k)\hat{P}(f,q). \qquad (6)$$

The first principal spectral component (PSC #1) refers to the projection of the power spectrum onto the first eigenvector $\vec{e}_1$ and the second principal spectral component (PSC #2) refers to the projection of the spectrum onto the second eigenvector $\vec{e}_2$. Using the inverse rotation matrix $\hat{A}^{-1}$, we may reconstruct the power spectra using a subset of principle spectral components, *X*, as:

$$\hat{P}_X(f,q) = \sum_{k\in X} A^{-1}(f,k)W(k,q). \qquad (7)$$

2.3.5 Continuous PSC #1 during movement preparation

The dominant spectral motifs can be obtained by doing a PCA on the 1 kHz normalized LFP spectra as described in the previous section. To analyze the continuous PSC #1 behavior during movement preparation, we computed the PSD using a 512 ms sliding window across the entire movement preparation phase. The center of the moving window started at target onset (t = 0 ms) and stopped at the imperative cue which triggers the saccade (t = 1600 ms) in 1 ms steps. We then extracted the PSC #1 magnitude from the spectrum at each step to obtain the continuous PSC #1.

2.3.6 Classification methodology

Throughout the paper, we used a support vector machine (SVM) algorithm, with a linear kernel, to evaluate the decoding accuracy obtained from PSC #1 based features. We used the LIBLINEAR (Fan et al. 2008) implementation of the L2-regularized, L2-loss support vector classification, with 5-fold cross-validation which automatically optimizes the model parameters to best decode intended saccade targets. Some of our sessions had a low number of successful trials for a given target location, we chose 5-fold cross-validation since it provided a good balance to validate accuracy for all target locations while keeping a low computational requirement.

2.3.7 Statistics

To determine the statistical difference of PSC #1 distributions between epochs and targets, we confirmed with the Anderson-darling statistical test (Anderson and Darling, 1952) that the data points were not normally distributed. This led us to use the non-parametric Wilcoxon rank sum test (exact method; Wilcoxon, 1945), to determine if the PSC #1 distributions are significantly different between epochs and between target locations.

To allow for statistical comparisons of decoding method accuracies, we generated accuracy distributions by averaging the 5-fold cross-validation results of each SVM iteration and repeating the procedure 1,000 times. For each method, we established the chance level by shuffling the target labels before running SVM (1,000 times) which provided us with the null distribution for this method. To evaluate if the decoding methods were significantly different than the others, we subtracted the mean of the associated null distribution for each method and ran the Wilcoxon rank sum test on the resulting 1,000-point distributions. Since most methods showed very low p-values, we decided to perform the Cohen's d effect size (Cohen, 1988) between those distributions. We set the statistically significant threshold at $p < 0.01$ and used the * symbol to highlight this property in our results. Highly significant results ($p < 0.001$) are represented by ***.

2.3.8 Greedy electrode-adding procedure

To determine the maximal decoding accuracy obtainable from our dataset, we performed a greedy electrode-adding procedure. We first found the individual channel providing the best SVM decoding accuracy using features based on the continuous PSC #1 during movement preparation. Then looking at the combinations of this chosen channel with all the other channels, we selected the pair that provided the best decoding accuracy. The remaining individual electrodes were then added to the pair, and the best trio was selected. This procedure was repeated until all remaining electrodes were included, maximizing decoding results at each step.

2.3.9 Spatial processing using canonical discriminant analysis

A linear model was first fitted using the function "lm" included in the R stats package (Chambers 1992, Wilkinson and Rogers 1973) within the RStudio environment. For each session, we used

this function to perform a multivariate two-way analysis of variance. The multiple linear regression model formula was defined as:

$$Y = \beta_0 + \beta_1 X_1 + \beta_2 X_2 + \beta_3 X_3, \qquad (8)$$

where $\beta_0, \beta_1, \beta_2, \beta_3$ are the regression coefficients,

β_0 is the line intercept (size 1 x 32 channels),

β_1 (size 3 (epochs 2,3,4) x 32 channels),

β_2 (size 7 (targets 2 to 8) x 32 channels),

β_3 (size 21 (target:epoch interactions) x 32 channels),

Y is the broadband activity (1 x 32 channels)

X_1 (size 1x3), X_2 (size 1x7), X_3 (size 1x21) are the independent variables which respectively refer to the epochs (2 to 4), target locations (2 to 7), and their interactions.

Using this model, we focused on specific terms (e.g., the epoch-target interaction or the target location) and performed a canonical discriminant analysis (Ramsay and Silverman, 1997), to find the linear combination of electrodes that maximized these interactions. The goal of this analysis was to reduce the spatial dimensions of the model. Like the dimensionality reduction from a PCA which aims to preserve the data-variance, this technique derives canonical vectors that maximize between-class variations. The function "candisc" from the R candisc package (Friendly and Fox, 2020) was used to perform this generalized canonical discriminant analysis of the fitted linear model for the target term or for the epoch-target interaction term.

2.3.10 Temporal dimensionality reduction of continuous broadband LFP

To investigate the continuous temporal dynamics of the broadband activity across the movement preparation period of the saccade task, the following steps were taken:

(i) Calculate the PSC #1 for every window of 512 ms at every timepoint (1 ms step) across the fixation period (see section 2.3.5).

(ii) Project the resulting broadband activity of all electrodes on the canonical vectors based on the epoch-target interactions or target factor (see section 2.3.9).

(iii) Perform the PCA (on the array made of the projections of PSC1 on a canonical vector at every step of the movement preparation period x number of trials) to extract the low-dimensional temporal component for each considered canonical vector.

The resulting data from the canonical discriminant analysis could then be projected onto these temporal PC vectors to obtain a single feature value per trial to be used in SVM decoding.

2.3.11 Feature sets for decoding target locations

We compared the SVM decoding performance of 4 different feature sets to better understand the relative trade-offs between dimensionality reduction techniques.

- Method1 (M1): Features are the calculated PSC #1 of four separated 512 ms fixation epochs (pre-target, early, middle, and late fixation) for every trial. This method uses spectral dimensionality reduction only. The resulting number of features equals to #trials x (32 channels x 4 epochs).
- Method2 (M2) and Method3 (M3): Features used for these methods utilize the spectral, spatial, and temporal dimensionality reduction of the LFPs. First, the continuous PSC #1 data are projected on the predefined canonical vectors. Method 2 uses 7 canonical vectors specialized in discriminating target locations, while method 3 uses the top 11 canonical vectors specialized

in discriminating epoch-target interactions. The resulting vectors are further projected on the first temporal PC vector. The resulting feature set size is equal to #trials x #canonical vectors.

- Method4 (M4): Features are the average of the continuous PSC #1 for every electrode, without spatial and temporal dimensionality reductions. The resulting number of features equals #trials x 32 electrodes.

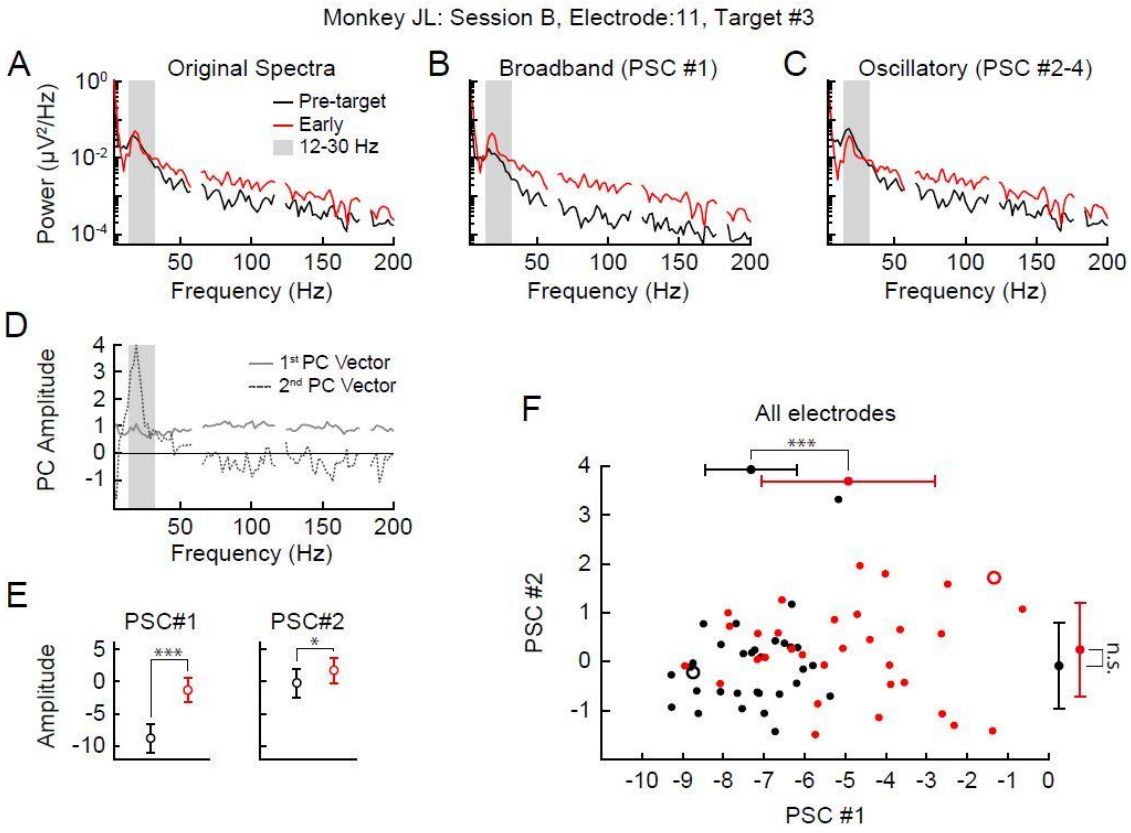

Figure 5. LFP-based broadband feature is modulated during the task. (A) shows the averaged PSD for the trials associated with target #3 on electrode #11, during pre-target (black) and early fixation (red). This PSD was decoupled and reconstructed into (B) broadband power (using PSC #1) and (C) oscillatory/narrow-band power (using PSC #2-4). (D) plots the PCA first and second eigenvectors used to reconstruct the PSD. (E) represents the mean and standard deviation of PSC #1 and PSC #2 for pre-target and early fixation epochs. (F) shows the population LFP analysis where PSC #1 is plotted against PSC #2 for all electrodes. The mean and standard deviation of the population are shown on the outside border (Note that the larger circle represents electrode #11 activity).

2.4 Results

2.4.1 Spectral dimensionality reduction of LFP

The PSD of the LFP differed markedly between the pre-target and early fixation with target epochs. In many channels, averaged spectral power in frequencies above the beta range (12 – 30 Hz) was increased during the early compared to the pre-target epochs. To illustrate this difference in the frequency spectrum and its principal components, we selected the signal from one electrode, averaged over the trials associated with a specific target location. Figure 5A shows the original PSD of electrode #11 (chosen because the effects are clearly demonstrated) for pre-target fixation (black trace) and early fixation during movement preparation (red trace) epochs. To determine if these observations are the result of an increase of oscillatory power in frequency above 40Hz or an increase in the broadband power, we assessed the PSD of these LFP motifs individually.

Miller et al. (2014) demonstrated theoretically and empirically from ECoG recordings that the PSC #1 reflects broadband, non-oscillatory, components of the power spectrum, whereas the PSCs #2-4 reflect the oscillatory power which refers to narrow-band activity. Therefore, these eigenvector-based power spectrum reconstructions can allow one to delineate between spectral changes due to oscillatory and non-oscillatory power. PSDs reconstructed from the PSC #1 reflected broadband activity (Figure 5B) whereas PSDs reconstructed from the 2^{nd} to 4^{th} components reflected narrow-band oscillatory activity (Figure 5C). This separation was also evident in the corresponding PCA vectors (Figure 5D). The broadband power increase observed in the PSDs is well-represented by PSCs #1 (Figure 5E). While PSC #2 amplitudes were significantly different for electrode 11, they were not when looking across all electrodes for the same target (Figure 5F). On the other hand, the two epochs were well discriminated by PSC #1 magnitudes across all electrodes (Figure 5F). These

results suggest that the broadband activity as reflected in PSC #1 may be a suitable feature to decode intended saccade direction because it demonstrates task-related modulation in the pre-saccadic period.

We expanded our analyses to the four different trial epochs and the eight target locations. The variance analysis for monkey JL electrode #11 (Table 4, black values) and monkey M electrode #7 (Table 4, blue values) showed that PSC #1 varied across multiple trial epochs and target locations. For monkey JL (electrode #11), it was greater during early, middle, and late epochs than

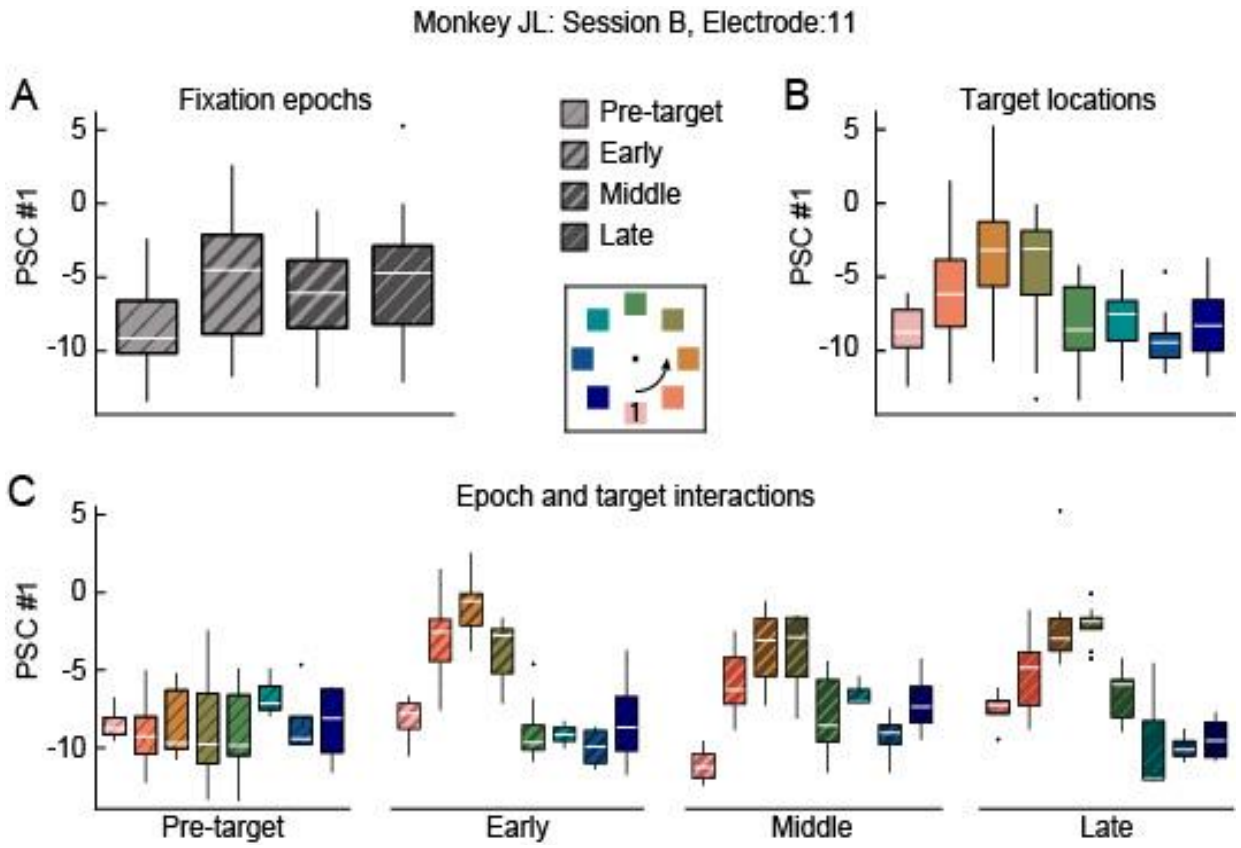

Figure 6. Variance Analysis and Individual electrode target selectivity. Specific to electrode #11 of a session with monkey JL, the analysis of variance is shown for (A) fixation epochs "Pre-target", "Early", "Middle" and "Late" where each epochs is associated to a box texture, (B) saccade target locations where the target locations are color coded, and (C) the epoch-target interactions. The color and texture legend for epochs and target locations is inserted between (A) and (B).

during the pre-target epoch but there were no differences among early, middle, and late epochs (Table 4 and Figure 6A). PSC #1 also discriminated the various target locations in both monkeys (Table 5). PSC #1 distributions across all targets for monkey JL electrode #11 are presented in Figure 6B. Consistent with these results, there was a significant interaction between epochs and targets, with PSC #1 magnitude being greatest for the contralateral targets during early, middle, and late epochs (Figure 6C). Various selectivity profiles were found for both epochs and targets across numerous electrodes for each monkey, suggesting that it could be beneficial to use spatially distributed processing of task related information across the MEAs. A previous study has shown individual neurons selectivity distributed over the different array channels for different trial epochs of a visually guided saccade (Bullock et al. 2017). However, it is not currently clear whether there is a 'topography' concerning task epochs and target locations in this area.

2.4.2 Spatial dimensionality reduction of broadband activity

In higher cortical areas, the local and neuronal activity show mixed selectivity, implying that those neurons are often tuned to more than one task related variable (Kobak et al. 2016). The purpose of the spatial dimensionality reduction analysis was to evaluate how the PSC #1 information about an upcoming saccade's target was distributed over the MEAs. We used the mean of the continuous PSC #1 amplitude, calculated during the movement preparation period, to evaluate SVM decoding performance for all eight target locations. The SVM decoding accuracy refers to the averaged five-fold cross-validation SVM results. Figure 7A shows the mean and standard deviation for individual electrodes decoding accuracy for all sessions (note that monkey JL Block A has seven possible targets hence overall higher performance).

Table 4. Pairwise Wilcoxon rank sum test P-values for considered fixation epochs. Black: Monkey JL - Block B – Electrode # 11. Blue: Monkey M – Block B – Electrode # 7.

	Pre-target	Early	Middle
Early	**3.4e-05** **<2e-16**	-	-
Middle	**0.00014** 0.615	0.689 **<2e-16**	-
Late	**6.3e-06** 0.064	0.733 **3.7e-8**	0.689 0.033

We performed a greedy electrode-adding procedure (section 2.3.8) by sequentially adding individual electrodes that provided the largest classification accuracy gain. The decoding accuracy and 95% confidence intervals for the increasing number of electrodes are presented in Figure 7B. We also plotted on this figure the absolute best decoding accuracy for all possible combinations of electrodes (dashed lines). As processing requirements increase exponentially for every additional electrode, we limited this analysis to combinations of up to 6 electrodes. We found that our greedy electrode-adding procedure produced comparable results to the best combinations, with a more manageable computation time, warranting its use as our gold standard.

Table 5. Pairwise Wilcoxon rank sum test P-values for the different target locations. Black: Monkey JL - Block B – Electrode # 11. Blue: Monkey M – Block B – Electrode # 7.

	T1	T2	T3	T4	T5	T6	T7
T2	0.013 **3.2e-5**	-	-	-	-	-	-
T3	**4.7e-5** **2.0e-6**	0.047 1.0	-	-	-	-	-
T4	**5.9e-4** 0.092	0.432 0.20	1.0 0.268	-	-	-	-
T5	1.0 0.138	0.021 **2.4e-9**	**4.9e-6** **3.4e-12**	**2.4e-4** **3.4e-5**	-	-	-
T6	1.0 0.041	0.432 **3.7e-11**	**0.0047** **2.7e-15**	0.025 **2.2e-6**	1.0 1.0	-	-
T7	1.0 **1.4e-6**	**3.8e-4** **<2e-16**	**1.2e-5** **<2e-16**	**2.0e-4** **6.3e-13**	1.0 0.10	1.0 0.19	-
T8	1.0 1.0	0.111 **2.5e-3**	**2.7e-4** **0.002**	**4.6e-3** 0.268	1.0 0.14	1.0 0.05	1.0 **2e-5**

Although these methods might be prone to overfitting and are not recommended for real-world decoding applications, our goal here was to evaluate the peak decoding accuracies achievable with our current data. We found that the peak decoding accuracy (Figure 7B, black asterisks) was reachable, within the 95% confidence intervals, for electrode groups containing at most 6 electrodes for monkey JL (Block A and B: 4, Block C: 6) and 7 for monkey M (Block A: 7, Block B: 6, Block C: 4). This suggests that a large proportion of electrodes are either non-informative or provide redundant information, further warranting spatial optimization. The location on the MEAs

of the top 6 electrodes for monkey JL and top 7 electrodes for Monkey M found with the greedy electrode-adding procedure are shown in Figure 7C.

The previous greedy electrode-adding procedure identified some locations on the MEAs which seemed more valuable in discriminating the different saccade target locations. Alternatively, some electrodes did not seem to provide valuable information. This led us to investigate the possibility

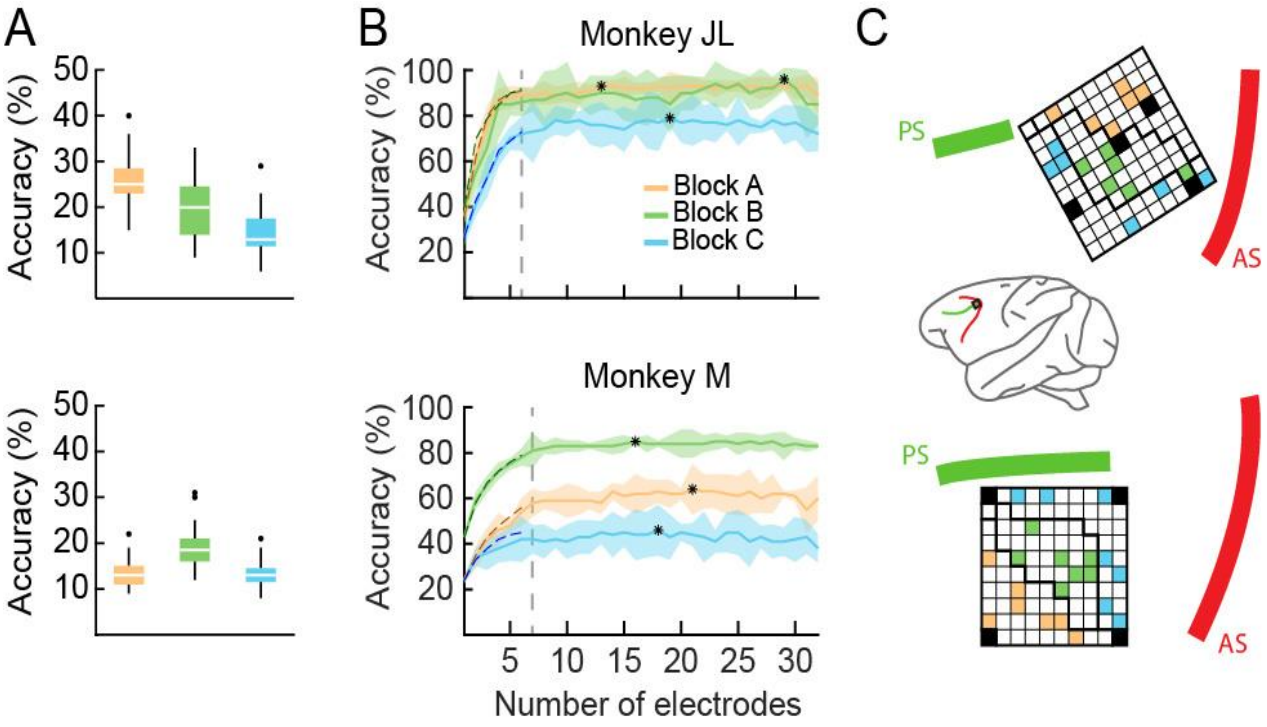

Figure 7. Analysis on spatial contribution of individual electrodes to the decoding accuracy of saccade intentions during the movement preparation period of the task (electrodes on blocks A, B, and C are in orange, green, and blue respectively). Part (A) represents individual decoding accuracy (mean and standard deviation) with chance levels for monkey JL as follows: A (16.6%), B (14.0%), C (12.3%) and for monkey M as follows: A (12.3%), B (14.5%) and C (12.3%). (B) shows the decoding accuracy for increasing electrodes based on features from continuous PSC #1 for an increasing number of channels. The top and bottom row show the results for all sessions on monkey JL and on monkey M respectively. The solid lines represent the mean of the decoding accuracy from the greedy electrode-adding procedure, the dashed line show the results from combining all electrodes up to 6 electrodes. The black stars highlight the maximum accuracy obtained for each session. The shaded area represents the mean ± confidence interval (CI) and the dashed vertical bar shows at which electrode all sessions reached the CI. (C) shows the location on the MEA of the top 6 (top row - monkey JL) or 7 (bottom row - monkey M) electrodes required to reach the CI interval.

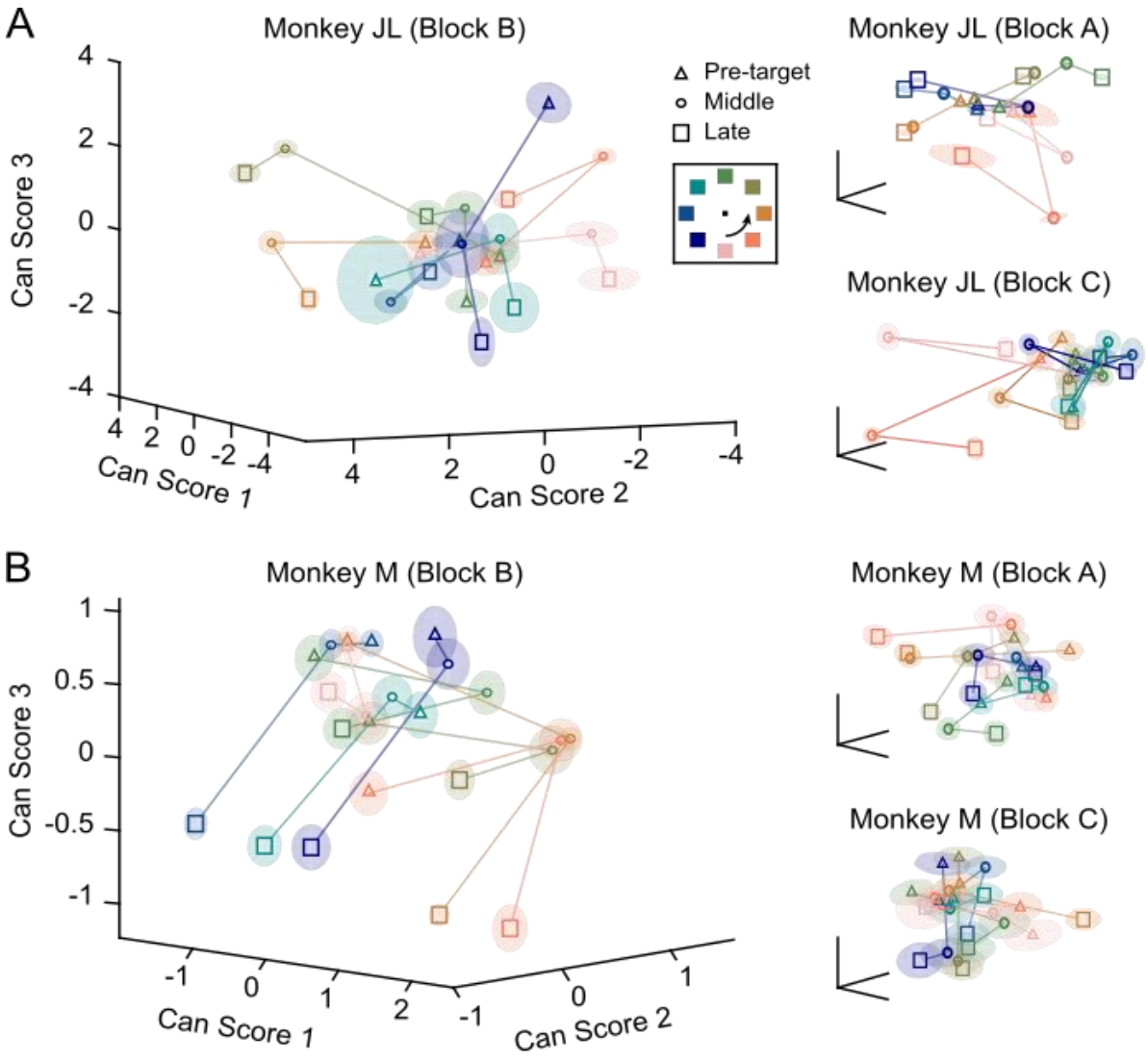

Figure 8. Dynamics of PSC #1 in Canonical Space and Spatial Visualization on MEAs. (A-B) show the dynamics of PSC #1 in canonical space for all saccade targets on both monkeys, for fixation epochs pre-target (Δ), early fixation period (O) and, late fixation just before the saccade (□).

of reducing the spatial dimension of 32 electrodes into a more optimized combination of electrodes that could maintain or improve the decoding performance. As detailed in section 2.3.9, we created a linear regression model using the broadband activity on all electrodes as the response variable, with the eight possible target locations, four different fixation epochs and their interactions, as the factors. Using this model, we focused on the epoch-target interaction term and performed a

canonical discriminant analysis (Friendly and Fox, 2020) to find the linear combination of electrodes that maximized its separability. The resulting canonical coefficients represent a transformation of the broadband activity from the space of all electrodes into a canonical space that maximizes the differences in these epoch-target interactions.

We plotted the per target mean of the multichannel PSC #1 projected on the top 3 canonical vectors for pre-target, early, and late fixation epochs (Figures 8A, 8B). The resulting figures show the dynamics of PSC #1, starting with a cluster for all targets during the pre-target fixation epoch and dispersing during the following epochs when the animal can see the intended saccade location. Monkey JL (Blocks A-B-C) and monkey M (Block B) show good separation for those sessions, corresponding with the higher decoding accuracy demonstrated in the previous section. On the other hand, sessions A and C of monkey M do not show good separation, coinciding with worse decoding performance.

2.4.3 Spatial visualization of broadband activity contribution

The coefficients of the most influential canonical vectors inform which electrodes are most valuable in discriminating the intended saccade target location during the delay period. These coefficients represent the weights allocated to each electrode's broadband activity to maximize the discriminability of the intended saccade targets throughout the movement preparation period of the task. In Figure 9A we represent the MEAs for monkey JL on the left and monkey M on the right with 10×10 arrays, each separated in 3 blocks of 32 electrodes (see Figure 4A for details). The top row shows the first canonical vector coefficients for each session (scaled and absolute) representing the electrode's weight in epoch-target discrimination. The bottom row illustrates the normalized SVM decoding accuracy of individual electrodes. The mean of the continuous PSC #1,

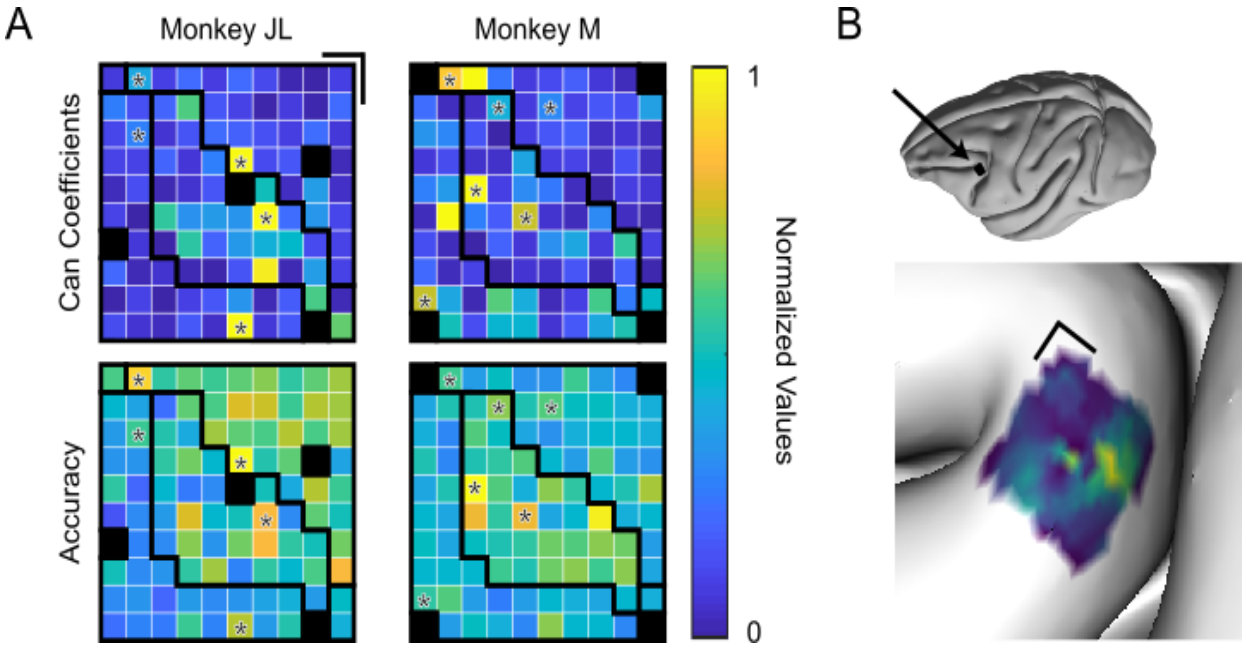

Figure 9. Spatial Visualization on MEAs. (A) shows Monkey JL and Monkey M electrode arrays based on the top canonical vector coefficients scaled and absolute (top row) and based on the individual electrode decoding accuracy (bottom row). The stars represent significant contributing electrodes which overlap between methods for each monkey. (B) Anatomical visualization of monkey JL MEA. The spatially interpolated broadband activity based on the top canonical vector coefficients are projected on a monkey cortex model (Seidlitz et al. 2018) using Neuralact Matlab toolbox (top row, Kubanek and Schalk 2017) and using Visbrain (bottom row, Combrisson et al. 2019).

over the 1600 ms movement preparation period of the trials (starting at target onset), was used for the SVM input features. The four black squares on the arrays represent the unused electrodes which are set by the manufacturer. The blocks A-B-C on each array are separated by a darker contour. Looking at the top and bottom rows, we can compare the locations of valuable electrodes for discriminating epoch-target interactions. The discriminating information for these epoch-target interactions visualized on the MEAs, for monkeys JL and M shown in column 1 and 2 respectively, are subjectively similar. We compared the locations of the 5 best electrodes from each block and marked the common pairs across the two conditions (Figure 9A, asterisks). As can be seen by the number of asterisks in each block, monkey M block C ("L" shaped block in lower left corner –

refer to Figure 4A) does not show much overlap. This observation coincides with an overall worse

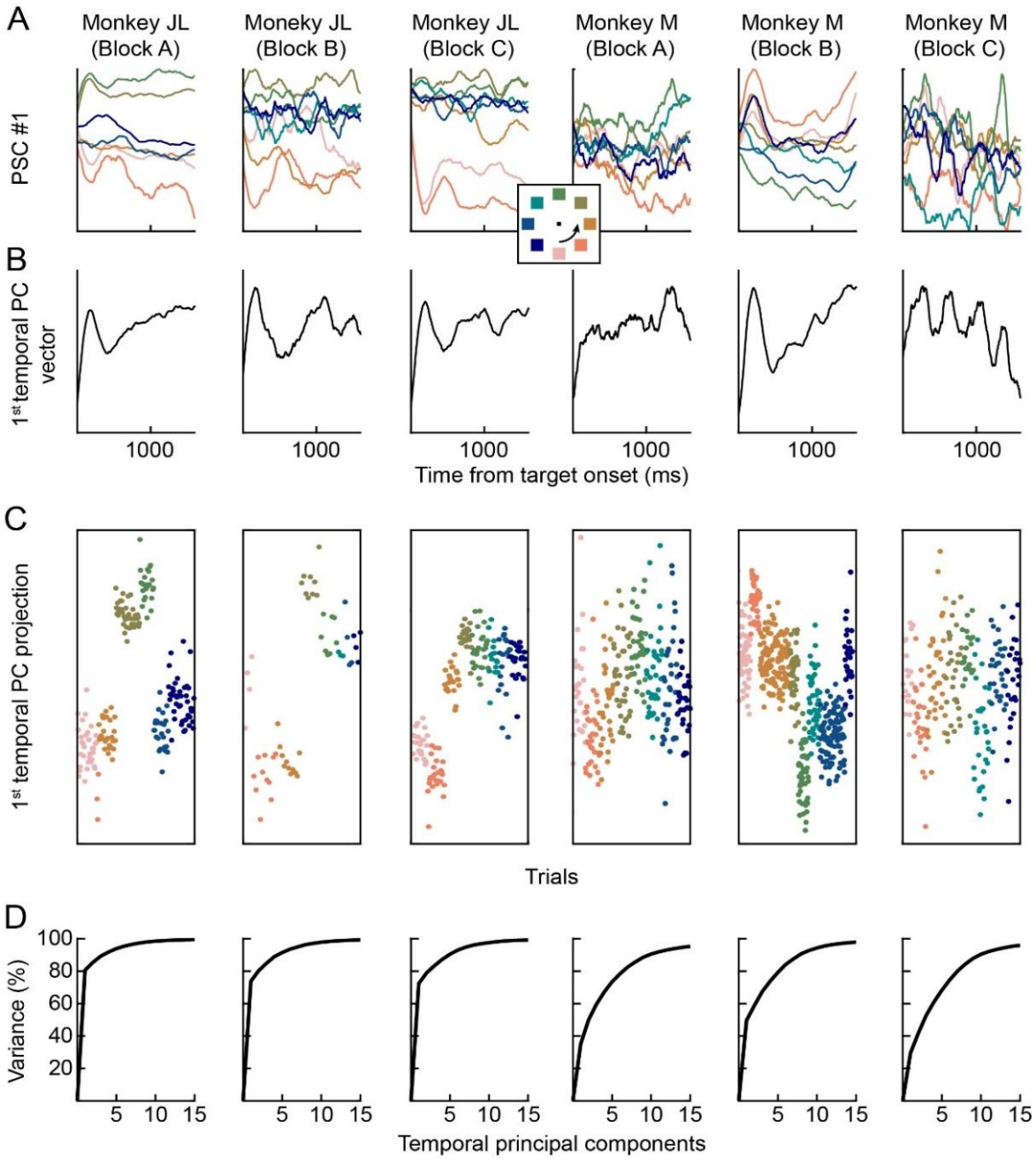

Figure 10. Continuous broadband activity related to saccade location intent. (A) Dynamics of PSC #1 projection on the top canonical vector, from target onset to saccade cue, averaged for trials of same target location, which is used as inputs for the temporal PCA analysis. (B) The coefficients of the first component resulting from the temporal PCA for all sessions. (C) The first component projection of temporal PCA performed on the PSC #1 projected on the top canonical vector, for all trials of each session grouped by saccade target locations**.** (D) The cumulative variance accounted for (VAF) of the temporal PCA components.

decoding performance for this session as shown with the greedy electrode-adding procedure, possibly due to the lesser involvement of the active electrodes during the saccade task. The fact that all electrodes do not overlap perfectly indicates that the canonical analysis efficiently discarded redundant information, while allocating higher weights to complementary electrodes, or to electrodes that are possibly informative about task epochs.

Table 6. Decoding accuracy of eight saccade target locations for all sessions (* except for monkey JL-Block A which had trials for seven possible target locations). Four different methods (red: associate chance level based on shuffling the target labels) are compared which all used SVM learning (5-fold cross-validation, averaged of 1000 iterations) with different features based on broadband activity (PSC #1).

	SVM Learning Features based on PSC #1			
Sessions	**M1**	**M2**	**M3**	**M4**
SVM Features size	#trials x 128	#trials x 7	#trials x 11	#trials x 32
MonkeyJL: Block A*	76.1 (16.2)	91.2 (16.4)	84.1 (16.5)	91.7 (16.6)
MonkeyJL: Block B	59.5 (10.6)	95.6 (13.9)	81.8 (14.3)	86.9 (14.0)
MonkeyJL: Block C	32.1 (12.1)	80.6 (12.3)	65.7 (12.3)	72.9 (12.3)
Monkey M: Block A	29.0 (12.5)	57.4 (12.2)	48.5 (12.2)	57.7 (12.3)
Monkey M: Block B	60.6 (14.8)	87.3 (14.4)	83.7 (14.5)	83.0 (14.5)
Monkey M: Block C	23.7 (12.5)	46.9 (12.3)	34.1 (12.4)	37.6 (12.3)

To highlight the relevant location within area 8A of the LPFC, Figure 9B shows the interpolated contribution of the electrode's related broadband activity based on the top canonical vector coefficients for monkey JL.

2.4.4 Temporal dimensionality reduction of continuous broadband LFP

The top canonical vectors, averaged for the different targets, represent the dynamics of the projected broadband activity during the entire 1600 ms of the movement preparation period (Figure

Table 7. Statistical differences ($p < 0.001$ is represented by ***) and Cohen's d effect size comparing distribution accuracies obtained between the decoding methods. Distributions are made of 1000 samples where each sample is the average of the SVM 5-fold CV accuracy results minus the associated method shuffled results.

	MonkeyJL: Block A				MonkeyJL: Block B				MonkeyJL: Block C			
	M1	M2	M3	M4	M1	M2	M3	M4	M1	M2	M3	M4
M2	9.54 ***	0	-	-	8.78 ***	0	-	-	22.52 ***	0	-	-
M3	4.90 ***	-9.69 ***	0	-	5.08 ***	-7.62 ***	0	-	14.45 ***	-10.74 ***	0	-
M4	8.99 ***	0.39 ***	7.49 ***	0	5.66 ***	-3.29 ***	1.82 ***	0	16.57 ***	-4.59 ***	4.09 ***	0
	Monkey M: Block A				Monkey M: Block B				Monkey M: Block C			
	M1	M2	M3	M4	M1	M2	M3	M4	M1	M2	M3	M4
M2	14.16 ***	0	-	-	21.90 ***	0	-	-	11.88 ***	0	-	-
M3	9.83 ***	-5.89 ***	0	-	18.29 ***	-6.70 ***	0	-	4.93 ***	-7.72 ***	0	-
M4	12.69 ***	0.12	4.94 ***	0	16.66 ***	-6.23 ***	-0.97 ***	0	6.26 ***	-4.88 ***	1.87 ***	0

10A). The coefficients of the top PCA component vector (Figure 10B), common to all targets, show a similar pattern across all JL blocks and monkey M block B; transient weighting of the initial target-onset response followed by a more gradual increase in weighting as response time approaches. The first principal component for all trials of each session, grouped by target locations, is represented in Figure 10C. This figure shows that the first temporal component associated with the top canonical vector has discriminating information regarding the saccade target location. Note that the figure only displays the contribution from one canonical vector. The discriminative capability improves as contributions from additional canonical vectors are included. For all sessions, we also plotted the cumulative variance accounted for (VAF) of the top 15 temporal PCA components which show that for monkey JL, more than 70% of the variance was captured with the top component while for monkey M, more components were required to capture the temporal variance (Figure 10D).

2.4.5 Decoding Saccade Target

The statistical analysis performed above is descriptive and demonstrates how lower dimensional projections of neural activity evolve over time in a task-dependent manner. However, in an iBCI setting, the interest often lies in efficiently decoding a single factor. It may therefore be better to consider individual, instead of mixed, models for the canonical transformation. These optimized vectors can be superior at discriminating classes within one categorical variable, while using a lower number of canonical vectors to support the required degrees of freedom. We investigated the benefits of using such specialized vectors to maximize differences between target locations and to better understand the relative trade-offs between dimensionality reduction and temporal integration window with decoding accuracy. To do so, we compared the accuracy obtained using SVM on different feature sets (see section 2.3.11 for details). The features for the first method (M1) are based on the PSC #1 averaged over the four separated 512 msec epochs. Methods two and three (M2-M3) uses the PSC #1 projection on the canonical vectors specialized to decode target locations (M2) or the epoch-target interactions (M3). For method four (M4), the features are generated with the mean of the continuous PSC #1 over the movement preparation window.

The reported results are the mean of repeating the 5-fold cross-validation SVM 1,000 times. For each method, we also report the chance level calculated by shuffling the target labels as described in section (2.3.7). The resulting decoding accuracies for all methods and all sessions including the input features' matrix sizes, are displayed numerically in Table 6, and plotted in Figure 11A. To compare methods, we performed a Wilcoxon rank sum test and calculated the Cohen's d effect size (Table 7).

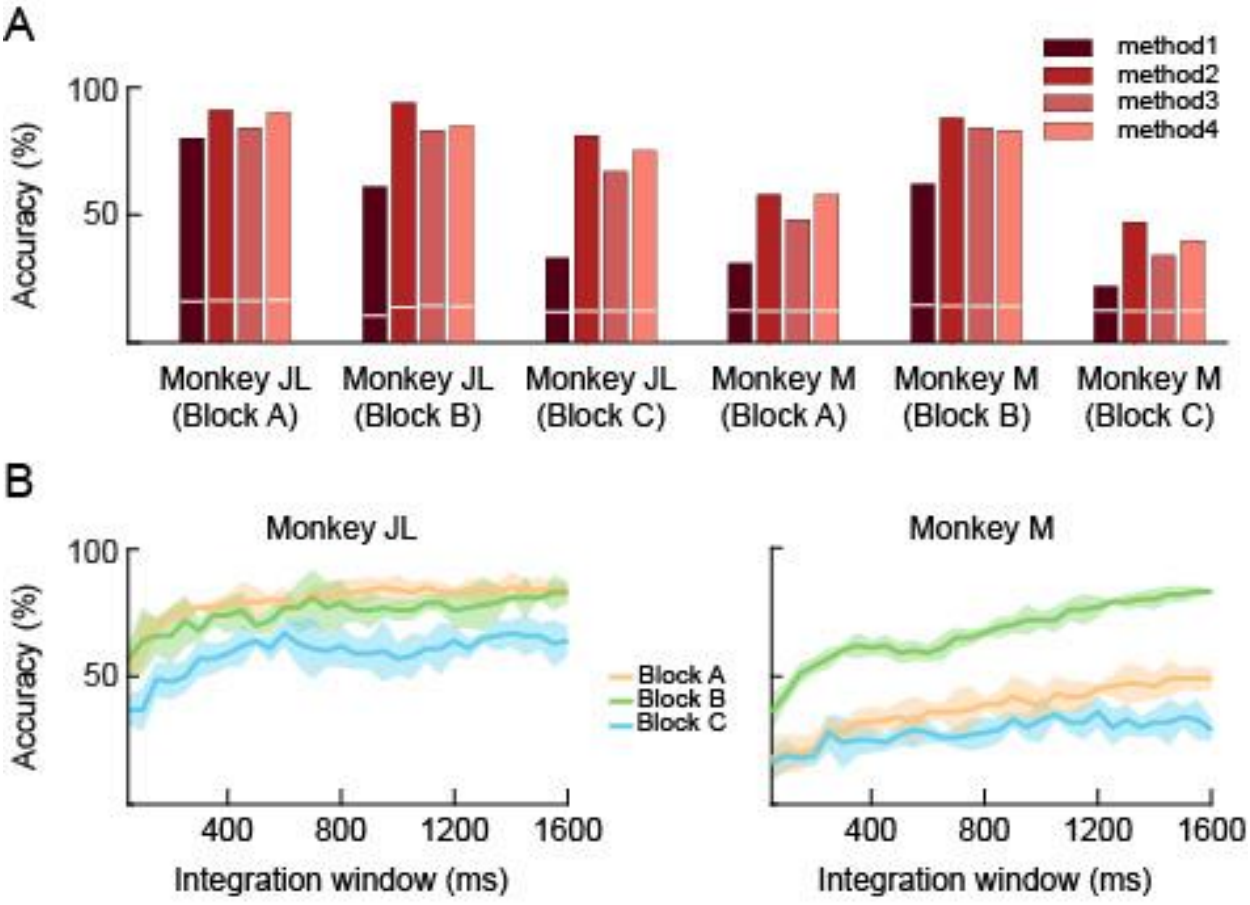

Figure 11. Decoding Accuracy and Speed of Convergence. (A) compares the decoding accuracy for all methods on each session, with the white separation showing the chance level associated with this method. (B) demonstrates the SVM decoding accuracy (mean and standard deviation) using continuous PSC #1 spatially and temporally reduced (method 3) for increasing window length (Δ of 50 ms).

The decoding accuracy for classifying all targets is significantly better using the continuous PSC #1 signal (M2, M3, M4), as opposed to using the activity found in a limited number of fixation epochs (M1). In addition, we found that the accuracy is slightly better using a canonical transformation that maximizes the target location factor, even with the input matrix size being significantly smaller than the other methods (63% and 22% smaller compared to M3 and M4 respectively).

2.4.6 Decoding performance over time

Because a cognitive iBCI would require short response times, we quantified how quickly the intended saccade target could be discriminated once its location was shown to the animals. The SVM classifier based on M3 was applied to the low spectral, spatial, and temporal dimensions of the LFP features to quantify classification as a function of temporal integration, with a time window ranging from 50 ms to 1600 ms. Figure 11B illustrates the speed of decoding convergence for all sessions on both monkeys. We demonstrated that for monkey JL, it was possible to decode the saccade target location close to maximum accuracy in less than 400 ms after the target onset, which is within the suggested BCI minimal requirement of 750 ms for sense of agency (Skomrock, et al. 2018). The results for monkey M showed a steady increase in performance throughout the fixation period.

2.4.7 Model validation

In the previous analyses, the decoding cross-validation was performed after the spectral, spatial, and temporal dimensionality reduction. To validate the entire process, we split the data from monkey M – Block B session into a 90% training and 10% testing data sets (randomly selected for each target). With the training set, we generated the spectral principal components, the canonical vectors for the epoch-target interactions, the temporal principal components, as well as the SVM model parameters. We evaluated the decoding accuracy of the pre-trained model on novel data and obtained an 86.7% decoding accuracy, which is within 2% of the training data set results (88.0%).

To validate the robustness of our model on monkey JL, we performed a similar experiment using the vectors and SVM model parameters trained on block B (training session 2) and applied them

to a different session (testing session 1), captured on the same block over one month apart. We performed this analysis using methods M2 and M3. We obtained a decoding accuracy within 16% of the performance from components trained on the same session (Table 8).

Table 8. Decoding accuracy for all target locations using saved dimensionality reduction components and model parameters from a training session recorded over a month apart (red: chance level calculated using a shuffle test).

Monkey JL – Block B			
Training Data Set	Testing Data Set	Decoding Accuracy (%) Saved components and SVM model parameters	
		M2	M3
Session 1	Session 1	**95.6** (13.9)	**81.8** (13.9)
Session 2	Session 2	**86.1** (12.2)	**78.5** (12.2)
Session 2	Session 1	**79.6** (14.0)	**68.5** (14.1)

The validation results would suggest the possibility of training a BCI system to identify spectral, spatial, and temporal components for certain significant variables or interactions, and then using this knowledge in future sessions without the need to continuously re-evaluate these dimensions and the model in real-time.

2.4.8 Proposed workflow

The methodology described in this manuscript is a sequence of processes through which neural signals can be preprocessed to optimize the classification of various factors of interest (e.g., intended saccade target) in an iBCI setting. The proposed workflow, represented by a flow chart in Figure 12, includes two parallel paths: preprocess and decoding. The preprocess path includes a statistical analysis to verify that (1) the LFPs are task modulated and (2) the relevant factors can

be discriminated from PSC #1. Once this is validated, the dimensionality reduction vectors as well as the classification model parameters will be generated and stored. The decoding path uses these stored variables to classify the factors which can then be passed on to the BCI decoder. While the BCI is in use, factors classification can be validated (i.e., performance is acceptable from the user's

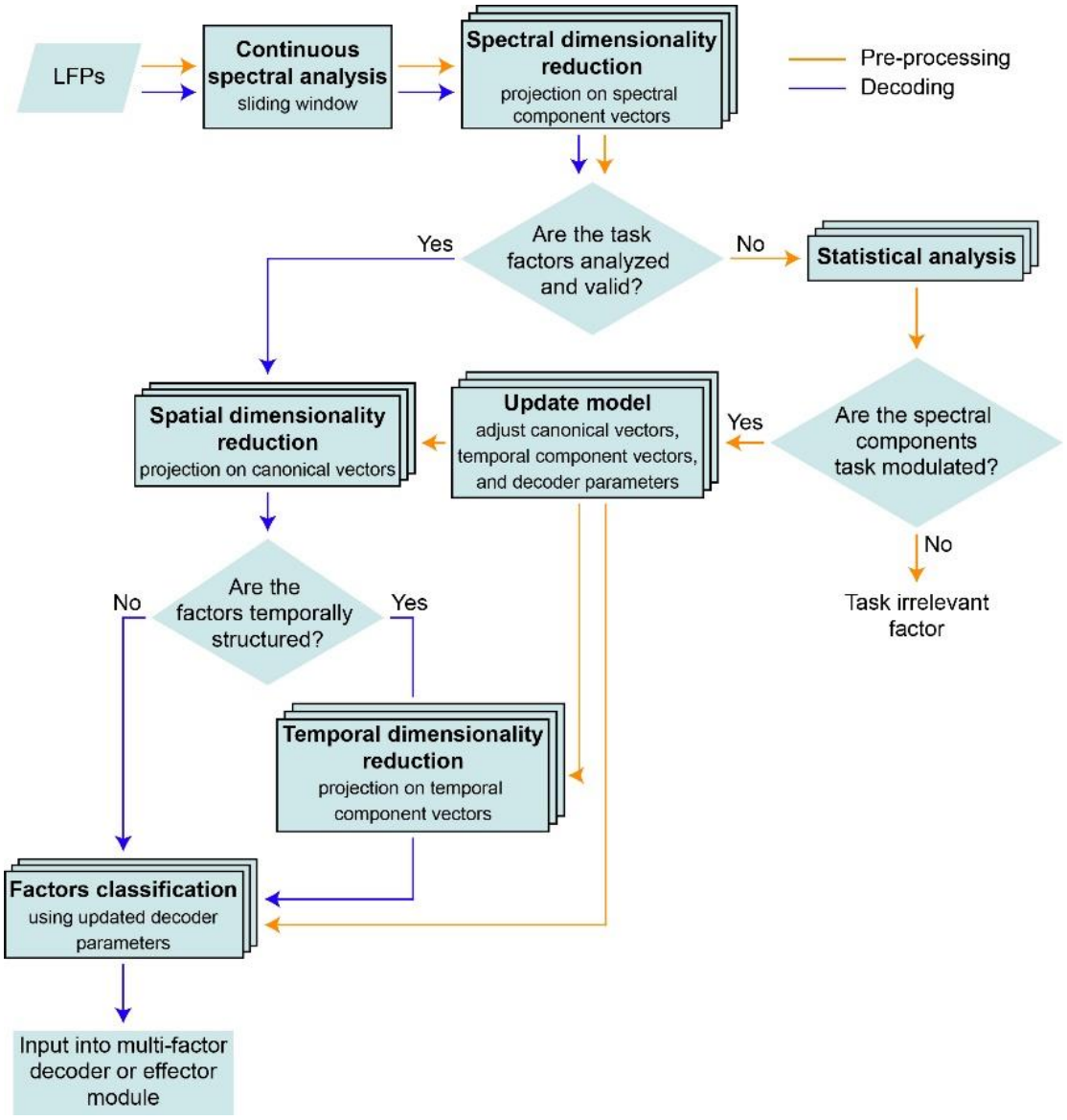

Figure 12. Proposed BCI workflow to decode task variables (factors like target locations) using spectral, spatial and temporal dimensionality revduction.

perspective or from a monitoring algorithm) and, if deemed unacceptable, the factors can be reprocessed, without affecting decoder response time.

2.5 Discussion

In this paper, the technique of reconstructing the power spectral density from different principal spectral components was applied to intracortical microelectrode LFP data. This technique has been utilized in the past on ECoG signals allowing the relation between low frequency oscillations and broadband amplitude to be established (Miller et al. 2009). The application of this analysis to multielectrode array data from macaque LPFC provides evidence suggesting that the broadband signal may be an effective surrogate of physiological activity across spatial scales. At the relatively small scale of microelectrode recordings, it may represent population spiking activity; at the larger scales represented by ECoG recordings, it may demonstrate phase dynamics over gyri and across sulci.

The decoding accuracy obtained from classifying all targets using broadband LFPs from LPFC, indicates that this activity can be a useful signal in a goal based BCI system. In at least one block of electrodes on both monkeys, we could identify all possible target locations correctly in over 85% of the test cases. Comparing our results with previous studies, we confirmed that LFPs offer comparable decoding performance to spiking data from LPFC (Boulay et al. 2016). In some sessions, decoding accuracy was suboptimal, possibly due to activity involved in other prefrontal processing unrelated to saccade planning or to other factors related with the signal and noise in the recordings. Even with similar placement of MEAs, inter-subject responses can vary greatly (Labecki et al. 2019), further strengthening the case for optimization along each step of the process. Our overall results suggest that sampling LFP signals from relatively small areas of the LPFC

provide sufficient information to decode movement goals, in the presence of saccade inhibition (delay) and in the presence of visual distractors (the task-unrelated cue). Since real-world iBCI's will need to incorporate movement inhibition and "visual clutter", LPFC may offer advantages over (or in addition to) motor cortex. An open question is whether the robustness of LPFC LFP decoding scales with the added task complexity required in real world applications, as well as how stable they remain over multiple months or years needed for a prosthetic implant to be viable. Because we likely recorded from supragranular layers (e.g., deep layer 3) of the LPFC and from the larger pyramidal cells in such layers, we hypothesize that we accessed high level integrated information about target goals. Whether the same information would be accessible to ECoGs remains to be investigated.

One aspect of our results is that we do not use a closed loop interface where the animal may be able to modulate the neural activity during training. It is likely possible the performance in this scenario improves with training. The LPFC is a brain region that has shown high levels of plasticity during tasks that require learning as well as an expanded capacity to integrate high level information relative to primary sensory and motor areas (Miller, 2000).

We propose a workflow that can identify the optimal signal candidates for a BCI that encode goals during a period of movement preparation and inhibition. The dimensionality reduction using a supervised method proved beneficial in identifying the spatial contribution of each electrode's LFP-based broadband activity for a chosen task variable, and the interaction between chosen variables. Since multiple studies have shown that LFPs from intracortical electrodes are stable over time (Milekovic et al. 2015, Wang et al. 2014), the training period of a BCI system could include learning (1) the spectral composition of the broadband signal, (2) the optimal electrode's weight

or the optimal subset of electrodes, and (3) the fixation dynamics, which can together maximize the decoding of motor planning activity. Using these stored parameters in real time could provide valuable processing optimization and even allow or improve the decoding accuracy of multiple goal-encoding variables.

2.6 Conclusion

In conclusion, we examined LFPs sampled from the LPFC of two macaques and used spectral, spatial, and temporal dimensionality reductions to decode with high accuracy the intended saccade target location. We proposed a decoding workflow which allowed the prediction of a saccade target during a fixation period. We validated the stability of our parameters over time using an additional session recorded one month apart. We focused on LFPs because they are more robust than spikes in a chronically implanted MEA. However, a future analysis should assess the combination of spikes, noise RMS and/or PSC #1. As well, a subsequent study should investigate the consistency of the results on a larger number of sessions as well as verify the methodology with other cognitive tasks.

2.7 Acknowledgments

Support from the neuroscience program at Ottawa Hospital Research Institute and from the University of Ottawa Brain and Mind Research Institute.

2.8 References

[1] Ajiboye AB, Willett FR, Young DR, Memberg WD, Murphy BA, Miller JP, et al. Restoration of reaching and grasping movements through brain-controlled muscle stimulation in a person with tetraplegia: a proof-of-concept demonstration. The Lancet [Internet]. 2017;389(10081):1821–30.

[2] Andersen RA, Aflalo T, Kellis S. From thought to action: The brain–machine interface in posterior parietal cortex. Proceedings of the National Academy of Sciences of the United States of America [Internet]. 2019;116(52):26274

[3] Anderson TW, Darling DA. Asymptotic theory of certain" goodness of fit" criteria based on stochastic processes. The annals of mathematical statistics. 1952 Jun 1:193-212.

[4] Barios JA, Ezquerro S, Bertomeu-Motos A, Nann M, Badesa FJ, Fernandez E, Soekadar SR, Garcia-Aracil N. Synchronization of slow cortical rhythms during motor imagery-based brain–machine interface control. International journal of neural systems. 2019 Jun 26;29(05):1850045.

[5] Boulay CB, Pieper F, Leavitt M, Martinez-Trujillo J, Sachs AJ. Single-trial decoding of intended eye movement goals from lateral prefrontal cortex neural ensembles. Journal of Neurophysiology. 2016;115(1):486–99.

[6] Brainard DH, Vision S. The psychophysics toolbox. Spatial vision. 1997 Jan 1;10(4):433-6.

[7] Bullock KR, Pieper F, Sachs AJ, Martinez-Trujillo JC. Visual and presaccadic activity in area 8Ar of the macaque monkey lateral prefrontal cortex. Journal of Neurophysiology. 2017;118(1):15–28.

[8] Burns A, Adeli H, Buford JA. Brain–computer interface after nervous system injury. The Neuroscientist. 2014 Dec;20(6):639-51.

[9] Chambers JM. Linear models, in Statistical Models, eds. J.M.Chambers and T. J. Hastie (Wadsworth & Brooks/Cole). 1992.

[10] Cohen J. The effect size index: d. Statistical power analysis for the behavioral sciences. Abingdon-on-Thames: Routledge Academic. 1988.

[11] Collinger JL, Wodlinger B, Downey JE, Wang W, Tyler-Kabara EC, Weber DJ, et al. High-performance neuroprosthetic control by an individual with tetraplegia. The Lancet [Internet]. 2013;381(9866):557–64.

[12] Combrisson E, Vallat R, O'Reilly C, Jas M, Pascarella A, Saive AL, et al. Visbrain: A multi-purpose GPU-accelerated open-source suite for multimodal brain data visualization. Frontiers in Neuroinformatics. 2019;13(March):1–14.

[13] Corsi MC, Chavez M, Schwartz D, Hugueville L, Khambhati AN, Bassett DS, De Vico Fallani F. Integrating EEG and MEG signals to improve motor imagery classification in brain–computer interface. International journal of neural systems. 2019 Feb 17;29(01):1850014.

[14] Dickey AS, Suminski A, Amit Y, Hatsopoulos NG. Single-unit stability using chronically implanted multielectrode arrays. Journal of Neurophysiology. 2009;102(2):1331–9.

[15] Fan JM, Nuyujukian P, Kao JC, Chestek CA, Ryu SI, Shenoy K V. Intention estimation in brain-machine interfaces. Journal of Neural Engineering. 2014;11(1).

[16] Fan RE, Chang KW, Hsieh CJ, Wang XR, Lin CJ. LIBLINEAR: A library for large linear classification. Journal of Machine Learning Research. 2008;9:1871–4.

[17] Flint RD, Lindberg EW, Jordan LR, Miller LE, Slutzky MW. Accurate Decoding of Reaching Movements from Field Potentials in the absence of Spikes. Journal of Neural Engineering. 2012;9(4):1–22.

[18] Friendly M, Fox J, Friendly MM. Visualizing generalized canonical discriminant and canonical correlation analysis. R Package ‘‘candisc’’, version: 0.6–5. 2013.

[19] Georgopoulos AP, Schwartz AB, Kettner RE. Neuronal population coding of movement direction. Science. 1986 Sep 26;233(4771):1416-9.

[20] Heldman DA, Moran DW. Local field potentials for BCI control. In: Handbook of Clinical Neurology. Elsevier B.V.; 2020. p. 279–88.

[21] Jolliffe IT. Principal component analysis. Technometrics. 2003 Aug 1;45(3):276.

[22] Kang X, Sarma S V., Santaniello S, Schieber M, Thakor N V. Task-Independent Cognitive State Transition Detection From Cortical Neurons During 3-D Reach-to-Grasp Movements. IEEE Transactions on Neural Systems and Rehabilitation Engineering. 2015;23(4):676–82.

[23] Kobak D, Brendel W, Constantinidis C, Feierstein CE, Kepecs A, Mainen ZF, et al. Demixed principal component analysis of neural population data. eLife. 2016;5(APRIL2016):1–36.

[24] Kubanek J, Schalk G, State NY. NeuralAct: A Tool to Visualize Electrocortical (ECoG) Activity on a Three-Dimensional Model of the Cortex. 2017;13:167–174.

[25] Labecki M, Nowicka MM, Suffczynski P. Temporal modulation of steady-state visual evoked potentials. International Journal of Neural Systems. 2019 Apr 26;29(03):1850050.

[26] Manning JR, Jacobs J, Fried I, Kahana MJ. Broadband shifts in local field potential power spectra are correlated with single-neuron spiking in humans. Journal of Neuroscience. 2009;29(43):13613–20.

[27] Markowitz DA, Wong YT, Gray CM, Pesaran B. Optimizing the decoding of movement goals from local field potentials in macaque cortex. Journal of Neuroscience. 2011 Dec 14;31(50):18412–22.

[28] Mendoza-Halliday D, Martinez-Trujillo JC. Neuronal population coding of perceived and memorized visual features in the lateral prefrontal cortex. Nature Communications [Internet]. 2017;8:1–13.

[29] Milekovic T, Truccolo W, Grün S, Riehle A, Brochier T. Local field potentials in primate motor cortex encode grasp kinetic parameters. NeuroImage [Internet]. 2015;114:338–55.

[30] Miller EK. The prefrontal cortex and cognitive control. InPerception. 2002 Jan 1;31:104.

[31] Miller EK, Erickson CA, Desimone R. Neural mechanisms of visual working memory in prefrontal cortex of the macaque. Journal of Neuroscience. 1996;16(16):5154–67.

[32] Miller EK, Cohen JD. An Integrative Theory of Prefrontal Cortex Function. Annual Review of Neuroscience. 2001;24:167–202.

[33] Miller KJ, Zanos S, Fetz EE, Den Nijs M, Ojemann JG. Decoupling the cortical power spectrum reveals real-time representation of individual finger movements in humans. Journal of Neuroscience. 2009;29(10):3132–7.

[34] Miller KJ, Honey CJ, Hermes D, Rao RPN, denNijs M, Ojemann JG. Broadband changes in the cortical surface potential track activation of functionally diverse neuronal populations. NeuroImage [Internet]. 2014;85:711–20.

[35] Ortiz-Rosario A, Adeli H. Brain-computer interface technologies: From signal to action. Reviews in the Neurosciences. 2013;24(5):537–52.

[36] Ortiz-Rosario A, Adeli H, Buford JA. Wavelet methodology to improve single unit isolation in primary motor cortex cells. Journal of neuroscience methods. 2015 May 15;246:106-18.

[37] Pandarinath C, Nuyujukian P, Blabe CH, Sorice BL, Saab J, Willett FR, et al. High performance communication by people with paralysis using an intracortical brain-computer interface. eLife [Internet]. 2017 Feb 21;6.

[38] Petrides M, Pandya DN. Dorsolateral prefrontal cortex: comparative cytoarchitectonic analysis in the human and the macaque brain and corticocortical connection patterns. European Journal of Neuroscience. 1999;11(6):1011–36.

[39] Petrides M. Lateral prefrontal cortex: Architectonic and functional organization. Philosophical Transactions of the Royal Society B: Biological Sciences. 2005;360(1456):781–95.

[40] Porat B. A course in digital signal processing. John Wiley & Sons, Inc.; 1996 Oct 1.

[41] Ramsay J O and Silverman W 1997 Canonical correlation and discriminant analysis, in Functional Data Analysis Springer Series in Statistics (Springer, New York).

[42] Rousche PJ, Normann RA. Chronic intracortical microstimulation (ICMS) of cat sensory cortex using the utah intracortical electrode array. IEEE Transactions on Rehabilitation Engineering. 1999;7(1):56–68.

[43] Santhanam G, Ryu SI, Yu BM, Afshar A, Shenoy K V. A high-performance brain-computer interface. Nature. 2006;442(7099):195–8.

[44] Seidlitz J, Sponheim C, Glen D, Ye FQ, Saleem KS, Leopold DA, et al. A population MRI brain template and analysis tools for the macaque. NeuroImage [Internet]. 2018;170(April 2017):121–31.

[45] Shenoy KV, Sahani M, Churchland MM. Cortical control of arm movements: A dynamical systems perspective. Annual Review of Neuroscience. 2013;36:337–59.

[46] Skomrock ND, Schwemmer MA, Ting JE, Trivedi HR, Sharma G, Bockbrader MA, et al. A Characterization of Brain-Computer Interface Performance Trade-Offs Using Support

Vector Machines and Deep Neural Networks to Decode Movement Intent. Frontiers in Neuroscience. 2018;12(October).

[47] Sumsky SL, Schieber MH, Thakor N V., Sarma S V., Santaniello S. Decoding kinematics using task-independent movement-phase-specific encoding models. IEEE Transactions on Neural Systems and Rehabilitation Engineering. 2017;25(11):2122–32.

[48] Tremblay S, Doucet G, Pieper F, Sachs A, Martinez-Trujillo J. Single-trial decoding of visual attention from local field potentials in the primate lateral prefrontal cortex is frequency-dependent. Journal of Neuroscience. 2015;35(24):9038–49.

[49] Tremblay S, Pieper F, Sachs A, Martinez-Trujillo J. Attentional Filtering of Visual Information by Neuronal Ensembles in the Primate Lateral Prefrontal Cortex. Neuron. 2015;85(1):202–15.

[50] Wang D, Zhang Q, Li Y, Wang Y, Zhu J, Zhang S, et al. Corrigendum: Long-term decoding stability of local field potentials from silicon arrays in primate motor cortex during a 2D center out task. Journal of Neural Engineering. 2014;11(4).

[51] Wilcoxon F. Individual comparisons by ranking methods. Biometr. Bull.1945;1:196-202.

[52] Wilkinson N and Rogers CE. Symbolic description of factorial models for analysis of variance Appl. Statist.1973;22:392-399.

[53] Willett FR, Avansino DT, Hochberg LR, Henderson JM, Shenoy KV. High-performance brain-to-text communication via handwriting. Nature. 2021 May 13;593(7858):249-54.

[54] Zhuang J, Truccolo W, Vargas-Irwin C, Donoghue JP. Decoding 3-D reach and grasp kinematics from high-frequency local field potentials in primate primary motor cortex. IEEE Transactions on Biomedical Engineering. 2010;57(7):1774–84.

Chapter 3

Decoding spatial locations from primate lateral prefrontal cortex neural activity during virtual navigation

3.1 Abstract

Objective. Decoding the intended trajectories from brain signals using a brain-computer interface system could be used to improve the mobility of patients with disabilities. *Approach*. Neuronal activity associated with spatial locations was examined while macaques performed a navigation task within a virtual environment. *Main results.* Here, we provide proof of principle that multi-unit spiking activity recorded from the lateral prefrontal cortex of non-human primates can be used to predict the location of a subject in a virtual maze during a navigation task. The spatial positions within the maze that require a choice or are associated with relevant task events can be better predicted than the locations where no relevant events occur. Importantly, within a task epoch of a single trial, multiple locations along the maze can be independently identified using a support vector machine model. *Significance*. Considering that the lateral prefrontal cortex of macaques and humans share similar properties, our results suggest that this area could be a valuable implant location for an intracortical brain computer interface system used for spatial navigation in patients with disabilities.

3.2 Introduction

Invasive brain-computer interface (iBCI) systems have the potential to improve quality of life for physically disabled individuals. The real-time use of intracortical activity can add communication channels (Santhanam et al. 2006, Pandarinath et al. 2017) or control assistive devices (Flint et al.

2012, Ajiboye et al. 2017). One potential application of a brain computer interface (BCI) is to aid individuals with limited mobility to navigate environments. As reported by Al-qaysi et al. (2018), the current advancement in technology allows intelligent wheelchairs to be safely controlled by brain signals, making it one of the important applications of BCI-based systems that can help disabled individuals gain independence. One issue that remains poorly investigated is the brain areas that can provide reliable signals for spatial navigation via a BCI.

The prefrontal cortex is known to coordinate cognitive processes such as working memory (Miller et al. 2018) and learning abstract rules (Wallis et al. 2001, Buschman et al. 2012). Studies have shown the impact of prefrontal cortex lesions on the successful execution of spatial working memory functions (Curtis and D'Esposito, 2003) and that the firing rate of the lateral prefrontal cortex (LPFC) cells is modulated by spatial working memory task demands (Jung et al. 1998, Corrigan et al. 2021). More specifically, neurons in the LPFC have been found to encode remembered spatial locations during working-memory (Mendoza-Halliday and Martinez-Trujillo 2017, Leavitt et al. 2017) and visuospatial attention (Tremblay et al. 2015, Backen et al. 2018) tasks, as well as movement intentions (Markowitz et al. 2011, Boulay et al. 2016, Johnston et al. 2021). Within the LPFC, neurons encode the location of items in virtual environments (Roussy et al. 2021) when monkeys navigate towards visible or invisible targets using a joystick. The use of such desktop systems provides an efficient platform to analyze the neuronal activity underlying path-integration (excluding proprioceptive information) during spatial navigation tasks (May and Klatzky 2000, Gulli et al. 2020). The geometry and intersections of a maze virtual environment, including boundaries (Lee 2017) and landmarks (Jansen-Osmann 2002), are key elements of spatial mapping and navigation behavior. Historically, motor execution tasks allowed the research

community to create primary and supplementary motor cortex functional maps. Further research demonstrated that motor imagery and motor attempt can generate valuable brain activity for the discrimination of movement intention (Chen et al. 2021), particularly applicable to BCI systems. We can use a similar approach for spatial navigation, by starting with the question of how spatial locations can be decoded while navigating a virtual maze using a joystick. The results can then guide us to further test imagined or attempted navigation.

Here, we demonstrate that spatial locations and task relevant events can be decoded from multichannel LPFC activity of rhesus macaques navigating through a virtual environment using a joystick. Using support vector machine (SVM) learning, we found that spatial location identification is more precise for locations associated with task relevant information such as maze intersections and directional change. We also demonstrated that different maze locations for the same task event could be differentiated (i.e., two different starting locations). Since spatial location probability depends on the prior position, we added a Markov chain to the SVM model prediction and found that it improves the decoder performance. We also show the possibility to optimize the size of the feature set by projecting the multi-unit spiking rate on canonical vectors generated to maximize the difference between spatial locations on the maze. The outcome of this study highlights the possibility of using the prefrontal cortex as a source of information related to task-relevant locations in a goal-selective cognitive iBCI system.

3.3 Methods

3.3.1 Animals

Two male rhesus macaques (*Macaca mulatta*), aged 10 and 9 years old with respective weights of 12kg and 10 kg, were trained to navigate through a maze with a joystick to complete an associative memory task (Figure 13A). For this task, the primates were trained to associate a context with a disk color. The goal was to reach the correct colored disk depending on the wall texture observed in the corridor of the maze (Figure 13B). If successful, the monkeys would receive a juice reward.

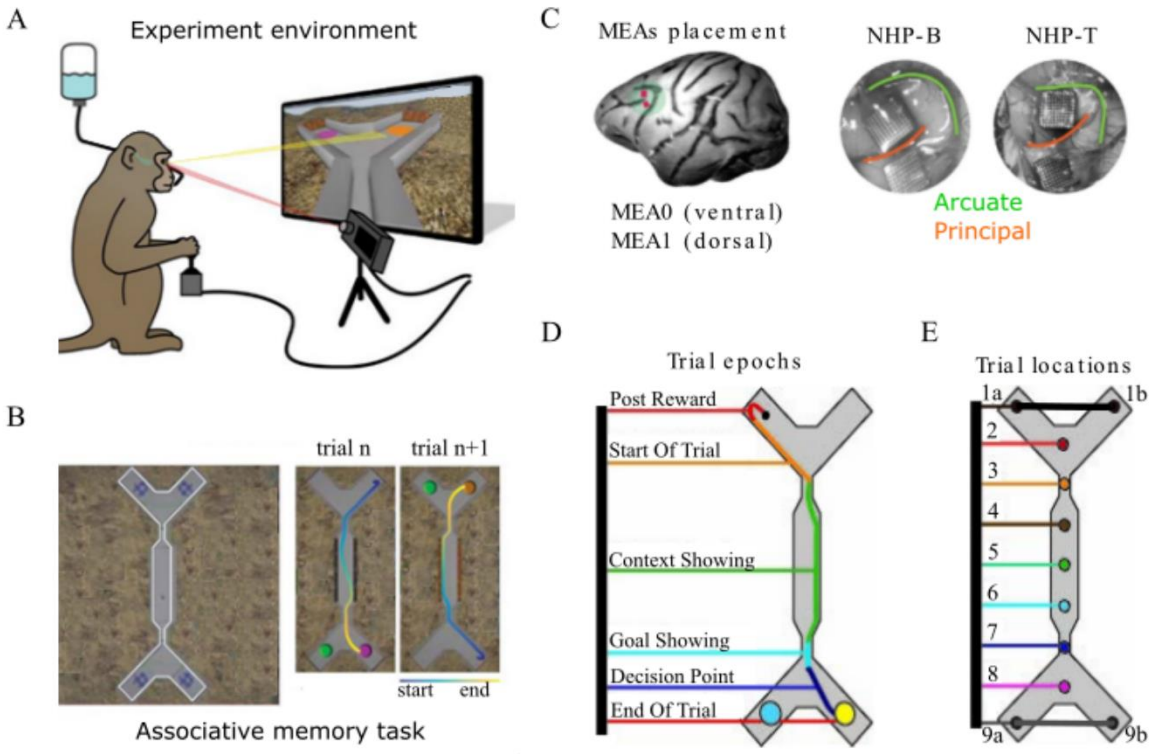

Figure 13. Experiment description and intracortical implant locations details. (A) Virtual desktop environment allowed the monkey to navigate through the maze using a joystick. Eye movements were tracked (Gulli et al. 2020). (B) One trial of the associative memory task would start at one end of the maze and move to the other end of the maze while the monkey learned to associate the correct wall context texture in the corridor of the maze with the correct disk color to obtain a reward. The next trial would start when the animal reached the disk and start its rotation back to face the maze center (Gulli et al. 2020). (C) MEAs were chronically implanted anterior to the arcuate sulcus in the LPFC of NHP-B and NHP-T, MEA0 and MEA1 located lateral and medial to the principal sulcus (Roussy et al. 2021). (D) Schematic of the maze showing trial epochs. (E) Schematic of the maze showing trial locations considered.

3.3.2 Electrophysiological recordings

The brain activity from the LPFC was recorded using two Utah microelectrode arrays (96 channels, electrode length of 1.5 mm). They were both implanted anterior to the arcuate sulcus, the first (MEA0) and second (MEA1) array being placed lateral and medial to the principal sulcus respectively (Figure 13C). The neuronal signals were recorded using a 128-channel Cerebus Neuronal Signal Processor from Blackrock Microsystems. The Plexon offline sorter was used to isolate the single units from the multi-unit stream. The local field potential (LFP) signal was band-pass filtered (0.3 Hz to 7.5 kHz) and digitized (16-bit with 1 μV per bit) at 30 kHz. Using a fourth-order Butterworth anti-aliasing filter with a 250 Hz cut-off frequency, the signal was finally down sampled to 1 kHz and re-reference to the common average.

3.3.3 Experimental Setup

The behavioral task took place in an X maze virtual environment (Doucet et al. 2016). During a session, the rhesus macaques were seated in a custom-built chair facing a computer monitor, the animals' head being fixed to allow eye position recordings which were not used in our study. They would freely navigate the maze using a two-axis joystick. The position within the maze was recorded at a rate of 75 Hz, matching the monitor refresh rate.

3.3.4 Behavioral Task

The task required associating a context (wall texture options: wood or steel) with a correct destination (disk options: color1 or color2). A session would include multiple blocks (3 or 4), each block had a different set of association (context-color) to be learned. Note that the first and last

blocks would use the same association set. The animals would receive a juice reward only if the correct association was made.

A trial starts once the monkey has completed the previous trial (Figure 13D), rotating its point of view to face the center of the maze ("post reward" task epoch). The animal then navigates from the left or right branch at one end of the X maze to the branch junction ("start of trial" task epoch). The monkey continues through a long corridor in which the side walls' texture represents the trial context ("context showing" task epoch). At the end of the corridor, the colored disks are visible ("goal showing" task epoch). The monkey then travels through the left or right end branch, depending on learned context-color association ("end of trial" task epoch). The next trial starts once the monkey reaches a colored disk. The context and the disk-color branch location were randomized independently for each trial. Equally spaced maze locations along the Nort-South axis were selected (Figure 13E).

Neural activity associated with task events and spatial locations is independent of the successful completion of the task. For this reason, we considered all trials regardless of the successful association of the context with a color. We only excluded incomplete trials where the animals did not navigate through all task locations. There was no time limit for a trial, the macaques would typically traverse the maze at the same speed, from the start to the end of each trial. The incomplete trials would be caused by the experimenter interrupting the experiment (i.e., when sufficient trials had been captured). Learning and unlearning activity was present during the trials but not considered in the analysis of spatial locations along the maze and the epochs of the task.

A session included the same navigational requirement but from trials belonging to different color-context associative tasks. We processed one session for each monkey. For non-human primate

Buzz (NHP-B), the session included 3 blocks run in the following order: block1 (66 trials), block2 (288 trials), and block3 (68 trials). For non-human primate Theo (NHP-T), the session included 4 blocks sequentially presented as follow: block1 (40 trials), block2 (97 trials), block3 (319 trials), and block4 (61 trials). Note that block1 and block3 for NHP-B, as well as block1 and block4 for NHP-T, used the same color-context association.

3.3.5 Neural data analysis

MATLAB and RStudio were used for all data analysis.

3.3.5.1 First principal spectral component

As reported by Miller et al. (2014), this signal represents the overall broadband frequency activity for a window centered at a particular time. For each 1024 msec window of interest, a principal component analysis was performed on the normalized power spectrum of the LFP to obtain the eigenvectors and eigenvalues. The first principal spectral component refers to the original spectrum projected on the principal eigenvector. For a more detailed description refer to Miller et al. (2009).

3.3.5.2 Support vector machine classification

To identify the spatial locations and epochs from the single and multi-unit spiking rate or from the first principal spectral component of the LFP, we used a support vector machine algorithm with a linear kernel (LIBLINEAR implementation for MATLAB (Fan et al. 2008), with options L2-regularized, L2-loss, and 5-fold cross-validation). We chose this algorithm as it is fast and is less vulnerable to overfitting. To classify multiple classes, this algorithm uses the one-vs-rest strategy.

3.3.5.3 Markov chain

The probability to be at a specific location in a maze depends on the prior location. For that reason, we added a stochastic model to our decoder. We designed a simple Markov chain which assigned probabilities for all possible locations given a prior location. Our predicted location is then based on the multiplication of the Markov chain probabilities with the SVM prediction probabilities.

3.3.5.4 Canonical discriminant analysis

To reduce the size of the SVM feature set used to decode the spatial locations, we generated 8 canonical vectors for each microelectrode array that maximize the neuronal activity difference between the 9 locations. In RStudio, we first fitted a linear model using the function "*lm*" from the R Stats package (Chambers 1992, Wilkinson and Rogers 1973) and then performed a canonical discriminant analysis (Ramsay and Silverman 1997) using the "*candisc*" function from the R candisc package (Friendly and Fox 2020) to create the canonical vectors. See Johnston et al. (2021) for further implementation details.

3.3.6 Statistics

The statistical significance of SVM feature set distributions was evaluated using the MATLAB implementation of the Wilcoxon rank sum test (Wilcoxon 1945). Each entry in our distributions was the average decoding accuracy of the 5-fold SVM result, which was repeated 100 times to create a full distribution for this feature set. A null distribution was similarly calculated using the average accuracy of the 5-fold SVM results after shuffling the classifier labels. Before performing the Wilcoxon rank sum test between our feature sets, the average of the null distribution was

subtracted from the decoding accuracy distribution. The statistically significant threshold was reported when the resulting p-value from the Wilcoxon test was less than 0.01.

3.4 Results

3.4.1 Spatial locations within a virtual environment can be decoded from the LPFC neural activity.

To explore whether a subject's position can be decoded from neuronal activity in the LPFC we trained two macaque monkeys to perform a navigation task in a virtual environment and recorded the responses of neurons in the LPFC using chronically implanted microelectrode arrays. A virtual maze (X-maze) was originally created using a gaming engine (Gulli et al. 2020, Corrigan et al. 2021). A trial *n* consists of a rhesus macaque navigating through the maze using a joystick going from one of two branches on one side at the start of the trial (SOT), to one of two possible branches on the opposite side at the end of the trial (EOT) (Figure 13A). The maze had a corridor that connected the two sets of branches. The animal had to learn the association between the wall texture (wood or steel) presented when entering the corridor (context epoch) and the colors of two disks that appear when the animals reached the branching point (e.g., wood context means choose the red disk and steel context means choose the green disk). At the end of the trial, the monkey receives a juice reward if the correct colored disk was reached. The next trial ($n + 1$) would start once the monkey had turned around in the maze (Figure 13B).

The brain activity of each monkey was recorded from two 10x10 microelectrode arrays (Maynard et al. 1997, Normann et al. 1999) located in the LPFC anterior to the knee of the arcuate sulcus. MEA0 and MEA1 are the array designations lateral and medial to the principal sulcus respectively

(Figure 13C). For the session with NHP-B, the electrophysiological recording from the first array (MEA0) provided valid signals from 96 electrodes (97 single-units, 96 multi-units), while the

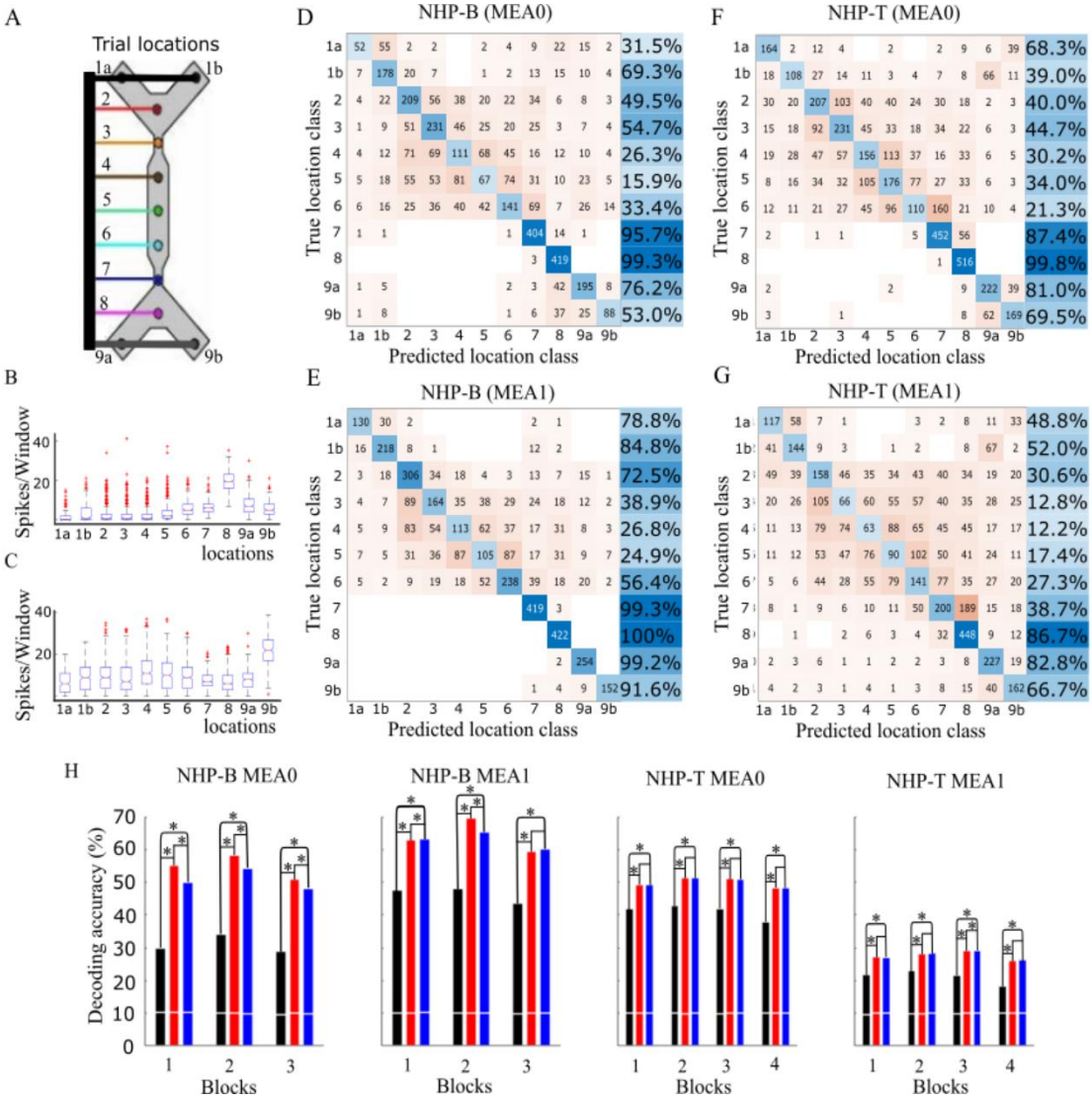

Figure 14. SVM decoding of 11 locations from PFC neuronal activity. (A) Schematic of the maze showing the location points considered in our decoding. (B)-(C) Single unit examples showing the number of spikes per 1024 msec window statistical distribution centered at each location (NHP-B, 422 trials). (D)-(E) Confusion matrices showing true and predicted classes of decoding the locations using multi-unit spiking activity from 422 trials (all blocks) with NHP-B MEA0 and MEA1 respectively. The diagonal values represent the number of trials where the prediction was successful (darker blue shows higher percentage of successful trials for each class). (F)-(G) Confusion matrices showing location decoding from 517 trials (all blocks) with NHP-T MEA0 and MEA1 respectively. (H) Overall decoding accuracy of locations obtained using the 1st principal spectral component of the LFP signal (black), single-unit (red) and multi-unit (blue) spiking activity from a 1024 msec window. White horizontal lines show the respective shuffled result ($p<0.001$ is represented by *).

second array (MEA1) gave 95 channels (132 single-units and 95 multi-units). For the session with NHP-T, the electrophysiological recording from MEA0 provided valid signals from 91 electrodes (90 single-units and 91 multi-units), while MEA1 gave 96 channels (49 single-units and 96 multi-units).

For each trial, 5 task epochs (Figure 13D) and 11 maze positions (Figure 13E) were defined on the North-South axis from where the animal started his navigation to where the animal stopped moving forward at the end of the trial. Note that the trials for location 1 and 9 are split between the right branch (locations 1a/9a) or left branch (locations 1b/9b) depending on the specific trial (Figure 14A).

We first examined if spatial locations within the maze could be decoded from the brain signals. We looked at single unit spiking activity around each maze location (1024 msec window) and found some single units which had higher number of spikes around specific locations. Figures 14B and 14C show examples of a single unit tuned to location 8 and location 9b respectively.

We then used 5-fold cross-validation support vector machine (SVM) repeated 100 times to evaluate the average decoding accuracy of 11 spatial locations from features based on a 1024 msec window of single-units and multi-units spiking rates as well as the first principal spectral component of the LFP (Miller et al. 2009) at those places. In a real-time BCI application, avoiding spike sorting is beneficial because it is time consuming. We therefore compared the average decoding accuracy obtained with the different features on individual blocks for both animals (Figure 14H). The tested feature sets on individual blocks for both arrays were all significantly higher than predicted by chance, however, the LFP-based decoder performed worse than that of the spiking activity. For most blocks, single units provided better results than multi-units.

Nevertheless, the remaining analysis and presented results will focus on multi-unit activity because of the broader applicability for a future iBCI.

The confusion matrices in Figure 14 show the results of the predicted versus true decoded classes of each location using data from all blocks for NHP-B on MEA0 (Figure 14D), MEA1 (Figure 14E), and for NHP-T on MEA0 (Figure 14F) and MEA1 (Figure 14G). The results highlight the fact that some locations are associated with unique neural activity, while others are associated with activity that resembles other locations. Similarity of activity is often seen in the long corridor of the maze (locations 4-6). Locations associated with the start of trial up to entering the corridor (locations 1-3) and from the goal showing to end of trial (locations 7-9) are better decoded. Importantly, the initial starting branch during the SOT epoch (locations 1a/1b) and the ending branch during EOT epoch (locations 9a/9b) could be particularly well identified on NHP-B MEA1 (start right: 78.8%, start left: 84.8%, end right: 99.2%, end left: 91.6%). These findings eliminate the possibility that the locations were decoded from neuronal activity linked with the time to reward or linked with the task epoch of the trials.

For subsequent analyses, we balanced the dataset by comparing the activity at 9 locations (instead of 11) on the North-South axis, combining the initial and final left/right branches into single locations (Figure 15C). The results of this analysis reinforced that location can be decoded well from the neural activity. Using the data from all blocks and both arrays, the decoding accuracies for positions 1,7,8,9 (the starting point and the end of the corridor to the final point of the trial), are all above 81% for NHP-B (the last 3 locations being decoded accurately for 1261 out of 1266 trials) and above 75% for NHP-T (Figures 15A-15B). To highlight the impact of array placement

on the decoding accuracy results, we looked at the predicted and true location class from all blocks on primates NHP-B (MEA0: Figure 15D, MEA1: Figure 15E) and NHP-T (MEA0: Figure 15F,

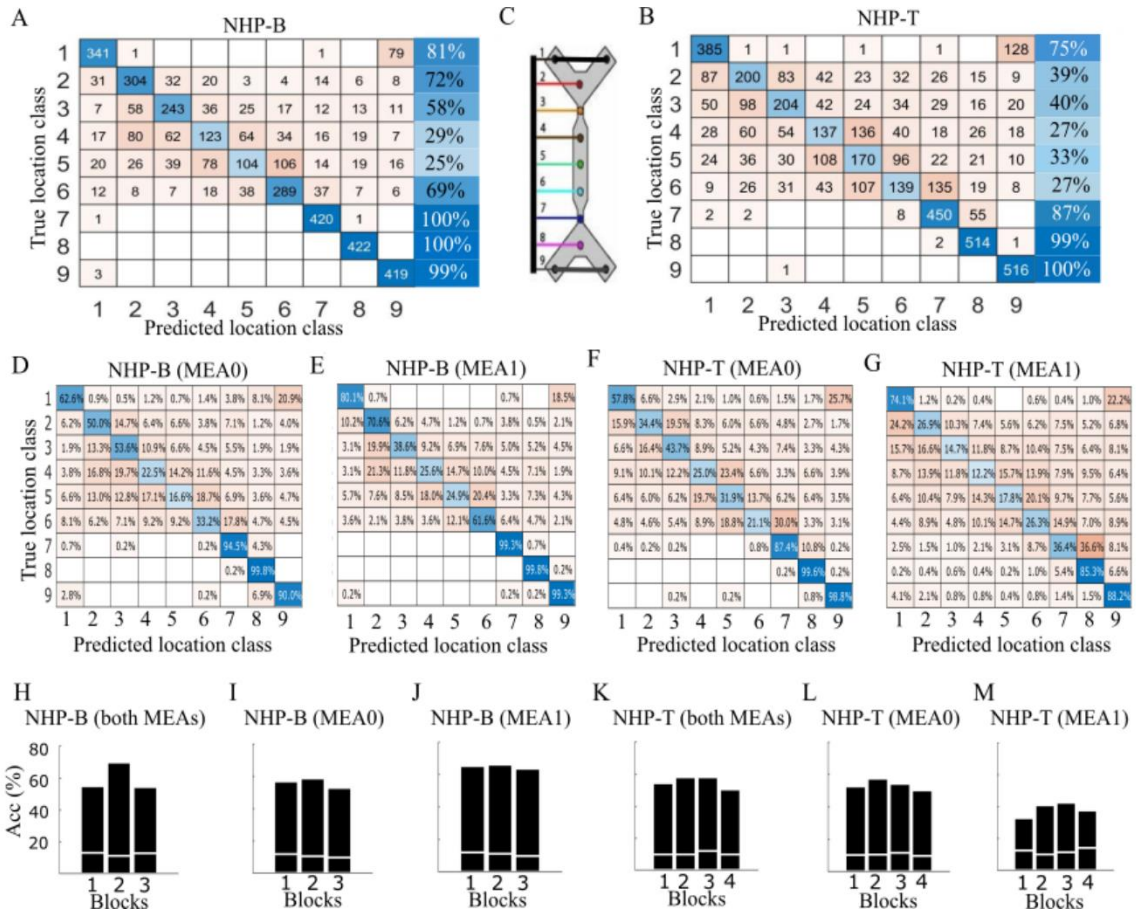

Figure 15 SVM Decoding of 9 locations from individual and combined blocks, using single or both arrays. (A) Confusion matrix showing true and predicted classes of decoding the 9 locations from 422 trials (all blocks) using both arrays on NHP-B. Right blue column show decoded accuracy for each class. Overall decoding accuracy obtained was 70%. (B) Confusion matrix showing true and predicted classes of decoding the 9 locations from 517 trials (all blocks) using both arrays on NHP-T. Right blue column show decoded accuracy for each class. Overall decoding accuracy obtained was 59%. (C) Schematic of the maze showing the location points considered for this analysis. (D)-(E) Confusion matrices showing predicted and true location decoding accuracy from 422 trials (all blocks) on NHP-B MEA0 and MEA1 respectively. (F)-(G) Confusion matrices showing predicted and true location decoding accuracy from 517 trials (all blocks) on NHP-T MEA0 and MEA1 respectively. (H) SVM decoding accuracy for individual blocks using both arrays for NHP-B. The horizontal white lines show the accuracy when labels were shuffled. (I)-(J) SVM decoding for individual blocks on NHP-B MEA0 and MEA1 respectively. (K) SVM decoding accuracy for individual blocks using both arrays for NHP-T. (L)-(M) SVM decoding for individual blocks on NHP-T MEA0 and MEA1 respectively.

MEA1: Figure 15G). Different levels of decoding accuracy were obtained with individual arrays, but all arrays could best discriminate locations 1-7-8-9. The decoding accuracies of locations from the combined blocks and arrays (Figures 15A-15B) are mainly the combination of the best decoding accuracies obtained from individual arrays.

We calculated the overall decoding accuracy by (1) performing a 5-fold cross-validation SVM analysis, (2) averaging the returned 5-fold accuracies and then (3) repeating this process 100 times to obtain a distribution of results, reporting its mean as the accuracy. The standard deviations of the obtained accuracy distributions for all blocks were smaller than 1.5%. The overall decoding accuracy using data from individual and combined arrays are significantly above the shuffled results for all individual blocks (Figures 15H-15M). We evaluated the above chance accuracy distributions by subtracting each entry with the averaged shuffled accuracy. The Wilcoxon rank sum showed that the difference between the above chance accuracy distributions from individual array compared to using both arrays were all statistically significant ($p<0.01$).

When analyzing individual arrays, we found that data captured from MEA1 of NHP-B and MEA0 of NHP-T produced a slightly better overall performance compared to their counterparts in the same monkey (Figures 15J-15L). This contrast between primates can possibly be caused by the decoding activity being differently located within the LPFC for individual animals, or by higher levels of noise for different implants. These findings indicate that the spatial information can be decoded from LPFC neural activity.

3.4.2 Parallel identification of task epochs and maze locations

Since the identification of the locations is particularly strong in areas of the maze associated with important events linked to the successful completion of the task, we decided to analyze the epoch neuronal activity at relevant task events (Figure 16A). Following the same process described for

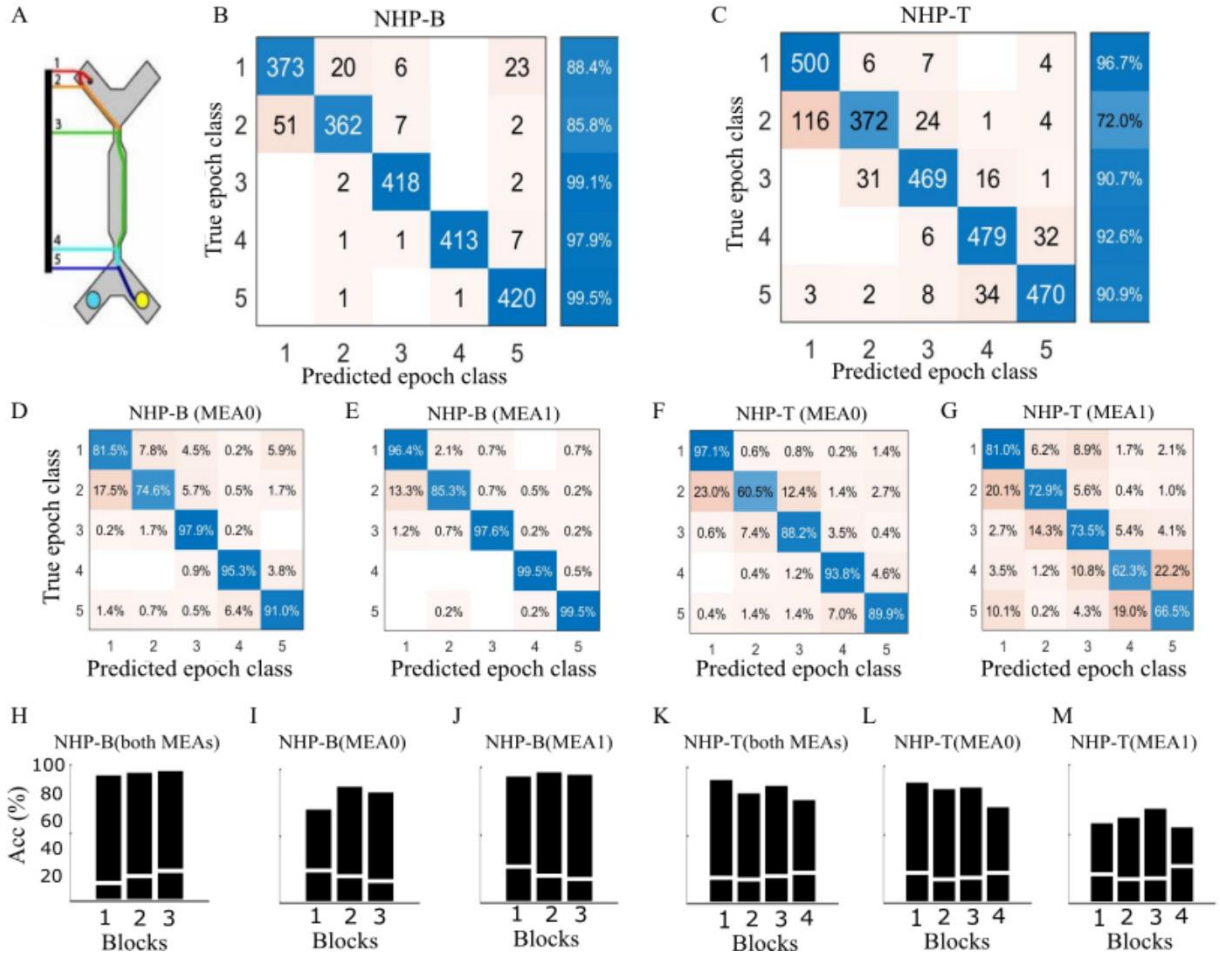

Figure 16. SVM Decoding of epochs from individual and combined blocks, using single or both arrays. (A) Shematic of the maze showing the task epochs onset considered for this analysis. (B) Confusion matrix showing true and predicted classes of decoding the epochs from 422 trials (all blocks) using both arrays on NHP-B. Overall decoding accuracy obtained was 94.1%. (C) Confusion matrix showing true and predicted classes of decoding the 5 task events from 517 trials (all blocks) using both arrays on NHP-T. Overall decoding accuracy obtained was 88.6%. (D)-(E) Confusion matrices showing decoding of the task events for combined blocks on NHP-B MEA0 and NHP-B MEA1 respectively. (F)-(G) Confusion matrices showing decoding of the task events for combined blocks on NHP-T MEA0 and NHP-T MEA1 respectively. (H) SVM decoding accuracy (black) and chance (horizontal white lines) for individual blocks using both arrays for NHP-B. (I)-(J) SVM decoding for individual blocks on NHP-B MEA0 and MEA1 respectively. (K) SVM decoding accuracy for individual blocks using both arrays for NHP-T. (L)-(M) SVM decoding for individual blocks on NHP-T MEA0 and MEA1 respectively.

maze location decoding analysis, we confirmed that the distributions of epoch decoding accuracy compared to its chance level were significantly different for individual and combined arrays

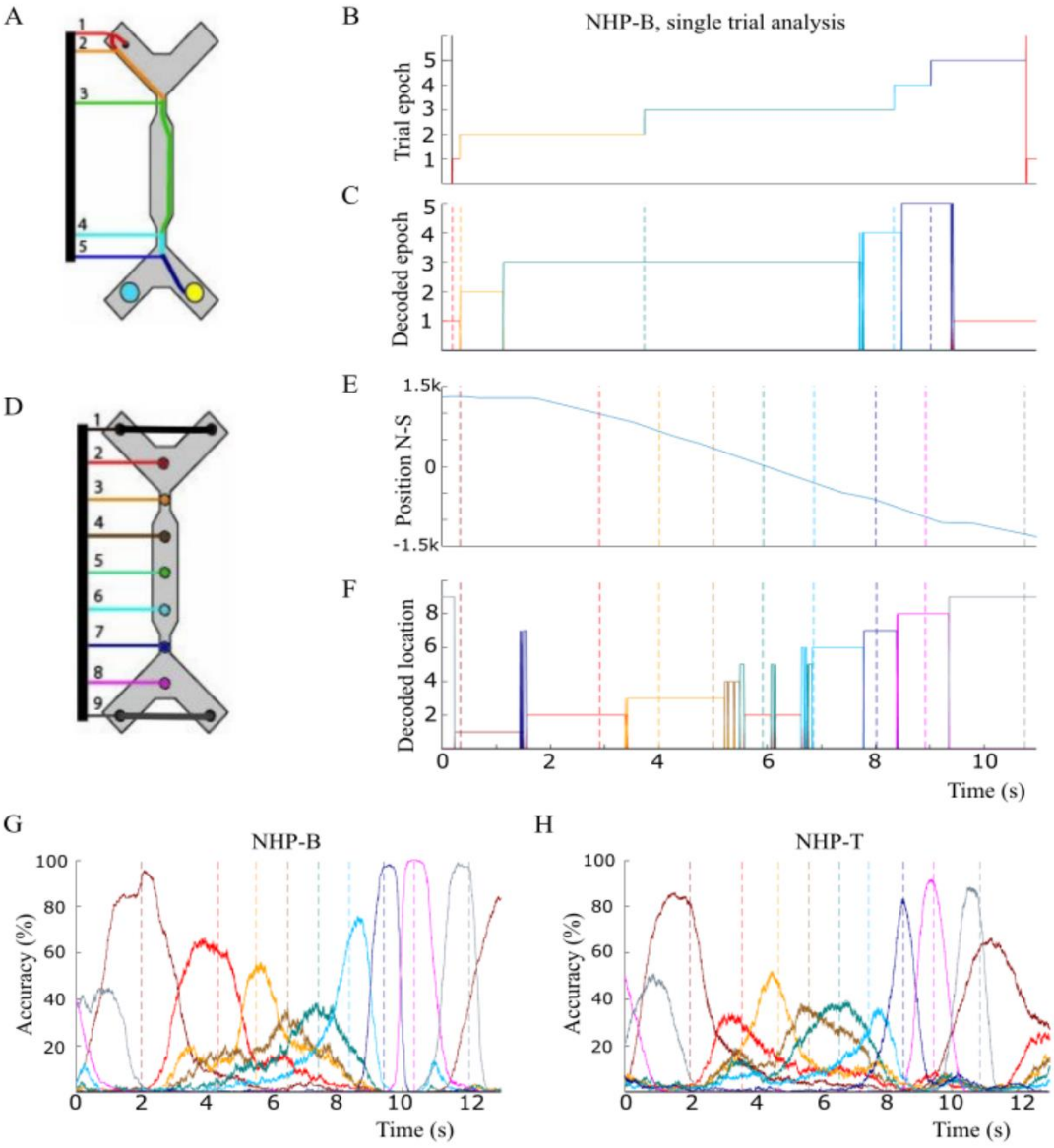

Figure 17. SVM decoding of locations and task epochs over time. Features used in the prediction are spiking rate (1024 msec window) from all available multi-units captured from both MEAs. (A) Schematic of the considered epoch on the maze. (B) Color-coded task epochs over time for an exemplar trial (trial7 of block1 on NHP-B). (C) Prediction of epoch over time for same trial using trained SVM model. (D) Schematic of the considered location points on the maze. (E) Color-coded task locations on the North-South axis of the maze for the same examined trial. (F) Prediction of the maze location over time using trained SVM model. Mean of the decoding accuracy of each location over time, all trials (except training set) being aligned depending on each location for (G) NHP-B and (H) NHP-T.

($p<0.01$). The standard deviations of the obtained accuracy for all blocks were smaller than 3.0%.

The 5-fold cross-validation SVM lead to decoding performances of the 5 epoch transitions at accuracy higher than 94% for NHP-B (Figure 16B) and 88% for NHP-T (Figure 16C) when combining all blocks and data from both arrays. To highlight the impact of array placement on the decoding accuracy results, we also looked at the predicted and true epoch class from all blocks on primates NHP-B (MEA0: Figure 16D, MEA1: Figure 16E) and NHP-T (MEA0: Figure 16F, MEA1: Figure 16G). We found that all task epochs could be well discriminated except for the SOT which would often be confused (23% for array MEA0 on NHP-T) with the previous task epoch (post-reward). Although the difference between above chance distributions were statistically different, testing individual blocks with combined data from both arrays showed a similar performance between blocks on both animals (Figures 16H-16K). However, we found some differences between arrays (NHP-B: Figures 16I-16J and NHP- T: Figures 16L-16M) which were in line with the results found in our spatial response analysis, possibly caused by higher level of noise on those implants.

To better understand the relationship between activity associated with task events and activity associated with spatial locations, we performed a single-trial decoding analysis. To do this, we used a subset of 200 trials from the block with the largest trial set (block2 and block3 for NHP-B and NHP-T respectively) to train two SVM models to decode the task events and the spatial locations using multi-unit activity from both MEAs. Figure 17B shows a typical trial from block1 of NHP-B with its associated task epochs shown on the maze (Figure 17A). The saved SVM model was used to predict the task epoch for every 10 msec time point of the trial (Figure 17C). The vertical dashed lines represent the onset of the color-coded task epoch. For this exemplar trial, all

onsets of the task events were successfully predicted with the model. Unsurprisingly, in the examined trial, the decision point (epoch #5) quickly becomes decoded as the post reward (epoch #1) for the following trial.

We repeated this analysis for spatial locations. Figures 17D-17E show the maze position over time on the North-South axis of the same exemplar trial. Each vertical dashed line represents one of 9 color-coded locations equally spaced on the maze axis and is associated with a particular location point on the maze (Figure 17E). The classification result (Figure 17F), evaluated every 10 msec, shows some misclassifications for locations 4-5 but accurate decoding of the other locations. This analysis demonstrates that within a specific epoch of a trial, it is still possible to decode multiple different locations.

Using the model saved from the prior analysis, we evaluated both primates' average population performance. We tested all trials (excluding the 200 trials used to train the model) and compiled the decoding accuracy around each location point individually. The results highlight the strong decoding at locations that are task-relevant with lower performance while navigating through the long corridor (Figure 17G for NHP-B and figure 17H for NHP-T). The alignment of all trials is based on the position belonging to the exemplar trial. Note that neuronal activity at the first position also caused an increase in predicting the last position associated with the previous trial prior to the maze direction change at the end of the branch. Similarly, the last position of exemplar trial becomes the first position of the next trial, which explains the gradual increase in predicting the first location at the last position.

3.4.3 Decoding performance improvement with a Markov Chain

Since navigation in this task is continuous, the sequence of locations reached at any given time

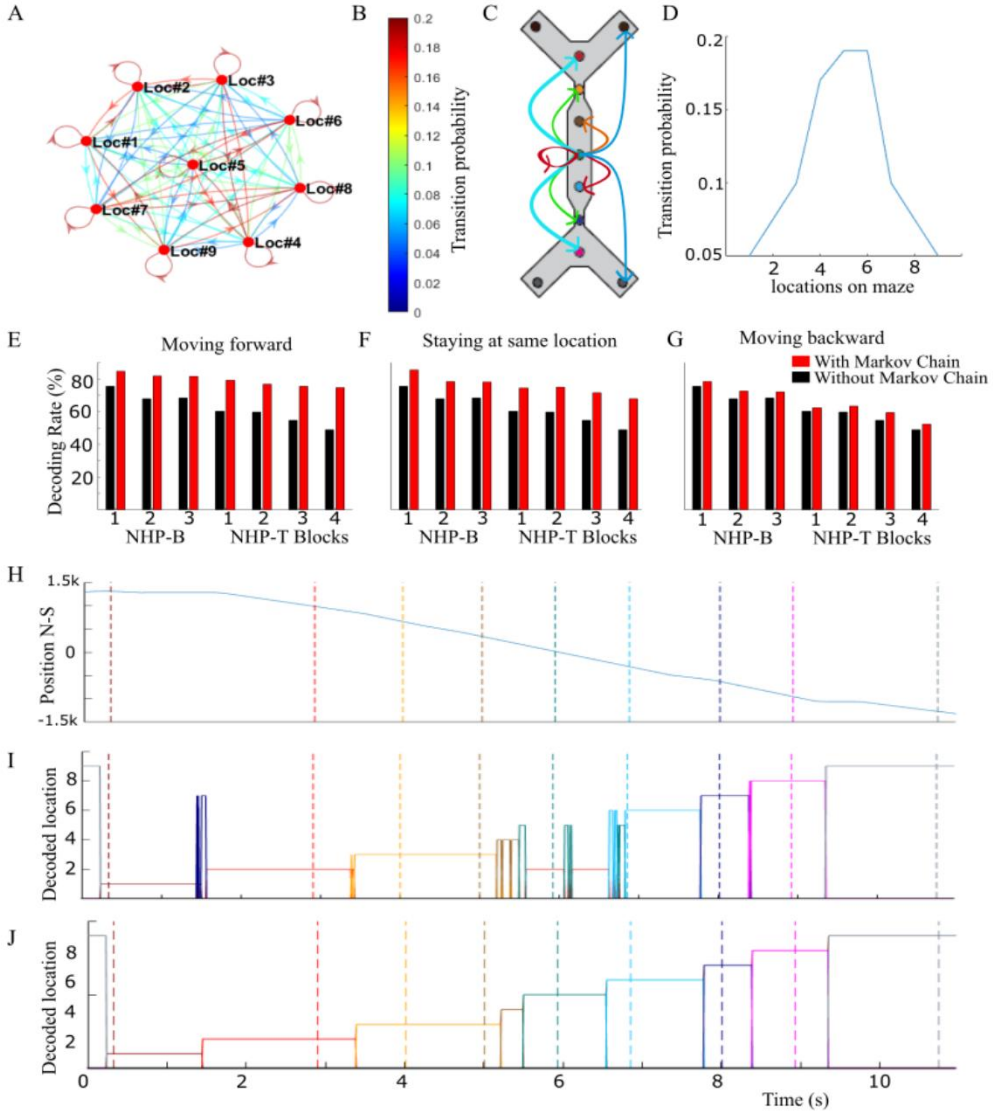

Figure 18. Markov chain impact on spatial locations decoding. (A) Discrete-time Markov chain for the 9 locations showing the transition probabilities between nodes. (B) Transition probability color code legend. (C) Schematic of maze showing the transition probabilities if the prior is at location #5. (D) Showing the probability to move from location #5 to any other locations on the maze. Decoding accuracy obtained originally (black) and with the Markov chain added to the prediction (red) for all blocks on both NHPs using multi-unit data from both arrays assuming that (E) the prior was the previous location (moving forward), (F) the prior was the same location (staying still) and (G) the prior was the next location (moving backward). (H) Color-coded task locations on the North-South axis of the maze for the examined trial in previous analysis (Figure 17). (I) Prediction of the maze location over time using trained SVM model only. (J) Prediction of the maze location over time adding a Markov chain to SVM prediction.

interval is dependent on the probability of moving from one location to the other. If spatial locations were used to control an effector in a BCI system, there would need to be a high level of prediction confidence. We therefore modified the SVM decoder to take advantage of knowledge of previous locations by modifying it with Markov chain inputs. If the prior position is known, the Markov chain probability of a current location is multiplied by the predicted location probability obtained from a trained SVM model.

In the maze task, the position could either be the same or the next forward position since the goal of the task is to move forward. However, in other potential navigation scenarios, there could be the possibility of backward movement or missing the feedback signal of the prior position. We designed a chain with the highest transition probabilities for moving in the forward direction or staying at the same place, and a low probability of moving backward or to the further locations (Figures 18A-18D). We tested our trials with and without applying the Markov chain assuming our prior location was either the same (Figure 18F), the previous (Figure 18E), or a future location (Figure 18G). Using features based on the multi-unit activity on both arrays, we averaged the previously saved model decoding accuracy for all trials on individual blocks (excluding the training data). The result of applying the Markov chain is an overall and consistent improvement of our decoding performance on both animals regardless of the prior location being same, forward, or backward.

At the trial level, we repeated the previous analysis on the same example trial (Figures 18H-18I), with the addition of the described Markov chain to the prediction path (Figure 18J). The prediction of locations followed a more regular navigation path. Additionally, location #5, which was missed in the previous non-stochastic decoder, was decoded correctly.

3.4.4 Canonical space projection of the multi-unit spiking activity

To better understand the number of channels required to decode location, we performed a "greedy channel analysis" (Leavitt et al. 2017). To do this, we first found the individual multi-unit signal which provided the highest decoding accuracy. We saved this first signal deemed our best unit.

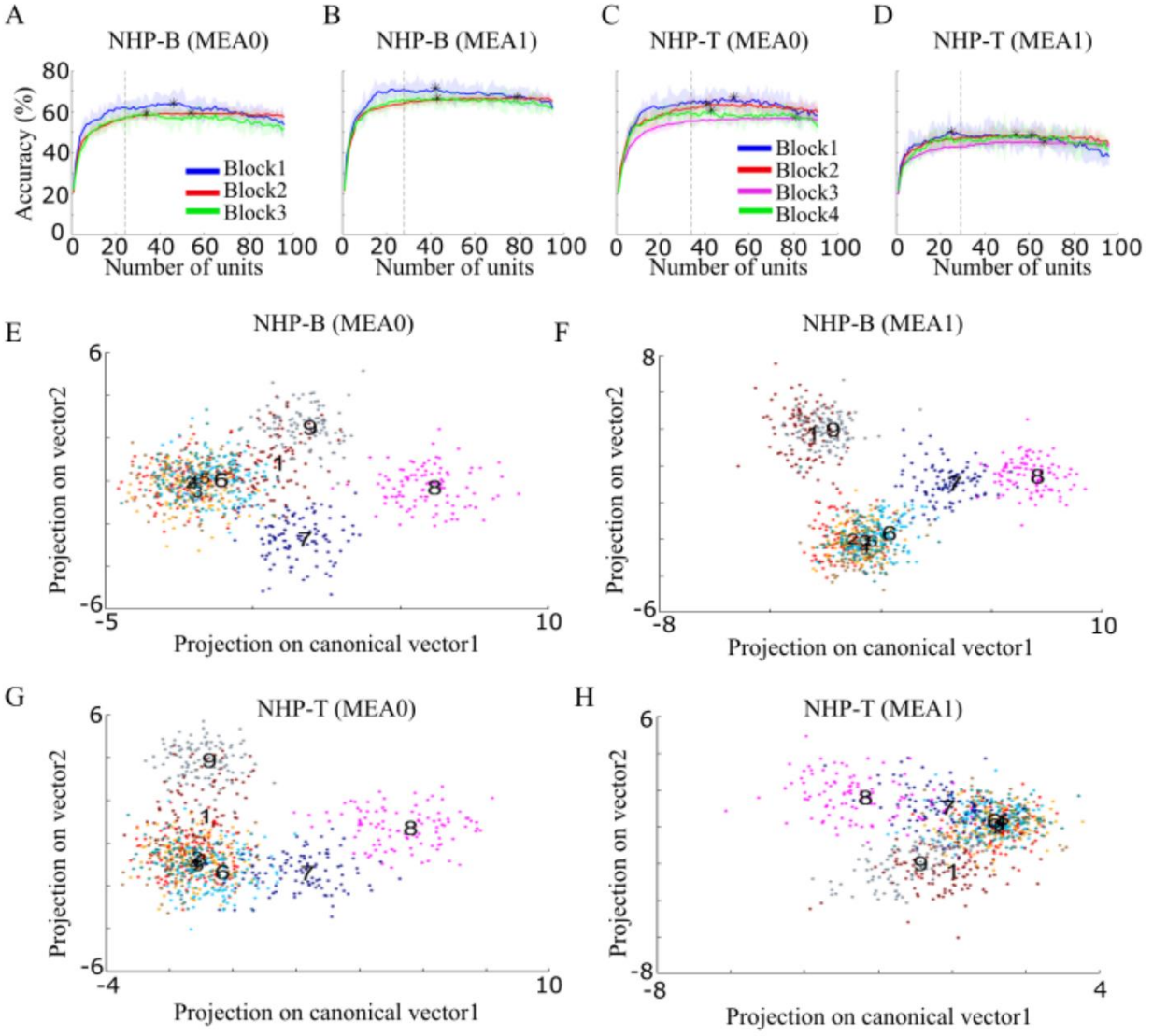

Figure 19. Analysis of multi-unit's impact on the decoding accuracy. Decoding accuracy for increasing multi-units for (A) NHP-B (MEA0), (B) NHP-B (MEA1), (C) NHP-T (MEA0), (D) NHP-T (MEA1). Projections in the canonical space of the multi-unit activity for 100 trials at locations 1 to 9 on monkeys (E) NHP-B (MEA0), (F) NHP-B (MEA1), (G) NHP-T (MEA0), (H) NHP-T (MEA1).

The decoding accuracy was then evaluated for this unit combined with each remaining unit to find and save what we called our second-best unit. We repeated this process for the third unit up to all units, maximizing the decoding accuracy at each step. The mean accuracy and the 95% confidence level obtained for all blocks are presented for NHP-B (Figures 19A-19B) and NHP-T (Figures 19C-19D). The results suggest that the peak decoding (stars on Figures 19A-19D) is reachable with at most 28 and 34 multi-units for NHP-B and NHP-T respectively (vertical dashed lines on Figures 19A-19D). In all cases, most of the decoding accuracy is achieved with around 10 units.

Having shown that each unit provides its own contribution for decoding the locations and that only a subset of the population is required to reach the peak decoding accuracy, we investigated the possibility to improve processing requirement using canonical space vectors. To identify 9 locations, the canonical discriminant analysis of each array generates 8 vectors of size equal to the number of multi-units. This canonical space analysis produces weights that maximize the unit activity differences for decoding all the considered spatial locations. SVM features based on the spiking rate projected on these vectors are then used to decode the locations more efficiently (factor reduction of 12 for one array: #multi-units/#canonical vectors). Consistent in both animals and arrays, the projection of the multi-unit spiking activity on the top 2 canonical vectors for 100 trials (Figures 19E-19H) demonstrates better separation for locations 1,7,8,9 in line with our previous SVM decoding results. The trial grouping for locations on individual array seem to also reflect the stronger decoding performance on MEA1 for NHP-B (Figure 19F) and on MEA0 for NHP-T (Figure 19G) mainly by improving the grouping and showing some separation for location 6. Note that the projection on the other vectors would improve the location separation further but the top

2 vectors provide approximately 79% of the cumulative variance explained (NHP-B MEA0:79.7%, MEA1: 79.6%, NHP-T MEA0:79.1%, MEA1: 78.9%).

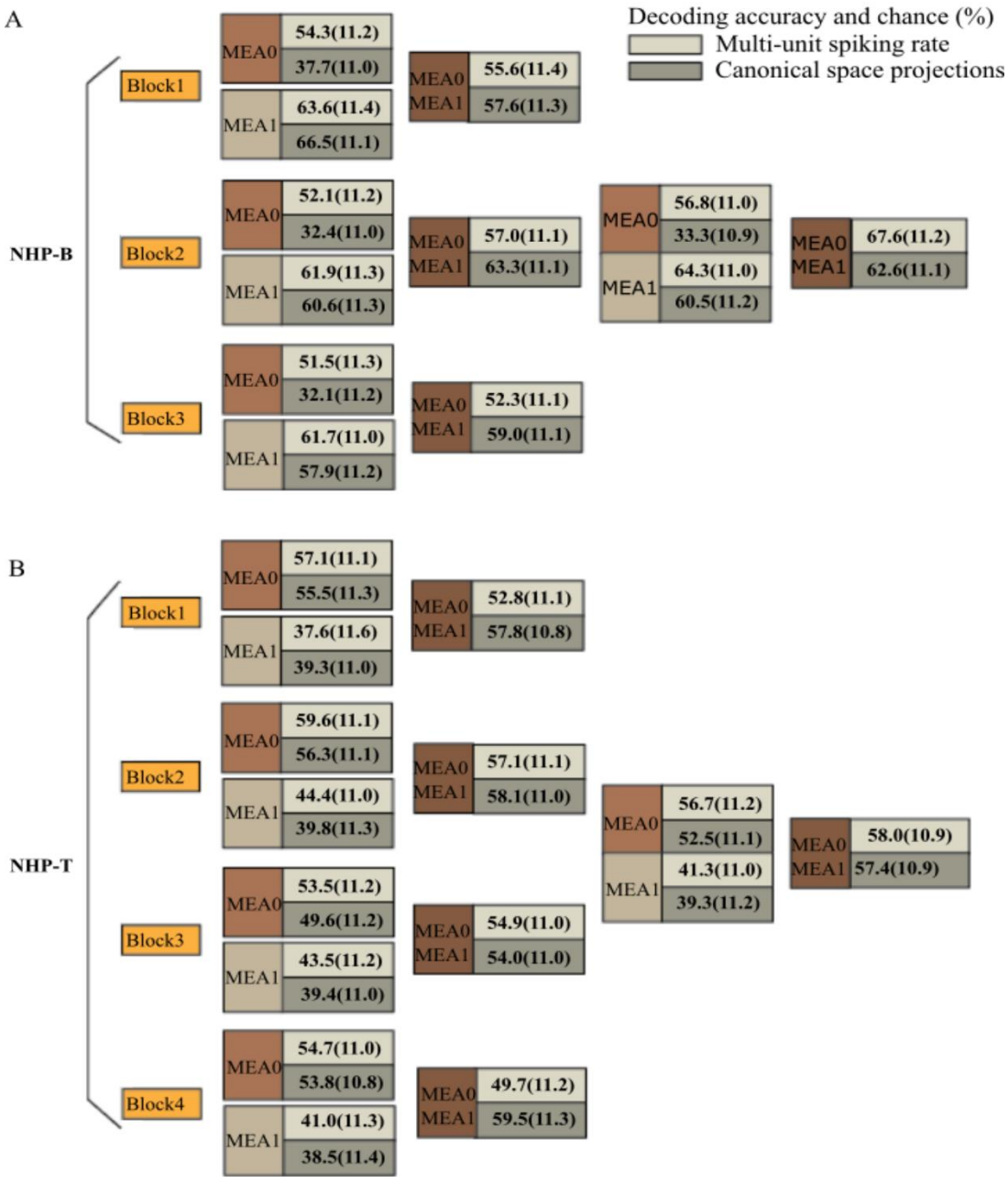

Figure 20. Comparison of SVM decoding using features based on multi-unit spiking rate versus their canonical space projections. Breakdown of decoding accuracy (chance level from shuffling the labels) from individual blocks on individual arrays to data from all blocks on both arrays for (A) NHP-B, and (B) NHP-T. All compared pair distributions were statistically different ($p < 0.001$).

We compared the SVM accuracy performance for decoding 9 locations from features based on the multi-unit spiking rate against features from the canonical space projections. For each feature set and its shuffled counterpart, we first performed a 5-fold cross-validation SVM analysis and averaged the returned 5-fold accuracies. We then repeated this process 100 times to obtain a distribution of results, reporting its mean as the accuracy. The locations were decoded using data from individual blocks on each array. We also applied the decoder to both arrays (Figure 20, second column), individual arrays with the blocks combined (Figure 20, third column), and combined arrays and blocks (Figure 20, fourth column). The statistical analysis distribution of all pairs showed small but statistically significant differences between methods ($p<0.01$). Overall, the canonical space projections were slightly less reliable, possibly due to the change in the multi-unit contribution between the trials used to train the canonical vectors, and the tested trials. However, this method required a much smaller feature set, which could be advantageous for real-time applications.

3.5 Discussion

We examined the neuronal activity in non-human primates' LPFC while they freely navigate through a virtual maze. While the LFP based signal and spiking activity of the population showed selectivity for maze locations, use of the latter provided better decoding accuracy of different spatial positions along the maze. We also demonstrated that decoding of spatial locations from neural activity improves using a Markov chain model. We focus on multi-unit spiking rate as this signal is well suited for the real-time demands of an iBCI system.

3.5.1 Decoding of space in the primate brain

Previous studies have reported that decoding of spatial positions is possible by reading out the spiking activity of place cells in brain areas such as the hippocampus of rodents during spatial navigation tasks (O'Keefe and Dostrovsky 1971, Buzsáki and Moser 2013, Spellman et al. 2015). Studies of spatial navigation in primates are scarcer, and the activity of hippocampus cells has been associated with encoding of gaze-position (Rolls and Xiang 2006, Ekstrom et al. 2003), while other studies have demonstrated encoding of spatial location modulated by the contingencies of the task (Rolls and Wirth 2018, Gulli et al. 2020, Baraduc et al. 2019). Although the hippocampus may seem, at first glance, an appropriate target for a BCI that supports spatial navigation, its location, deep in the temporal lobe, makes it less accessible to surgeries and chronic implants with many electrodes.

Other studies have shown that it is possible to build a BCI that utilizes neural activity recorded in premotor areas of macaque monkeys to navigate a cart through a physical environment (Rajangam et al. 2016). The premotor cortex directly receives information from the LPFC about the conceptual planning of movements to locations (Nakayama et al. 2008). In principle, it is reasonable to assume the LPFC and the premotor cortex, nearby and posterior to the arcuate (Petrides 2005) work in tandem in the planning and execution of commands for spatial navigation.

Previous research has shown that task epochs and target locations can be decoded from LPFC activity in macaques (Boulay et al. 2016, Johnston et al. 2021, Roussy et al. 2021, Lennert and Martinez-Trujillo 2013). Recently, Vogel et al. (2022) demonstrated that neurons in the mouse prefrontal cortex are required for maintenance, encoding, and retrieval of information in spatial working memory. They also reported that in their spatial working memory task, the rodent's spatial position in the physical maze had the largest influence on the prefrontal cortex neuronal activity.

The population decoding of locations during virtual navigation was, to our knowledge, never examined before. We demonstrated that eleven spatial locations along the North-South axis of a virtual maze could be decoded using 5-fold cross-validation SVM classifiers. Decoding was higher at locations where behavior associated with specific task events and reward took place. The prefrontal cortex is known to respond to reward expectation (Leon and Shadlen 1999, Watanabe 2007). The successful decoding of the starting and ending branch (left or right) during the post reward and end of trial epochs of the task eliminate the possibility that this selectivity was associated with the trial time to reward.

The five epochs associated with the key task events could also be identified from the same population. To understand the dependencies of epoch related neuronal activity on locations we looked at the decoding of their parallel identification in a single trial using a saved SVM model. Our results showed that within the same task event, multiple locations can be identified.

Most BCI implementations decode the movement intentions from motor cortex neuronal activity to control assistive devices (Shenoy et al. 2013, Collinger et al. 2013). Recently, studies have demonstrated the possibility to better guide iBCI effectors using discrete movement intentions (Fan et al. 2014), states (Sumsky et al. 2017, Kao et al. 2017), transitions (Kang et al. 2015), and goals (Andersen et al. 2019) decoded from other cortical areas of the brain. In line with this strategy, our results show that spatial locations within a physical or virtual environment can be deciphered from the LPFC intracortical activity, possibly to assist in the control of intelligent wheelchairs. In addition, knowing the region of interest within a tailored map, could control a robotic apparatus, assistive device, or even provide clues on what the user intends to do depending on the content of the selected location.

In our study, the virtual environment did not include landmarks other than the end goal colored disk. This disk became visible once the end of the maze corridor was reached and was located in one of two possible branches depending on the trial context. In such task scenario, we suspect the animal used an egocentric reference frame where the coded spatial positions in the maze were relative to the estimated end goal or the maze intersection points. Future research should add landmarks through the maze and investigate the effect on the spatial locations decoding accuracy in an allocentric reference frame.

3.5.2 Maximizing performance for iBCI systems

In real-time and critical application such as an iBCI, the decoder accuracy must be reliable since the failures will significantly impact the user's satisfaction and its benefit. In navigation, reaching a future position depends on the current location, and the associated probability between them. Such processes which retain no memory of past states are called Markov processes (Norris 1998). Markov chains, which are finite sets of state transition probabilities, have been used to model cellular signal processing (Said et al. 2003), to forecast daily precipitation (Bojar et al. 2018), and to simulate sleep electroencephalography patterns (Zung et al. 1965). We evaluated the possibility to improve the decoding performance by modifying the locations' probabilities predicted by the SVM with the transition probabilities embedded in the Markov chain. As expected, with a designed Markov chain favoring the forward navigation, we obtained valuable prediction accuracy improvements. Future work should look at how the state transition probability matrix of the Markov chain could be dynamically updated based on past trials, to better represent the environment and navigational constraints.

3.5.3 Canonical discriminant analysis

To reduce processing requirement, we further investigated how a canonical discriminant analysis could optimize the contributions of multi-unit activity for locations' selectivity while reducing the overall size of the feature set. The result for individual blocks and arrays as well as combined blocks and arrays was that the original multi-unit feature set performed better than its projections in canonical space. However, for individual blocks on combined arrays, the projected multi-unit signal performed better overall. The feature set size was reduced by over elevenfold using the canonical space which may be important in the design of an iBCI system.

3.5.4 BCI application

In principle, we reasoned that as reported by Downey et al. (2016), combining information from both, a BCI system and vision-guided autonomous robotics, can improve the control of an assistive device used for navigation or other purposes. One may ask, could lateral prefrontal cortex activity contribute to a BCI? The LPFC has been classically associated with high level cognition, planning and executive function (Miller et al. 2001, Fuster 2015). Neuronal ensembles in the LPFC, the area we recorded from in this study, encode spatial attention (Backen et al. 2018, Tremblay et al. 2015), movement goals (Boulay et al. 2016), and short-term memory (Leavitt et al. 2017) in spatiocentric coordinates, rather than in retinal coordinates, as many areas located more posteriorly in the brain (Crawford et al. 2003). Moreover, LPFC ensemble codes reflect the biases in space processing observed during behavior (Leavitt et al. 2017). Finally, LPFC activity undergoes gain control within the area microcircuit, which calibrates neural activity for changes in environmental variables such as stimulus intensity (Bullock et al. 2017, Duong et al. 2019). Together with its location at the top of the sensory processing hierarchy (Felleman and Essen 1991), the findings

reported in LPFC electrophysiological studies in non-human primates indicate that the computations performed in this area are at the final stage of visual and perceptual integration in primate brains such as the ones of macaques and humans. If a BCI were to incorporate aspects of cognition and executive control, a combination of LPFC and motor cortex interfaces may achieve more functionality than either of them alone (Pesaran et al. 2006, Andersen et al. 2010, Andersen et al. 2004).

One specific example of how LPFC activity can aid a motor cortex BCI is to encode desired locations in space-centered coordinates while navigating through an environment (in our scenario the virtual maze), and planning multiple sequential actions (e.g., visiting different locations in a sequence). For a BCI to assist in such tasks in the presence of eye movements and possibly changes in body position, it would be ideal to encode goals in space-centered frames, and it must be robust enough to ignore the interference produced by eye movements. LPFC ensembles encode goals in a space-centered frame independently of eye and arm movements (Roussy et al. 2022). This intended target location could provide valuable information and possibly improve the control of a navigation system (e.g., a wheelchair) that does sequential actions (Andersen et al. 2019). Other possible candidates for contributing to cognitive BCIs that encode space-center goals is the posterior parietal cortex (Andersen et al. 1985). This area has been the target of BCI studies (Andersen et al. 2004, Andersen et al. 2019). Whether BCIs using a combination of posterior parietal cortex, LPFC and motor cortex activity could be more effective for real world tasks than BCIs using one or two of these areas as targets remains speculative. Additional studies must be conducted to address these questions.

3.6 Conclusion

We examined the spiking and LFP activity recorded from the lateral prefrontal cortex of non-human primates while they navigated through a virtual maze. We found that the spatial locations within the maze could be decoded using SVM on those features, particularly well at locations associated with events relevant to the successful completion of the task. We investigated the effects of adding a Markov chain to the SVM decoder and concluded that it significantly improves the location decoding accuracy. Assuming similar activity can be extracted from humans and macaques LPFC during navigation, our results suggest that a goal based iBCI implant in LPFC could provide useful spatial information to support a navigation-based application for patients with disabilities.

3.7 Acknowledgements

We are thankful for the support of the neuroscience program at the Ottawa Hospital Research Institute as well as the support from the University of Ottawa Brain and Mind Research Institutes. This work was supported by the Canadian Institute of Health Research Project Grant and Natural Sciences and Engineering Research Council of Canada (NSERC).

3.8 References

[1] Ajiboye AB, Willett FR, Young DR, Memberg WD, Murphy BA, Miller JP, et al. Restoration of reaching and grasping movements through brain-controlled muscle stimulation in a person with tetraplegia: a proof-of-concept demonstration. The Lancet [Internet]. 2017;389(10081):1821–30.

[2] Al-qaysi, ZT, Zaidan, BB, Zaidan, AA, & Suzani, MS. A review of disability EEG based wheelchair control system: Coherent taxonomy, open challenges and recommendations. Computer Methods and Programs in Biomedicine. 2018;164:221–237.

[3] Andersen RA, Aflalo T, Kellis S. From thought to action: The brain–machine interface in posterior parietal cortex. Proceedings of the National Academy of Sciences of the United States of America [Internet]. 2019;116(52):26274.

[4] Andersen RA, Burdick JW, Musallam S, Pesaran B and Cham JG. Cognitive neural prosthetics. Trends Cogn Sci. 2004;8:486-493.

[5] Andersen RA, Essick GK and Siegel RM. 1985 Encoding of spatial location by posterior parietal neurons. Science. 1985;230(4724):456-458.

[6] Andersen RA, Hwang EJ and Mulliken GH. 2010 Cognitive neural prosthetics. Annu Rev Psychol. 2010;61:169-190.

[7] Backen T, Treue S and Martinez-Trujillo J. Encoding of spatial attention by primate prefrontal cortex neuronal ensembles. eNeuro. 2018;5**:**ENEURO.0372-16.2017

[8] Baraduc P, Duhamel JR and Wirth S. Schema cells in the macaque hippocampus. Science. 2019;363:635–639.

[9] Bojar W, Knopik L, Żarski J, Kuśmierek-Tomaszewska R and Żarski W. Markov chain as a tool for forecasting daily precipitation in the vicinity of the city of Bydgoszcz, Poland. ITM Web Conf. 2018;23:00003

[10] Boulay CB, Pieper F, Leavitt M, Martinez-Trujillo J and Sachs AJ. Single-trial decoding of intended eye movement goals from lateral prefrontal cortex neural ensembles. Journal of neurophysiology. 2016;115**:**486-499.

[11] Bullock KR, Pieper F, Sachs AJ and Martinez-Trujillo JC. Visual and presaccadic activity in area 8Ar of the macaque monkey lateral prefrontal cortex. J Neurophysiol. 2017;118:15-28.

[12] Buschman TJ, Denovellis EL, Diogo C, Bullock D and Miller EK. Synchronous Oscillatory Neural Ensembles for Rules in the Prefrontal Cortex. Neuron. 2012;76:838–846.

[13] Buzsáki G and Moser EI. Memory, navigation and theta rhythm in the hippocampal-entorhinal system. Nat. Neurosci. 2013;16:130–138.

[14] Chambers JM. Linear models, in Statistical Models, eds. J.M.Chambers and T. J. Hastie (Wadsworth & Brooks/Cole). 1992.

[15] Chen S, Shu X, Wang H, Ding L, Fu J and Jia J. The Differences Between Motor Attempt and Motor Imagery in Brain-Computer Interface Accuracy and Event-Related Desynchronization of Patients With Hemiplegia. Front. Neurorobot. 2021;15:1–13.

[16] Collinger JL, Wodlinger B, Downey JE, Wang W, Tyler-Kabara EC, Weber DJ, et al. High-performance neuroprosthetic control by an individual with tetraplegia. The Lancet [Internet]. 2013;381(9866):557–64.

[17] Corrigan BW, Gulli RA, Doucet G, Roussy M, Luna R, Sachs AJ and Martinez-Trujillo J. Different neural codes serve long and short-term memory functions in primate Hippocampus and Lateral Prefrontal Cortex during virtual navigation. bioRxiv. 2021;08.20:457136.

[18] Crawford JD, Martinez-Trujillo JC and Klier EM. Neural control of three-dimensional eye and head movements. Curr Opin Neurobiol. 2003;13:655-662.

[19] Curtis CE and D'Esposito M. Persistent activity in the prefrontal cortex during working memory. Trends Cogn. Sci. 2003;7:415–423.

[20] Doucet G, Gulli RA and Martinez-Trujillo J. Cross-species 3D virtual reality toolbox for visual and cognitive experiments. J. Neurosci. Methods. 2016;266:84–93.

[21] Downey JE, Weiss JM, Muelling K, Venkatraman A, Valois JS, Hebert M, Bagnell JA, Schwartz AB, and Collinger JL (2016). Blending of brain-machine interface and vision-guided autonomous robotics improves neuroprosthetic arm performance during grasping. Journal of NeuroEngineering and Rehabilitation. 2016;13(1), 1–12.

[22] Duong L, Leavitt M, Pieper F, Sachs A and Martinez-Trujillo J. A normalization circuit underlying coding of spatial attention in primate lateral prefrontal cortex. Eneuro. 2019;6:ENEURO.0301-18.2019

[23] Ekstrom AD, Kahana MJ, Caplan JB, Fields TA, Isham EA, Newman EL and Fried I. Cellular networks underlying human spatial navigation. Nature. 2003;425:184–187.

[24] Fan JM, Nuyujukian P, Kao JC, Chestek CA, Ryu SI and Shenoy K. Intention estimation in brain-machine interfaces. J. Neural Eng. 2014;11.

[25] Fan RE, Chang KW, Hsieh CJ, Wang XR and Lin CJ 2008 LIBLINEAR: A library for large linear classification. J. Mach.Learn.Res. 2008;9:1871– 1874.

[26] Felleman DJ and Essen DCV. Distributed hierarchical processing in the primate cerebral cortex. Cereb Cortex. 1991;1:1-47.

[27] Friendly M and Fox J. Candisc: Visualizing generalized canonical discriminant and canonical correlation analysis, R package version 0.8-3. 2020.

[28] Flint RD, Lindberg EW, Jordan LR, Miller LE and Slutzky MW. Accurate Decoding of Reaching Movements from Field Potentials in the absence of Spikes. J. Neural Eng. 2012;9:1–22.

[29] Fuster JM. Anatomy of the prefrontal cortex. The Prefrontal Cortex (Elsevier), 2015;9-62

[30] Gulli RA, Duong LR, Corrigan BW, Doucet G, Williams S, Fusi S and Martinez-Trujillo J. Context-dependent representations of objects and space in the primate hippocampus during virtual navigation. Nat. Neurosci. 2020;23:103–112.

[31] Jansen-Osmann P. Using desktop virtual environments to investigate the role of landmarks. Comput. Human Behav. 2002;18:427–436.

[32] Johnston R, Doucet G, Boulay C, Miller K, Martinez-Trujillo J and Sachs A. Decoding Saccade Intention from Primate Prefrontal Cortical Local Field Potentials Using Spectral, Spatial, and Temporal Dimensionality Reduction. Int. J. Neural Syst. 2021;31:1–19.

[33] Jung MW, Qin Y, McNaughton BL and Barnes CA. Firing characteristics of deep layer neurons in prefrontal cortex in rats performing spatial working memory tasks. Cereb. Cortex. 1998;8:437–450.

[34] Kang X, Sarma SV, Santaniello S, Schieber M and Thakor NV. Task-Independent Cognitive State Transition Detection From Cortical Neurons During 3-D Reach-to-Grasp Movements. IEEE Trans. Neural Syst. Rehabil. Eng. 2015;23:676–682.

[35] Kao JC, Nuyujukian P, Ryu SI and Shenoy K. A High-Performance Neural Prosthesis Incorporating Discrete State Selection with Hidden Markov Models. IEEE Trans. Biomed. Eng. 2017;64:935–945.

[36] Leavitt ML, Pieper F, Sachs AJ and Martinez-Trujillo J. A quadrantic bias in prefrontal representation of visual-mnemonic space. Cereb Cortex. 2017;52:1-17.

[37] Leavitt ML, Pieper F, Sachs AJ and Martinez-Trujillo J. Correlated variability modifies working memory fidelity in primate prefrontal neuronal ensembles. Proc. Natl. Acad. Sci. U. S. A. 2017;114:E2494–E2503.

[38] Lee SA. The boundary-based view of spatial cognition: a synthesis. Curr. Opin. Behav. Sci. 2017;16:58–65.

[39] Lennert T and Martinez-Trujillo J. Prefrontal neurons of opposite spatial preference display distinct target selection dynamics. J. Neurosci. 2013;33:9520–9529.

[40] Leon MI and Shadlen MN. Effect of expected reward magnitude on the response of neurons in the dorsolateral prefrontal cortex of the macaque. Neuron. 1999;24(2):415–425.

[41] Markowitz DA, Wong YT, Gray CM and Pesaran B. Optimizing the decoding of movement goals from local field potentials in macaque cortex. J. Neurosci. 2011;31:18412–18422.

[42] May M and Klatzky RL. Path Integration while Ignoring Irrelevant Movement. J. Exp. Psychol. Learn. Mem. Cogn. 2000;26:169–186.

[43] Maynard EM, Nordhausen CT and Normann RA. The Utah Intracortical Electrode Array: a recording structure for potential brain-computer interfaces. Electroencephalogr Clin Neurophysiol. 1997;102:228–239.

[44] Mendoza-Halliday D and Martinez-Trujillo J. Neuronal population coding of perceived and memorized visual features in the lateral prefrontal cortex. Nat. Commun. 2017;8:1–13.

[45] Miller KJ, Honey CJ, Hermes D, Rao RPN, denNijs M and Ojemann JG. Broadband changes in the cortical surface potential track activation of functionally diverse neuronal populations. Neuroimage. 2014;85:711–720.

[46] Miller EK and Cohen JD. An integrative theory of prefrontal cortex function. Annu Rev Neurosci. 2001;24:167-202.

[47] Miller EK, Lundqvist M and Bastos AM. Working Memory 2.0. Neuron. 2018;100:463–475.

[48] Miller KJ, Zanos S, Fetz EE, DenNijs M and Ojemann JG. Decoupling the cortical power spectrum reveals real-time representation of individual finger movements in humans. J. Neurosci. 2009;29:3132–3137.

[49] Nakayama Y, Yamagata T, Tanji J and Hoshi E. Transformation of a virtual action plan into a motor plan in the premotor cortex. J. Neurosci. 2008;28:10287–10297.

[50] Normann RA, Maynard EM, Rousche PJ and Warren DJ. A neural interface for a cortical vision prosthesis. Vision Res. 1999;39:2577–2587.

[51] Norris JR. Markov chains (No. 2). Cambridge university press. 1998.

[52] O'Keefe J and Dostrovsky J. Short Communications The hippocampus as a spatial map. Preliminary evidence from unit activity in the freely-moving rat. Brain Res. 1971;34:171–175.

[53] Pandarinath C, Nuyujukian P, Blabe CH, Sorice BL, Saab J, Willett FR, Hochberg L, Shenoy K and Henderson JM. High performance communication by people with paralysis using an intracortical brain-computer interface. Elife. 2017;6.

[54] Pesaran B, Musallam S and Andersen RA. Cognitive neural prosthetics. Curr Biol. 2006;16:77-80.

[55] Petrides M. Lateral prefrontal cortex: Architectonic and functional organization. Philos. Trans. R. Soc. B Biol. Sci. 2005;360:781–795.

[56] Rajangam S, Tseng PH, Yin A, Lehew G, Schwarz D, Lebedev MA and Nicolelis AY. Wireless cortical brain-machine interface for whole-body navigation in primates. Sci. Rep. 2016;6:1–13.

[57] Ramsay JO and Silverman W. Canonical correlation and discriminant analysis, in Functional Data Analysis. Springer Series in Statistics (Springer, New York). 1997.

[58] Rolls ET and Wirth S. Spatial representations in the primate hippocampus, and their functions in memory and navigation. Prog. Neurobiol. 2018;171:90–113.

[59] Rolls ET and Xiang JZ. Spatial View Cells in the Primate Hippocampus, and Memory. Hippocampal Place Fields Relev. to Learn. Mem. 2006;200:175–200.

[60] Roussy M et al. Ketamine disrupts naturalistic coding of working memory in primate lateral prefrontal cortex networks. Mol. Psychiatry. 2021;26:6688-6703.

[61] Roussy M, Corrigan B, Luna R, Gulli RA, Sachs AJ, Palaniyappan L, and Martinez-Trujillo JC. Stable working memory and perceptual representations in macaque lateral prefrontal cortex during naturalistic vision. J Neurosci. 2022;42:JN-RM-0597-22.

[62] Said MR, Oppenheim AV and Lauffenburger DA. Modeling cellular signal processing using interacting Markov chains. ICASSP, IEEE Int. Conf. Acoust. Speech Signal Process. - Proc. 2003;6:41–44.

[63] Santhanam G, Ryu SI, Yu BM, Afshar A and Shenoy K. A high-performance brain-computer interface. Nature. 2006;442:195–198.

[64] Shenoy K, Sahani M and Churchland MM. Cortical control of arm movements: A dynamical systems perspective. Annu. Rev. Neurosci. 2013;36:337–359.

[65] Spellman T, Rigotti M, Ahmari SE, Fusi S, Gogos JA and Gordon JA. Hippocampal-prefrontal input supports spatial encoding in working memory. Nature. 2015;522:309–314.

[66] Sumsky SL, Schieber MH, Thakor NV, Sarma SV and Santaniello S. Decoding kinematics using task-independent movement-phase-specific encoding models. IEEE Trans. Neural Syst. Rehabil. Eng. 2017;25:2122–2132.

[67] Tremblay S, Pieper F, Sachs A and Martinez-Trujillo J. Attentional filtering of visual information by neuronal ensembles in the primate lateral prefrontal cortex. Neuron. 2015;85:202–215.

[68] Vogel P, Hahn J, Duvarci S and Sigurdsson T. Prefrontal pyramidal neurons are critical for all phases of working memory. Cell Rep. 2022;39:110659.

[69] Wallis JD, Anderson KC and Miller EK. Single neurons in prefrontal cortex encode abstract roles. Nature. 2001;411:953–956.

[70] Watanabe M. Role of anticipated reward in cognitive behavioral control. Current Opinion in Neurobiology. 2007;17(2)**:**213–219.

[71] Wilcoxon F. Individual comparisons by ranking methods. Biometr. Bull. 1945;1:196-202.

[72] Wilkinson N and Rogers CE. Symbolic description of factorial models for analysis of variance. Appl. Statist. 2973;22:392-399.

[73] Zung W, Naylor T, Gianturco D and Wilson W. Computer simulation of sleep EEG patterns with a Markov chain model. Recent Adv Biol Psychiatry. 1965;8:335–355.

Chapter 4

Cognitive Activity Exploration

4.1 Introduction

Understanding human cognition and the intricate workings of our thoughts has captivated the curiosity of many researchers and psychologists. With advanced neuroimaging techniques, brain recording methods, and analytics tools, the research community has acquired a solid foundation for associating brain regions with cognitive functions. It is now possible to identify brain activity associated with perception, memory, decision-making, movement planning, and other cognitive processes. The primate brain operates as a dynamic, and interconnected network to accomplish goals. Its neural correlates associated with cognition are influenced by a myriad of factors including emotions, context, prior experiences, and individual preferences. In real world scenarios, extrapolating complex intentions amid those factors still needs further research and investigation.

In this chapter, I describe a methodology to explore brain signals associated with cognitive functions with the goal of use on NCC participants. This includes a description of the tasks, recording equipment and synchronization, user interface, and analysis pipeline. In Chapter 5, I describe application of the analysis and validation to previously collected ECoG data in an NBack task. This endeavor required the development of experimental tasks designed to trigger cognitive activity that are considered as possible factors associated with human intention. In each session, recorded with the labstreaming layer (LSL), the timely synchronized brain signals (i.e., EEG, ECoG, sEEG, MEA) and task events are captured while participants engage in specific cognitive tasks. The exploration of the sessions takes place offline through a designed Matlab GUI. The

session parameters are first selected, then signals and associated task events are preprocessed and loaded for further investigation. Finally, signal processing tools are available through the GUI to explore and visualize the modulation of field potentials based features around important task events for single or averaged subsets of trials.

4.2 Cognitive Tasks Developed

To investigate the modulation effect and the brain regions involved with cognitive activity, we selected three known cognitive tasks that engage goal encoding (Table 9), modified to be used by a participant with tetraplegia (either using saccades, or a BCI). These tasks were developed using the Unity platform and designed to stream task events using LSL. They were chosen based on their ability to simultaneously activate minimal cognitive functions, allowing for the detection of specific brain areas involved in a particular activity.

Table 9. Cognitive tasks.

Task	Description
Delayed Saccade Task	Target saccade intent
NBack with number (NBack1,2,3)	Working memory
Visual Spatial Attention	Covert visual spatial attention

4.3 Session Recordings

For the development and testing of the methodology, Emotiv and g.tech EEG systems were used to capture brain activity from 5 volunteers while they performed one or all cognitive tasks. The open source “Lab Recorder” application was used to generate the session extensible data format

(XDF) file with the synchronized LSL streams from both, the EEG system and the Unity framework, containing brain activity and cognitive task events respectively.

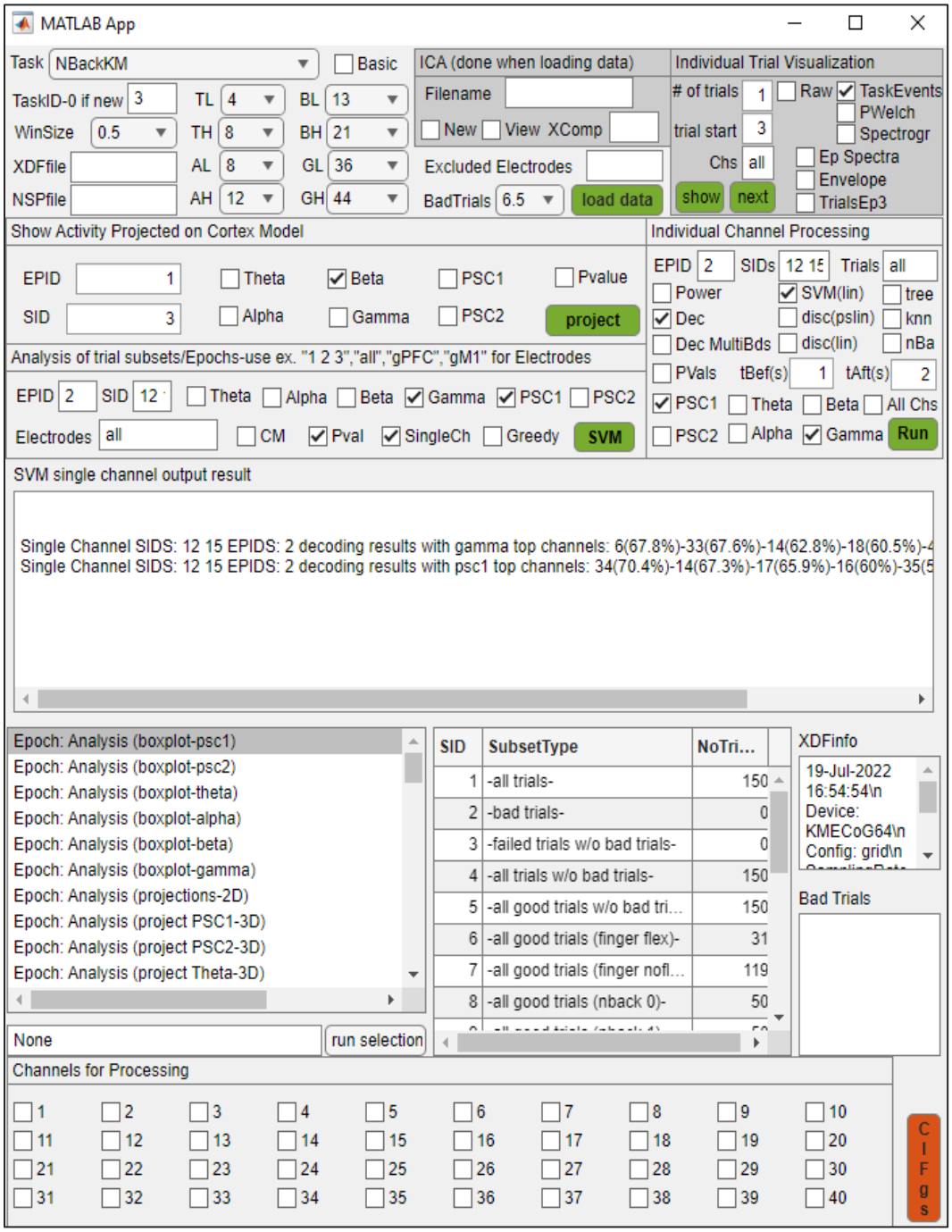

Figure 21. NCC Application – User Interface.

4.4 NCCapp: Session Loading and Preprocessing

The NCC application, depicted in Figure 21, was coded using Matlab and designed to facilitate the flexible exploration of recording sessions offline. Through the analysis of features synchronized with task events for selected sets of trials, it is possible to identify the brain regions involved with the specific cognitive demands of the tasks.

Prior to loading a recorded session, it is necessary to initialize the critical analysis parameters using the NCCapp user interface (UI). The mandatory settings include:

(1) Task: Cognitive task options include VisualSpatial, DelayedSaccade, NBack.

(2) TaskID: If set to 0, the XDF and NSP filename options in the UI will be employed. Alternatively, if a specific task ID is provided, the pre-recorded filenames in the task info file linked to this task and task ID will be processed.

(3) WinSize: Window Size for processing (typically 0.5 sec).

(4) TL/TH (Theta Low/High), AL/AH (Alpha Low/High), BL/BH (Beta Low/High), GL/GH (Gamma Low/High): frequency band ranges (low and high frequencies).

(5) BadTrials: Threshold to exclude trials. A trial will be marked as 'bad' if the standard deviation (STD) of a task epoch band power exceeds this threshold.

(6) ICA (Optional): Independent Component Analysis (ICA) parameters. This analysis utilizes and integrates tools from the open-source EEGLAB toolbox (Delorme A and Makeig S, 2004). Individual components can be viewed and then selected to be excluded from the regenerated signal to remove artifacts such as those associated with movements.

   i. Filename: New or saved ICA components file associated with this session.

   ii. New and View: Options to create a new and/or view the ICA components.

iii. XComp: Components to be excluded.

(7) Excluded Electrodes (Optional): Electrode numbers to be excluded from the analysis.

After specifying the parameters and options, pressing the "load data" button initiates the session loading and pre-processing. Depending on the session duration and the number of recorded electrodes, this may take several minutes.

The loading process incorporates pre-processing steps added to streamline analysis during session exploration. These steps include:

(1) Common average referencing for EEG or bipolar referencing for sEEG.

(2) Application of high-pass and notch filters (60 and 120 Hz).

(3) Computation of session baseline levels for each frequency band power.

(4) Categorization of trials and the formation of subsets of trials depending on the trial types and results.

(5) Assessment of the averaged band power for each task epoch and subset of trials.

(6) Utilization of PCA on task epochs from all trials to evaluate the principal component vectors and to extract the PSC1, PSC2 features for each epoch and their averaged level of each trial subsets.

Once loaded, information regarding the session, including the date, task epochs, and the count of successful trials for each subset, is displayed in the UI's output windows for Bad Trials, XDF info, and SID (Subset IDs). The session is then ready for exploration.

4.5 NCC Application: Cognitive Activity Exploration

The user interface offers multiple analysis options and can generate many visualization outputs to help determine the electrode's involvement associated with the cognitive factors of a selected task. Visualization options include but are not limited to:

- raw field potentials activity and associated task events for an individual or a group of trials,
- Hilbert envelope, spectrum or spectrogram for an individual trial or averaged trials at or around pre-defined task epochs,
- boxplot and p-values comparing electrode activity between epochs or between subsets of trials associated with a class,
- cortex topography of electrode activity for task epochs and for trials associated with a pre-determined class,
- frequency band power, statistical analysis, and machine learning decoding between epochs and/or between subsets using moving windows, and
- single channel decoding, greedy analysis and SVM confusion matrix between epochs or subsets of trials.

4.6 Cognitive Activity Mapping Results

EEG activity of volunteers was recorded as they completed multiple trials of the previously described cognitive tasks. The processing tools and recording pipeline underwent testing with the EEG signals and associated task events. The following subsections will present some of the results obtained from these testing sessions. During the NBack and Visual Attention tasks, the participants wore a 32 electrodes cap from Electro-Cap International (Figure 22C) for EEG recording. The

signals from the electrodes (Figures 22A, D) were amplified using the g.USBAMP (depicted in Figure 22B) and subsequently streamed via LSL to an XDF file, synchronized with the corresponding Unity stream containing the task events. Note that a mastoid electrode was used as the reference and the electrode in the AFz position was used as the ground.

A

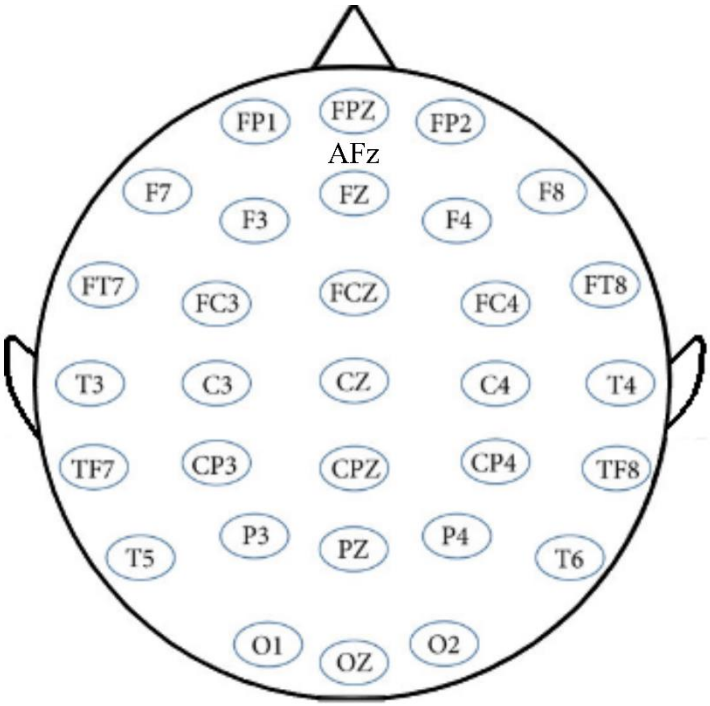

B

C

D

Electrode #	1	2	3	4	5	6	7	8	9	10	11	12	13	14	15	16
Label	FP1	F3	C3	P3	O1	F7	T3	T5	Fz	FCz	CP3	FC3	TP7	FPz	FT7	FP2
Electrode #	17	18	19	20	21	22	23	24	25	26	27	28	29	30	31	
Label	F4	C4	P4	O2	F8	T4	T6	Cz	Pz	CPz	CP4	FC4	TP8	Oz	FT8	

Figure 22. EEG g.tec Recording System. (A) shows the location of EEG electrodes recorded during the NBack and Visual Attention sessions. (B) depicts the EEG system g.USBAMP amplifier used during the testing sessions (note that 2 amplifiers were required for 31 electrodes). (C) illustrates the Electro-Cap International, gel-based EEG cap used for the testing sessions. (D) tabulates the electrode number along with the corresponding electrode label associations.

4.6.1 Working Memory: NBack Task

Introduced in 1958 by Wayne Kirchner (Kirchner, 1958), the NBack task is commonly employed in the research community to evaluate working memory activity such as memory load, encoding, retrieval, maintenance, and working memory manipulation. This task was implemented using single-digit numbers (1 to 4) and could be set to different levels of difficulty including 1-Back, 2-Back or the more challenging 3-Back.

In our implementation (Figure 23), the task starts after the participant fixates on the white sphere in the middle of the screen for at least 0.8 sec. The task initially shows the starting sequence of numbers depending on the set level of difficulty (1, 2 or 3 for NBack1, NBack2 and NBack3 respectively). The participant continues fixating until the next cue is shown. If this cue matches the memorized one, the participant initiates a saccade to the green check mark, otherwise in non-matching trials, participant saccade to the red X object.

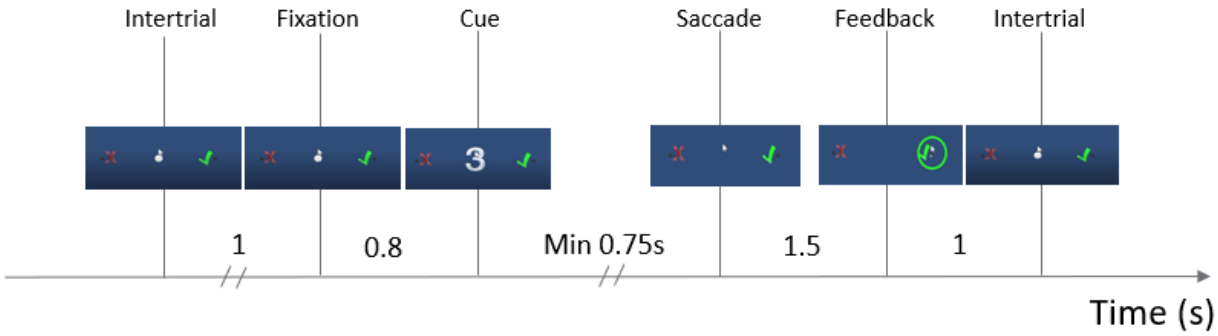

Figure 23. NBack Task. Experiment description and timing.

4.6.2 NBack2 Task Analysis (g.tec EEG)

In the pursuit of creating effective signal processing tools to investigate brain activity associated with cognitive functions, volunteers were asked to engage in the NBack task while their brain

activity was recorded using the g.tec EEG system. Presented results are shown for two females,

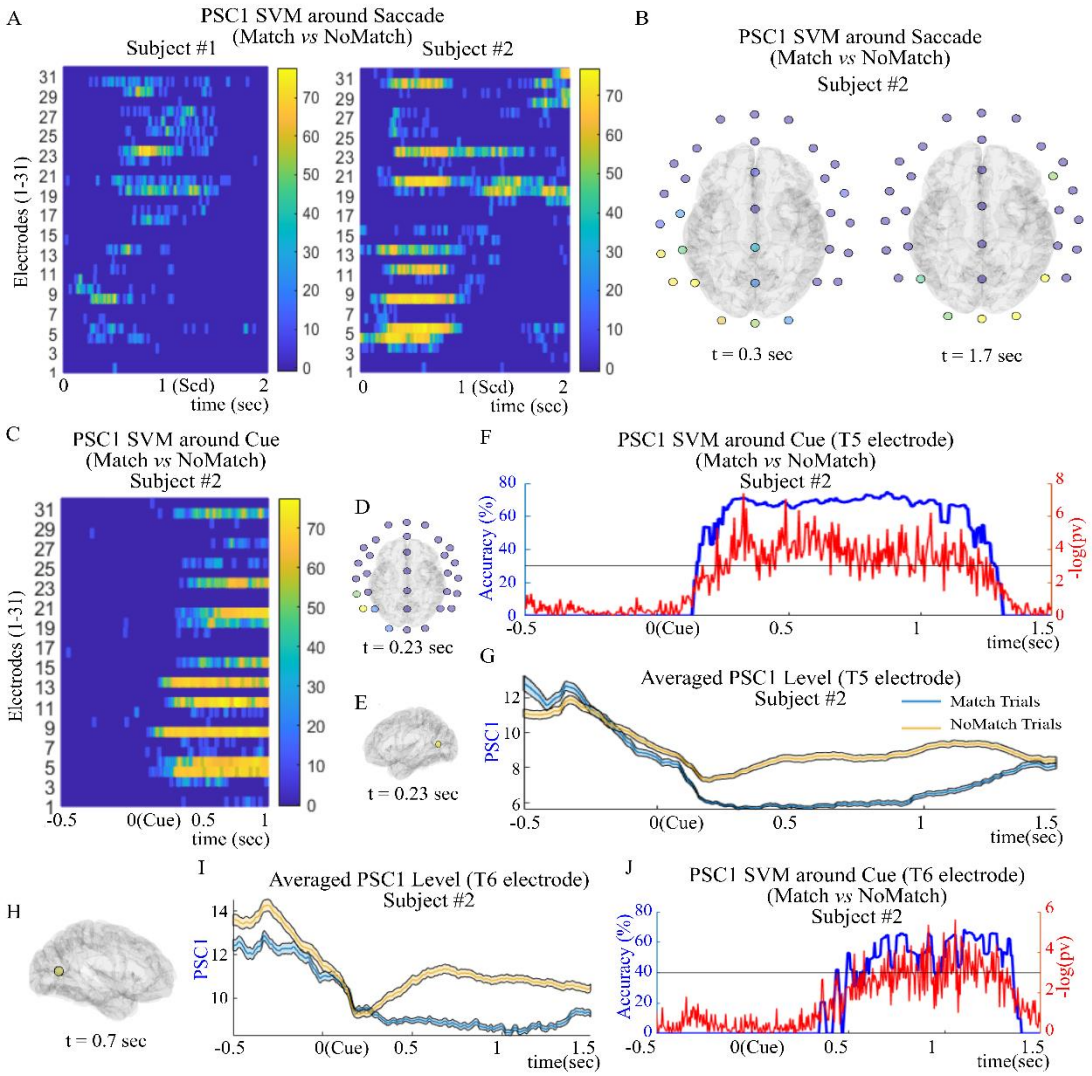

Figure 24. NBack2 Task – Analysis Results. (A) shows the PSC1 feature based SVM classification accuracy of Match *vs* NoMatch trials over time from individual electrodes for subject #1 (left panel) and subject #2 (right panel). (B) illustrates the electrode classification accuracy of Match vs NoMatch trials 0.7 sec before the saccade (left) and 0.7 sec after the saccade (right). (C) shows the PSC1 feature based SVM classification accuracy of Match vs NoMatch trials around the Cue onset. (D) illustrates the SVM (PSC1) classification accuracy 0.23 sec after Cue onset. (E) shows the location of T5 electrode. (F) displays the PSC1 classification accuracy for T5 electrode between Match vs NoMatch trials (blue) and the statistical significance (red, where the horizontal line is p-value = 0.001). (G) shows the Match and NoMatch successful trials averaged PSC1 level over time for T5 electrode. (H) shows the location of T6 electrode. (I) illustrates the Match and NoMatch successful trials averaged PSC1 level over time for T6 electrode. (J) displays the PSC1 classification accuracy for T6 electrode between Match vs NoMatch trials (blue) and the statistical significance (red, where the horizontal line is p-value = 0.001).

subject #1 and subject #2 aged 24 and 50 years old respectively.

Subject #1-#2 performed a total of 37-17 successful Match trials and 131-59 NoMatch trials respectively. Results illustrated in Figure 24 provide a sample of the analysis done from this experiment. In this task (NBack2), the classification of match versus no match trials identifies activities associated with decision making, movement planning, saccade, and working memory functions. Figure 24A shows the SVM classification of successful match vs no match trials using the PSC1 feature for Subject #1 (left) and Subject #2 (right) over time around the saccade onset. Note that the saccade onset epoch is the 0.5 sec window starting 1.5 sec before the feedback is provided. The findings show that numerous electrodes capable of discriminating between Match and NoMatch trials using the PSC1 feature are consistent across both subjects, with the modulation time being shorter for Subject #1 compared to Subject #2. Images of this classification for subject #2, captured 0.7 sec before (Figure 24B - left) and 0.7 sec after the saccade (Figure 24 - right), illustrate the positions of the active EEG electrodes. Initially, the activity reached its peak in the left hemisphere, around the T5 electrode location, before generating some activity in the right hemisphere. This pattern could be attributed to the engagement of brain areas associated with language in the left hemisphere during the task, possibly to repeat the memorized sequence.

At the cue onset, possible cognitive functions involved include cue processing, cue encoding, and working memory processes such as past cue retrieval. Note that the cue onset epoch (time=0 for Figures 24C-J) refers to the 0.5 sec epoch window centered 0.3 sec after the cue onset. For many of the electrodes active around the saccade onset, the decoder could successfully classify match vs no match trials (Figure 24C).

Utilizing PSC1 data captured from the T5 electrode enabled the successful classification of 70% of match *vs* no match trials using the window spanning from 0.28 to 0.78 sec after cue onset. The SVM classification accuracy (depicted in Figure 24F – blue) and the statistical significance (illustrated in Figure 24F – red) between match and no match trials reveal a sustained modulation following cue onset. Figure 24G illustrates the average PSC1 level over time for match (blue) and no match (yellow) trials. Interestingly, the T6 electrode, which is the right hemisphere counterpart to the T5 electrode, displayed modulation around 0.25 sec after the activity observed at the T5 electrode (Figures 24 H-J).

4.6.3 Covert Attention: Visual Spatial Attention

The visual attention task was designed to explore the neural activity associated with both covert visual attention and decision-making processes. Covert visual attention involves the capacity to attend to stimuli within a specific area of the visual field without overtly shifting the focus to that area. During such tasks, recording from MEAs in macaques' lateral prefrontal cortex showed high levels of field potentials activity in frequencies larger than 60Hz (Tremblay et al. 2015).

For this experiment (Figure 25), the participant begins by fixating on the central white sphere of the screen for a minimum of 1 sec. Subsequently, a cue appears briefly in one of four possible locations, followed by the presentation of four identical red spheres with black stripes. The participant is expected to maintain gaze at the center of the screen while covertly directing attention to the cued location. If the attended sphere undergoes a rotational movement, the participant executes a saccade toward the cued location (on the black sphere adjacent to the cued target). If any of the other spheres move, the participant is instructed to continue focusing on the center of the screen until feedback (a colorful ring around the cued target) is provided.

4.6.4 Session Visual Spatial Task (g.tec EEG)

As with the NBack analysis, the brain activity of participants was recorded using the g.tec EEG system as they engaged in the visual spatial attention task. Subject #1 completed a total of 22 successful saccade and 25 distractor trials, while subject #2 completed a total of 15 successful saccade and 16 distractor trials.

We first investigated the averaged beta power (normalized per electrode) around the saccade epoch for both saccade and distractor trials. It is important to highlight that the saccade onset epoch corresponds to the 0.5 sec window starting 1.25 sec before the feedback is provided. As shown in Figure 26A for subject #2, a clear beta desynchronization is noticeable for the saccade trials at the saccade epoch, followed by a synchronization period that includes all electrodes except for the frontal electrodes (FP2, FPz and F4). The difference seen for the frontal electrodes may be related to the removal of artifacts using ICA during the pre-processing steps. Predictably, this desynchronization/synchronization phenomenon is absent during the distractor trials, as the participant continued fixating until feedback was provided (Figure 26B).

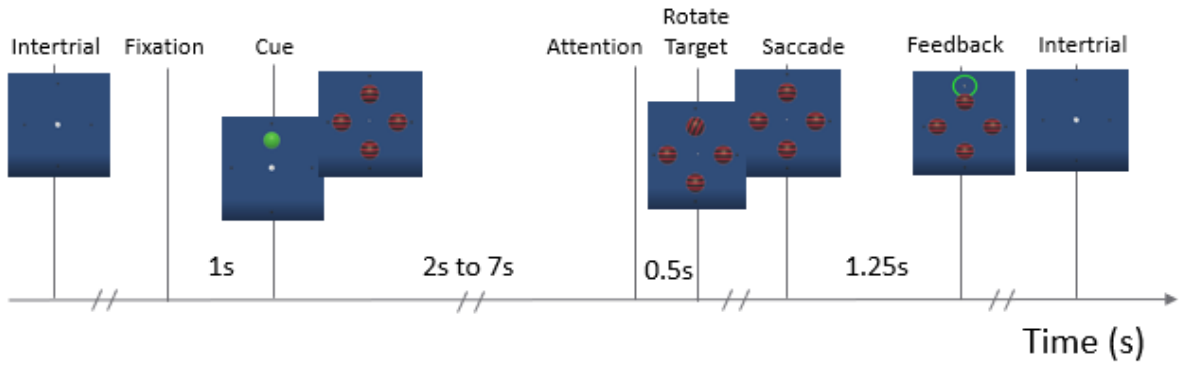

Figure 25. Visual Spatial Attention Task. Experiment description and timing.

The trials were then aligned with the feedback onset to investigate the SVM classification accuracy between saccade and distractor trials over time around the saccade epoch (1.25 sec before feedback). Notably, electrode Cz was able to classify with over 70% accuracy between saccade

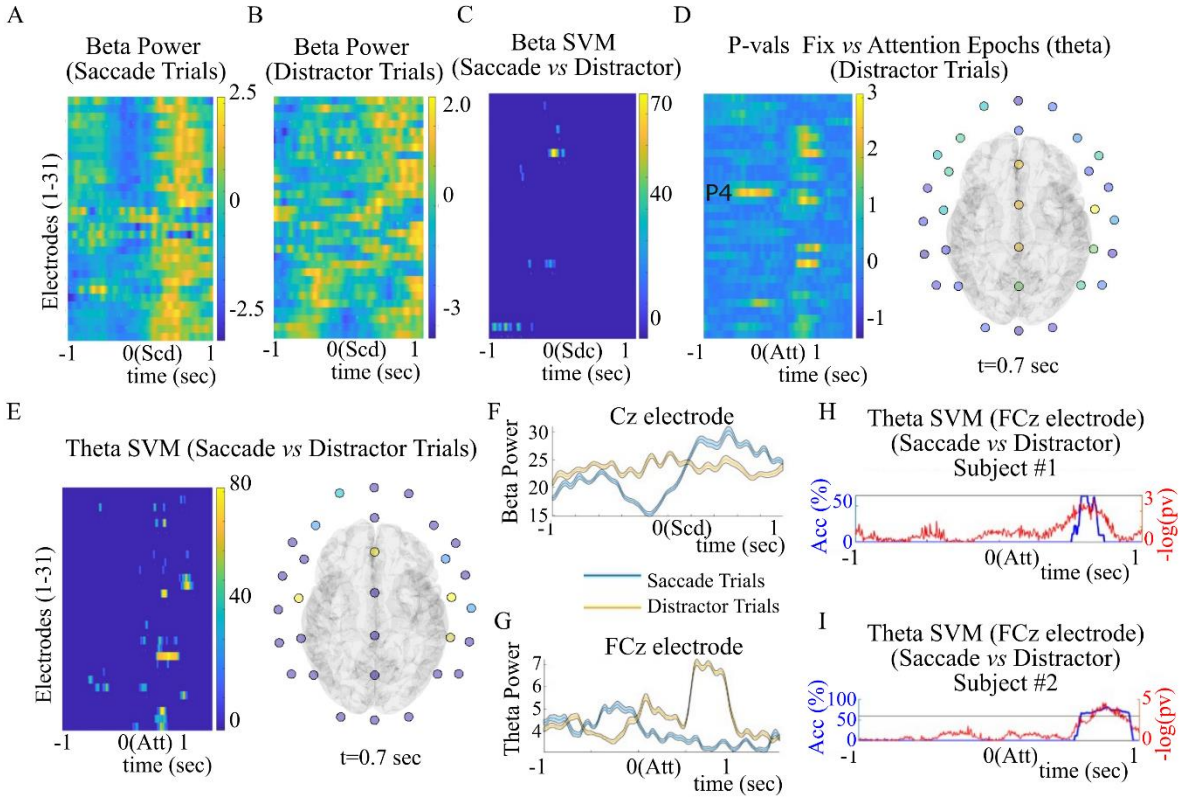

Figure 26. Visual Spatial Attention Task - Analysis Results. Averaged beta power of all successful saccade (A) and distractor (B) trials, norrmalized per electrode over time around the saccade (Scd). (C) shows the beta feature based SVM classification accuracy of saccade *vs* distractor trials over time from individual electrodes. (D-left panel) shows the statistical difference (-log10(p-values)) of theta between fixation and around the attention (Att) epochs (0.5 sec before target is rotated) for the distractor trials, (D-right panel) displays the EEG electrodes statistical results 0.7 sec after Att which is 0.2 sec after the target is rotated. (E-left panel) shows the classification accuracy of saccade *vs* distractor trials around the Att epoch, (E-right panel) represents the EEG classification 0.2 sec after the target is rotated. (F) shows the averaged beta power fluctuations over time for saccade and distractor trials on the Cz electrode. (G) shows the averaged theta power fluctuations over time for saccade and distractor trials on the FCz electrode. (H) and (I) show the classification accuracy (Acc) between saccade and distractor trials (blue) and the statistical difference (red, where the horizontal line is p-value = 0.001) for FCz on subject 1 (H) and subject 2 (I).

and distractor trials (figure 26C). Figure 26F illustrates the beta power modulation for the saccade trials (blue) and the distractor trials (yellow).

In every trial, when the target or a distractor target moves, the subject must decide on the next action to take. If the cued target moves, the participant initiates a saccade to that location, if it is a distractor target, the subject continues fixating. Aligning all trials with the target movement, which is referred to as the attention epoch, we then examined the statistical differences between a fixating epoch (fixation window before the cue epoch) and the epoch around the time the distractor target is set in motion. This analysis aimed to identify the electrodes involved with processing the target movement and the associated decision-making process. As shown in figure 24D (left), electrode P4, possibly involved with the processing of the stimulus, is the first to show statistical differences once the target moves. Several electrodes show statistical differences between these epochs 0.7 sec after the distraction occurs (as depicted in figure 26D - right), including the midline electrodes often associated with go and no-go cognitive activity (Brier et al. 2010).

The SVM classification of saccade *vs* distractor trials using theta activity around the attention epoch revealed a subset of electrodes capable of classifying the trials, achieving up to 80% accuracy 0.7 sec after the attention epoch (Figure 26E - right). In Figure 26G, the averaged theta power modulation of one of those electrodes (FCz) is presented for both the saccade trials (blue) and the distractor trials (yellow). Figures 26H-I illustrate the theta SVM classification accuracy and statistical variances between saccade and distractor trials around the attention epoch for two subjects. These figures highlight a consistent pattern of discriminatory activity for both subjects during this important epoch of the task.

4.6.5 Saccade Intention: Delayed Saccade Task

In this simple task, participants perform a saccade to one of four possible target locations. This task engages brain activity associated with vision, saccade intention, preparation and execution, and also working memory. Results may also be used as baselines for other tasks where saccade related activity should be disregarded.

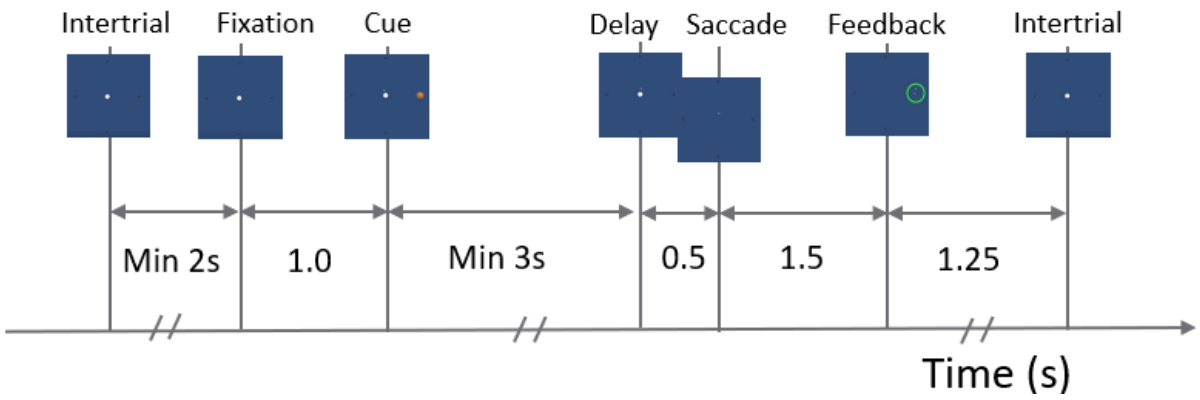

Figure 27. Delayed Saccade Task. Experiment description and timing.

As shown in Figure 27, the task starts with subjects fixating on a white sphere in the center of the screen (minimum of 1 sec) followed by the trial saccade cue location being shown for a period of 0.75 sec. The minimum duration of the following delay period is set for 3.5 sec and is interrupted by the white sphere disappearing which cues the participant to initiate a saccade to the memorized location and fixate to that position until feedback is provided. The following trial then starts 1.5 sec after the feedback is provided.

4.6.6 Delayed Saccade Task (sEEG)

In our ongoing efforts to develop a signal processing methodology for investigating EEG fluctuations associated with cognitive activity, we conducted evaluation sessions at the Epilepsy Monitoring Unit of Western University. In this joint effort, my role was to integrate the Unity

framework with their infrastructure and provide guidance on running the cognitive tasks. The research collaborators at Western (Mohamad Abbass and Greydon Gilmore) conducted the recording sessions with cooperative subjects who had previously undergone sEEG lead implantation. The sessions took place while the subjects were being monitored for seizure activity. Subsequently, the relevant data for this session was shared, including the task events (labstreaming layer: XDF file), the field potentials (EDF file) as well as the preprocessed sEEG electrode locations and their respective atlas label. My task involved synchronizing the brain activity and task events by utilizing annotation timestamps and associated timestamps within a Matlab XDF stream, both triggered by a single key press. Following this alignment, the previously described tool set was employed to analyze the session and identify contact points implicated in the task.

For the methodology assessment, an analysis was performed on a recorded session with one subject engaged in the delayed saccade task. This session included 13, 16, 13, and 11 successful right, up, left, and down saccade trials respectively. The epilepsy monitoring unit team meticulously documented the locations of electrode contacts (totaling 120 contacts) throughout the brain, illustrated in Figures 28A-B.

Following the pre-processing steps outlined in section 4.4, we explored the average power (normalized per electrode) around the cue epoch for trials involving left and right targets. Note that the cue onset epoch (time=0 for figures 28C-J) refers to the 0.5 sec epoch window centered 0.3 sec after the cue onset. Figures 28C-D depict a consistent pattern around the cue in left trials, displaying more synchronization across all electrodes compared to the right trials. This phenomenon might be attributed to the subject's preparatory activity, anticipating a specific cue location, and adjusting to the presented cue location. Notably, alpha activity in the right

hemisphere rapidly decreases after cue presentation in the left trials, as illustrated in Figure 28E.

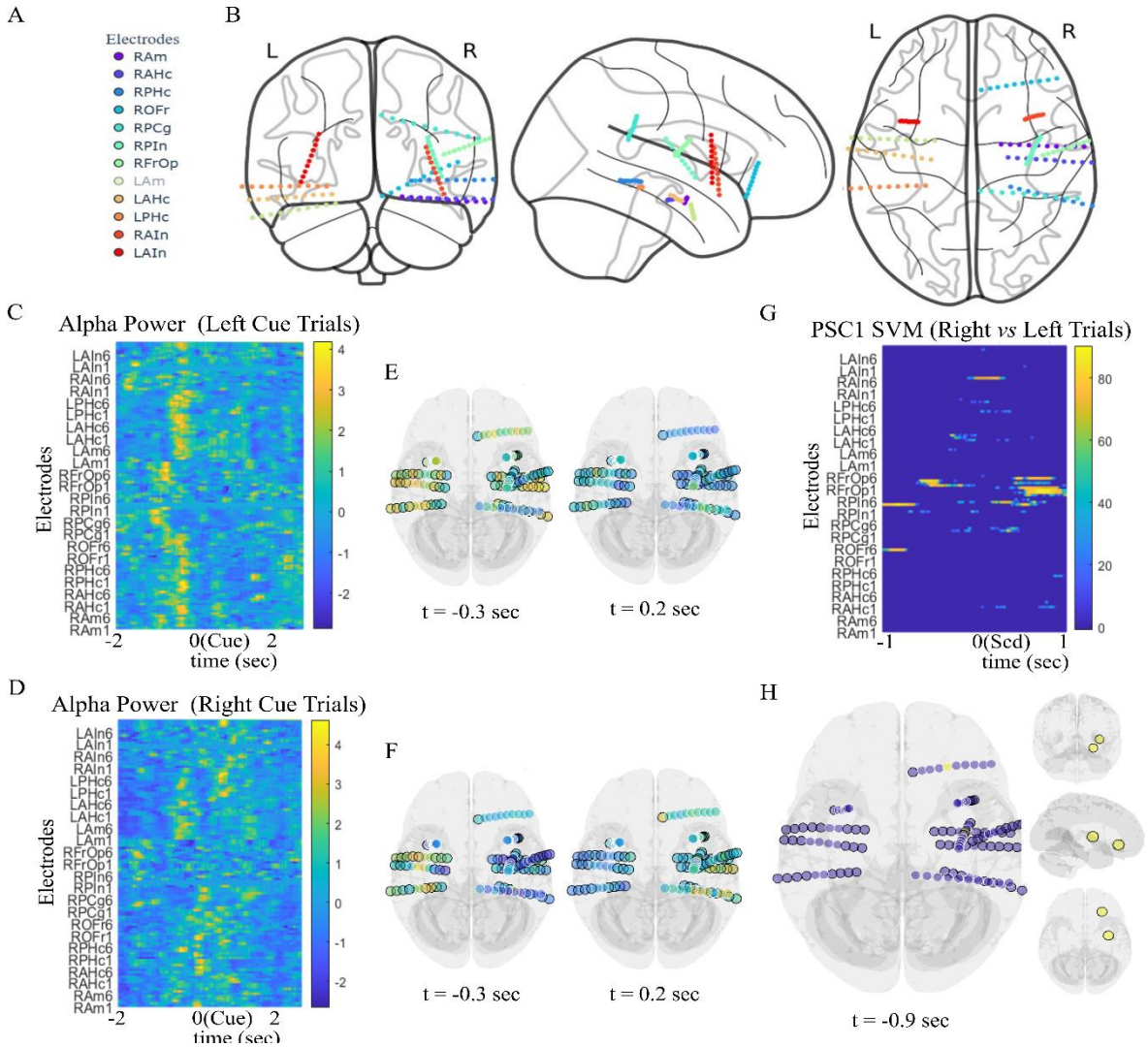

Figure 28. Delayed Saccade Task - Analysis Results. (A) shows the sEEG leads deepest contact point location (RAm: Right Amigdala, RAHc: Right Anterior Hippocampus, RPHc: Right Posterior Hippocampus, ROFr: Right Orbitofrontal, RPCg: Right Posterior Cingulate, RPIn, Right Posterior Insula, RFrOp: Right Frontal Operculum, LAm: Left Amigdala, LAHc: Left Anterior Hippocampus, LPHc: Left Posterior Hippocampus, RAIn: Right Anterior Insula, LAIn: Left Anterior Insula). (B) depicts the trajectory of the electrodes in the brain. Averaged alpha power of all successful left cue (C) and right cue (D) trials, normalized per electrode over time around the cue (Cue). (E)-(F) displays the EEG electrodes' alpha power at 0.3 sec before (left panel) and 0.2 sec after the Cue Epoch for the left (E) and the right (F) trials. (G) shows the PSC1 classification accuracy of right *vs* left trials around the saccade (Scd) epoch. (H) depicts the classification accuracy of left vs right trials 0.9 sec before the saccade epoch for all electrodes (left panel) and for electrodes RPIn5 (5^{th} contact on the Right Posterior Insula electrode) and ROFr5 (5^{th} contact on the Right Orbitofrontal electrode).

A comparable effect on alpha activity during right trials is observed in the left hemisphere (Figure 28F). This aligns with existing literature reporting alpha desynchronization on the contralateral side of the visual cue (Rihs et al. 2007).

We then aligned the trials with the saccade onset and looked at the SVM classification accuracy between left and right trials. Note that for this task, the saccade onset epoch is the 0.5 sec window starting 1.5 sec before the feedback is provided. Figure 28G displays the accuracy outcome over time for all electrodes around the saccade epoch. Two electrodes exhibited the capability to classify between left and right targets up to one second before the onset of the saccade, suggesting potential involvement in saccade planning activity or memory functions. These electrodes were positioned in the posterior insula and the precentral/prefrontal cortex region of the right hemisphere (Figure 28H). While the insula is traditionally associated with sensory and emotional processing, studies (Laurent et al. 1996, Cheng et al. 2013, Menon and Uddin, 2010) have indicated its modulation during saccade planning and broader cognitive processes. The discovery of the precentral electrode's involvement also aligns with findings by Goldman-Rakic (1995), indicating that neurons in the prefrontal cortex exhibit modulation during the delay period of delayed-response trials, suggesting a potential connection to short-term memory functions.

4.7 Conclusions

Mapping cognitive functions to specific anatomical locations can be instrumental in preparing for BCI implantation. The methodology presented herein demonstrates the potential to employ a tailored set of cognitive tasks and signal processing tools to trigger and investigate field potential activity associated with memory, attention, and saccade planning functions. The versatility of the

toolset allows for processing brain signals from various electrode types, including ECoG, EEG, sEEG, and MEA electrodes.

The results highlight significant differences between subjects posing a challenge in generalizing locations and common activities linked to specific cognitive functions. This variability may be caused by diverse cognitive strategies used by different subjects or true physiological variability, underscoring the importance of considering individualized factors when selecting an implant location. Please note that the presented results aim to showcase the capabilities of the signal processing and exploration tools. The number of recording sessions is insufficient to draw meaningful conclusions on markers of cognitive activity from these results.

To improve the proposed method, future refinements could involve tailoring or adding new cognitive tasks, and correlating results from different tasks for each subject, thereby identifying unique activity patterns per individual. This personalized approach holds the potential to yield more informative signals for deciphering the intentions of BCI users.

4.8 References

[1] Brignani D, Maioli C, Maria Rossini P, Miniussi C. Event-related power modulations of brain activity preceding visually guided saccades. Brain Research. 2007;1136(1):122–31.

[2] Brier MR, Ferree TC, Maguire MJ, Moore P, Spence J, Tillman GD, et al. Frontal theta and alpha power and coherence changes are modulated by semantic complexity in Go/NoGo tasks. International Journal of Psychophysiology [Internet]. 2010;78(3):215–24.

[3] Chang LJ, Yarkoni T, Khaw MW, Sanfey AG. Decoding the role of the insula in human cognition: Functional parcellation and large-scale reverse inference. Cerebral Cortex. 2013;23(3):739–49.

[4] Delorme A & Makeig S. EEGLAB: an open-source toolbox for analysis of single-trial EEG dynamics. Journal of Neuroscience Methods. 2004;134:9-21.

[5] Goldman-Rakic PS. Cellular basis of working memory. Neuron. 1995;14(3):477–85.

[6] Kirchner WK. AGE DIFFERENCES IN SHORT-TERM RETENTION OF RAPIDLY CHANGING INFORMATION Minnesota Mining and Manufacturing Company. Journal of Experimental Psychology. 1958;55(4):352–8.

[7] Menon V, Uddin L. Saliency, switching, attention and control: a network model of insula function. Brain Structure Funct. 2010;214(5–6):655–67.

[8] Petit L, Orssaud C, Tzourio N, Crivello F, Berthoz A, Mazoyer B. Functional anatomy of a prelearned sequence of horizontal saccades in humans. Journal of Neuroscience. 1996;16(11):3714–26.

[9] Rihs TA, Michel CM, Thut G. Mechanisms of selective inhibition in visual spatial attention are indexed by α-band EEG synchronization. European Journal of Neuroscience. 2007;25(2):603–10.

[10] Stam CJ, Van Cappellen Van Walsum AM, Micheloyannis S. Variability of EEG synchronization during a working memory task in healthy subjects. International Journal of Psychophysiology. 2002;46(1):53–66.

Chapter 5

Mapping Cognitive Activity from Electrocorticography Local Field Potentials in Humans Performing NBack Tasks

5.1 Abstract

Advancements in data science and assistive technologies have made invasive brain-computer interfaces (iBCIs) increasingly viable for enhancing the quality of life in physically disabled individuals. Intracortical micro-electrode implants are a common choice for such a communication system due to their fine temporal and spatial resolution. The small size of these implants makes the implantation plan critical for the successful exfiltration of information, particularly when targeting representations of task goals that lack robust anatomical correlates. Working memory processes including encoding, retrieval, and maintenance are observed in many areas of the brain. Using human electrocorticography recordings during a working memory experiment, we were able to localize cognitive activity associated with the task and to identify key locations involved with executive memory functions. From the analysis, we could propose an optimal iBCI implant location with the desired features. The general approach is not limited to working memory but could also be used to map other goal-encoding factors such as movement intentions, decision-making, and visual-spatial attention.

5.2 Introduction

Conditions that restrict mobility and/or communication can profoundly impact those who experience them. Brain-computer interfaces (BCIs) hold promise in restoring some of the lost functions through augmented communication (Willett et al. 2021, Santhanam et al. 2006,

Pandarinath et al. 2017), and improved mobility (Ajiboye et al. 2017, Collinger et al. 2013). By offering direct control of assistive devices (Al-qaysi et al. 2018, Flint et al. 2012, Benabid et al. 2019), this technology can enhance autonomy thus leading to an overall improved quality of life. Current intracortical BCIs predominantly capture and analyze the electrical signals from the sensorimotor cortex activated during movement intentions. Recent studies have explored generating action commands based on the user's goal or desired outcome (Andersen et al. 2019, Shanechi et al. 2013), resulting in a more natural and intuitive control of assistive technologies.

The objective of an iBCI user, such as an intended movement, object, or spatial location, can be decoded from neuronal activity in various regions of the brain, including parietal (Andersen and Cui 2009, Gold and Shadlen 2007), premotor (Hosman et al. 2021), and prefrontal cortices (Johnston et al. 2021, Tremblay et al. 2015, Mendoza-Halliday and Martinez-Trujillo 2017, Miller et al. 1996). The prefrontal cortex, known for its highly interconnected nature, plays a crucial role in integrating task-relevant information during goal-directed behaviors. For example, Rouzitalab et al. (2023) showed the possibility of classifying different representations of newly learned arbitrary associations within the lateral prefrontal cortex (LPFC), a region which was previously deemed a suitable signal source for a goal selective cognitive BCI (Vansteensel et al. 2010, Boulay et al. 2016).

Local field potentials (LFPs), which are low-frequency signals recorded from electrodes placed in (micro-electrode array (MEA), stereo-electroencephalography (SEEG)) or near (Electroencephalography (EEG), Electrocorticography (ECoG)) the cortical and sub-cortical surfaces, reflect the collective activity of the surrounding population of neurons. Oscillatory signals, extracted from the LFPs and typically considered during the analysis of brain activity,

include theta (frequency range: 4-8Hz), alpha (frequency range: 8-12Hz), beta (frequency range: 12-24Hz) and gamma (frequency range: 30-100Hz). Additionally, another study suggested that broadband shifts in the LFP power spectra can be a good predictor of local neuronal spiking (Manning et al. 2009). The first component of the principal component analysis on the LFP spectra (PSC1) provides a broadband feature that shows a distinct representation of individual fingers (Miller et al. 2009).

Working memory refers to the ability to temporarily hold and manipulate a limited amount of information (Baddeley 1986). It includes encoding, retrieving, and maintaining information necessary to complete a task and has been shown to involve many areas of the brain (Smith and Jonides 1999). Research studies have shown an increase in gamma power observed in higher memory load during different phases of working memories (Lundqvist et al. 2016, Miller et al. 2018, Roux and Uhlhaas 2014) where the gamma increase could even predict the number of items maintained in working memory (Roux et al. 2012). As reported by Brzezicka et al. (2019), theta activity increases in the dorsal anterior cingulate cortex and hippocampus but decreases in the dorsolateral prefrontal cortex (dlPFC) for higher working memory loads, the latter changes being predictive of behavior in an individual trial. The NBack task is a widely utilized experiment to assess the impact of memory load and reflects neural activity linked to online monitoring, updating, and the manipulation of memorized information (Owen 1995).

Possible intracortical locations and their associated cognitive activity correlation should be thoroughly considered before the implantation of an iBCI device. In this setting, the goal is to localize the activity from subdural electrodes spanning a larger brain region compared to a micro-electrode array. Therefore, in this report, the contribution at the level of individual electrodes is

investigated. The methodological approach described in the following sections details algorithms to find the brain locations most involved with the demands of performing variations of the NBack memory tasks. For an iBCI system, the most beneficial information is timed with the executive functions, specifically when the information is retrieved, processed, and decisions are made. The methodology presented here allows the possibility of identifying the subdural ECoG electrode most involved during different phases of working memory, and thus be selected as the optimal iBCI implant location. This approach has the potential to extend its capability to pinpoint the site of various other cognitive activities such as movement intention and visual-spatial attention.

5.3 Methods

5.3.1 Experimental Setup

For this study, we analyzed intracortical EEG data from the human ECoG library provided by Stanford University (Miller 2019). "All patients participated in a purely voluntary manner after providing informed written consent, under experimental protocols approved by the Institutional Review Board of the University of Washington (#12193). The patient data were anonymized according to IRB protocol in accordance with the HIPAA mandate".

The subdural activity was recorded from 40-64 ECoG contacts on the right hemisphere of four subjects at a 1kHz sampling rate while they performed variations of an NBack task. For visualization purposes, this manuscript used a standardized brain "wholebrain.mat" provided by the "Localization on Cortex (LOC)" package (Miller et al. 2007). The Talairach coordinates on the standardized cortex template and associated Brodmann areas for subjects CA, CC, AL, and UG are shown in Figures 29A-29B, 29C-29D, 29E-29F, and 29G-29H respectively.

5.3.2 Behavioral Task

As shown in Figure 30A, all variations of the NBack task consisted of subjects looking at a house cue (Figure 30B) visible for 0.6 sec, followed by the removal of the cue triggering a physical response of hand flexing/unflexing if the cue matched the remembered house. The following cue

A

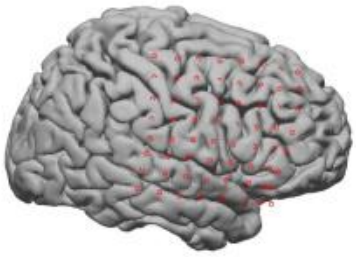

B

1	6	6	6	6	6	8	8
1	1	4	6	8	8	9	9
40	1	6	6	44	9	9	9
40	40	4	6	44	9	9	10
40	40	1	6	44	9	9	9
22	41	1	6	44	44	45	45
22	22	41	22	38	38	47	47
21	21	21	21	38	38	47	47

C

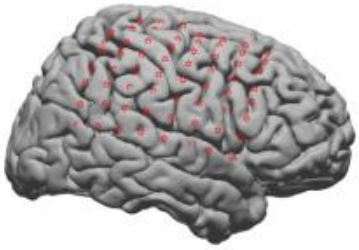

D

7	5	1	6	6	6	6	8
7	1	1	4	6	6	8	8
7	7	1	1	4	6	8	8
39	40	40	40	1	6	6	44
39	39	40	40	1	4	6	44
39	39	40	40	40	4	6	44
19	39	39	22	40	1	6	44
19	37	39	22	22	41	22	38

E

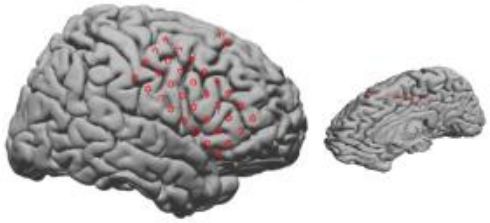

F

31	31	6	6	6	6	6	6
6	6	8	44	9	46	46	46
4	6	6	44	44	9	45	46
16	4	4	6	44	44	45	47
40	1	4	4	6	44	47	47

G

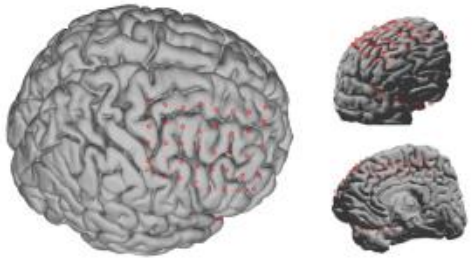

H

4	6	6	6	6	8	8	9
4	6	6	6	8	8	9	9
1	4	6	8	8	9	9	9
1	6	6	6	44	9	9	10
1	1	4	6	44	9	46	46
31	31	24	32	32	8	8	9
4	6	6	6	6	8	8	9
25	11	47	47	47	47		

Figure 29. Details of subjects' ECoG grids. (A), (C), (E), and (G) display a standardized brain with electrode locations superimposed using Talairach coordinates (Miller 2019) for subjects CA, CC, AL and UG, respectively. (B), (D), (F), and (H) list the Brodmann areas corresponding to each electrode location for subjects CA, CC, AL, and UG, respectively.

would then be presented 1.6 sec after the response initiation. The cued house could be one of 40 possible cues, with approximately 20% of the trials being a match trial.

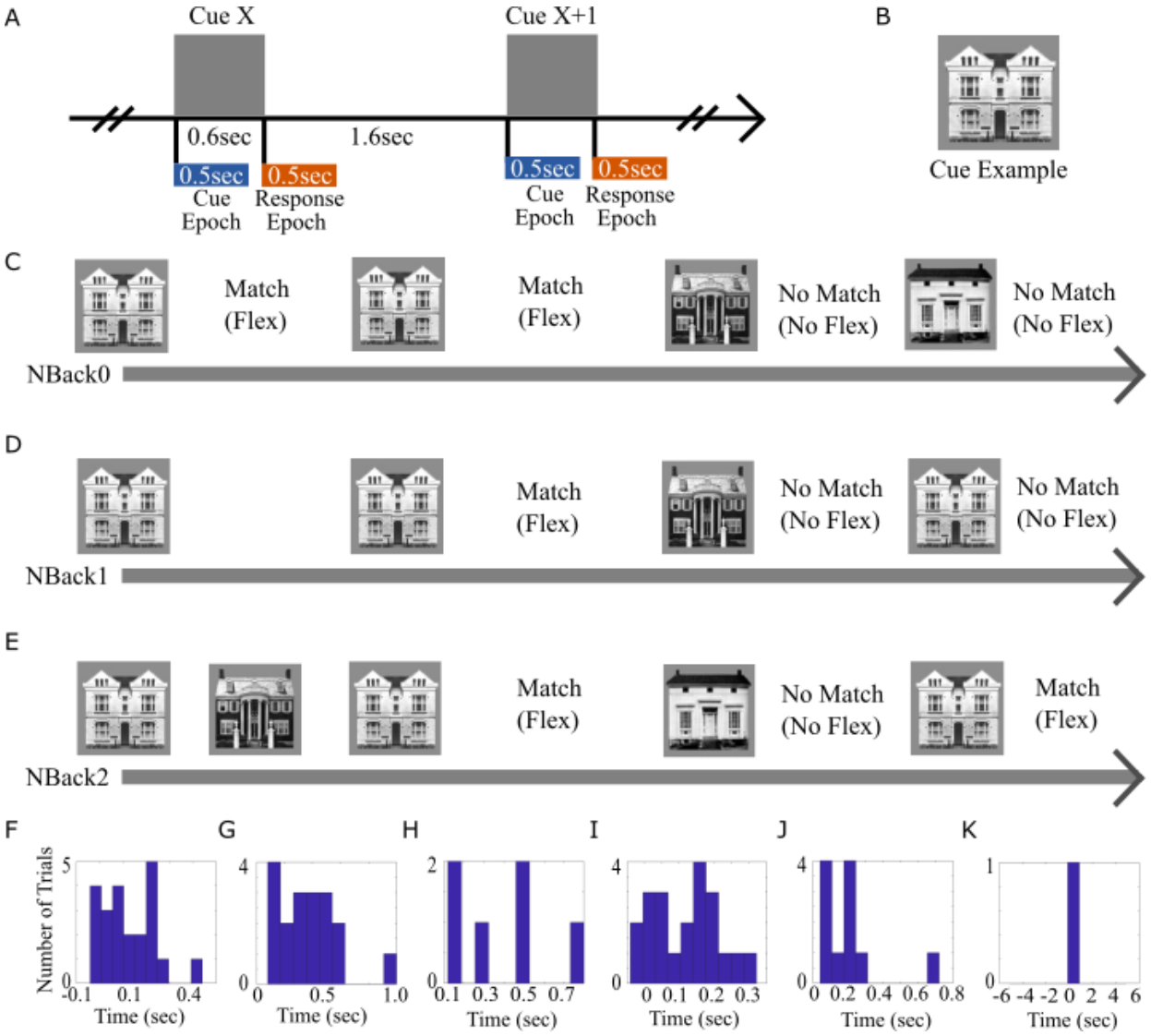

Figure 30. Task description. **(**A) depicts the experiment timing, the top row shows the visual information displayed to the subject during the task, the middle row shows the trial timing events, and the bottom row shows the analysis epochs. Note that the length of the analysis window is 0.5 sec. (B) show a cue example. (C)-(E) illustrates examples of trials showing expected behaviors which are a flex followed by an unflex of the hand for a matched house, and no movement for a house that does not match (NBack0 (C), NBack1 (D), and NBack2 (E)). (F)-(K) plots the histograms of movement delay relative to response event corresponding to the cue offset for subject CC (NBack0 (F), NBack1 (G), and NBack2 (H)) and for subject CA (NBack0 (I), NBack1 (J), and NBack2 (K)).

The subjects were recorded for blocks of trials set to one of three levels of difficulty (NBack0, NBack1, and NBack2). For subjects CA and CC, each block contained one hundred trials while for subjects AL and UG, 50 trials were tested per block. Since there was no recording of physical hand movement during the experiment for subjects AL and UG, all their trials were assumed to be successful. Based on the data glove recorded movement, histograms of movement delay from the cue offset for NBack0, NBack1, and NBack2 are shown in Figures 30F-30H for subject CA and Figures 30I-30K for subject CC respectively.

Table 10. Stanford University – NBack Subject and trials details (* Assuming all trials were successful since the flexing movement was not captured for this subject).

Subject (Sex)	Total Trials	Failed Trials	NBack0 Successful Trials		NBack1 Successful Trials		NBack2 Successful Trials	
			Match	No Match	Match	No Match	Match	No Match
CA(M)	300	20	22	77	18	79	6	78
CC (M)	300	29	21	78	11	80	1	80
AL (F)	150	0*	39	11	40	10	40	10
UG (F)	150	0*	39	11	40	10	40	10

For the simplest task (NBack0: Figure 30C), the subject was shown a picture of a house and was asked to memorize this cue before the start of the experiment. For the more difficult tasks, the subjects would have to remember the previously cued house (NBack1: Figure 30D), or the cued house one trial prior to the previously cued house (NBack2: Figure 30E). Note that for the NBack2 task, subject CC only selected a match once out of a hundred trials. This task was likely too difficult for this subject, who strategically chose to always assume no match trials. For that reason, the

NBack2 task results were disregarded for this subject. Table 10 shows the details of trials for each subject.

5.3.3 Neural data analysis

MATLAB was used for all data analysis. The data from each electrode was first referenced to its average and then re-referenced to the common grid average. Using a sixth-order Butterworth high pass filter, the frequencies lower than 3Hz were removed. The data were then filtered using two IIR notch filters (60Hz, 120Hz) to reduce the ambient noise. Windows of 0.5 sec were used to analyze the LFP-based activity.

Baseline. Moving average baselines for each frequency band were evaluated by using data recorded prior to the commencement of the first trial, gradually adapting throughout the experiment. Precisely, a buffer of 100 windows is established, each window initialized with the band power found in a 0.5 sec window before the onset of the first trial. A 0.5 sec moving window with a step of 0.5 sec throughout the experiment is then used to calculate a moving baseline for each channel. At every moving window step, the buffer undergoes a shift. The last window is updated with the band power from the moving window, and the first window is removed. The baseline for the duration of that window is established as the average of the entire pipeline.

Frequency band features. The presented analysis used Thomson's multitaper power spectral density estimate (Matlab function: pmtm) to first obtain the LFP spectrum of selected 0.5 sec windows. The averaged frequency band power for theta (4-8Hz), alpha (8-12Hz), beta (13-30Hz), and gamma (50-150Hz) were extracted from the spectrum (Matlab function: band power). Finally,

the theta, alpha, beta, and gamma baselines for each trial were subtracted from their respective averaged band powers to provide the window features used in this manuscript.

First Principal Spectral Component (PSC1) feature. This feature represents the broadband frequency activity (Miller et al. 2014) over a window size, set to 0.5 sec in this analysis. To calculate this feature (see Johnston et al. (2021) for details), the principal component analysis was performed on the normalized power spectrum of the LFP for all trials using three windows per trial (Intertrial: the window starting 0.5 sec before cue onset, Cue: the window starting when cue is presented, Response: the window starting when cue is removed). The electrode PSC1 feature of a 0.5 sec window is the result of projecting its original spectrum on the principal eigenvector for this electrode.

Moving Window: to evaluate the temporal evolution of band power, PSC1 level, statistical significance, and SVM classification accuracy, a 0.5 sec window was evaluated every 5 msec (99% overlap) from 1 sec before to 1.5 sec after the cue onset.

5.3.4 Statistics

The statistical significance between different sets of trials (p-value) was evaluated using the one-way ANOVA (Matlab function: anova1).

Support Vector Machine Classification. To classify the NBack difficulty level or the NBack Match/No Match trial type from neural activity, we used a support vector machine algorithm with a linear kernel (LIBLINEAR implementation for MATLAB (Fan et al. 2008), with options L2-regularized, L2-loss, and 5-fold cross-validation). This configuration provides a good balance between classification accuracy while keeping a low computational requirement (Johnston et al.

2021). The presented accuracies are the averages of repeating the SVM 5-fold classification 20 times. The SVM classification accuracies were only evaluated at the time when features for this

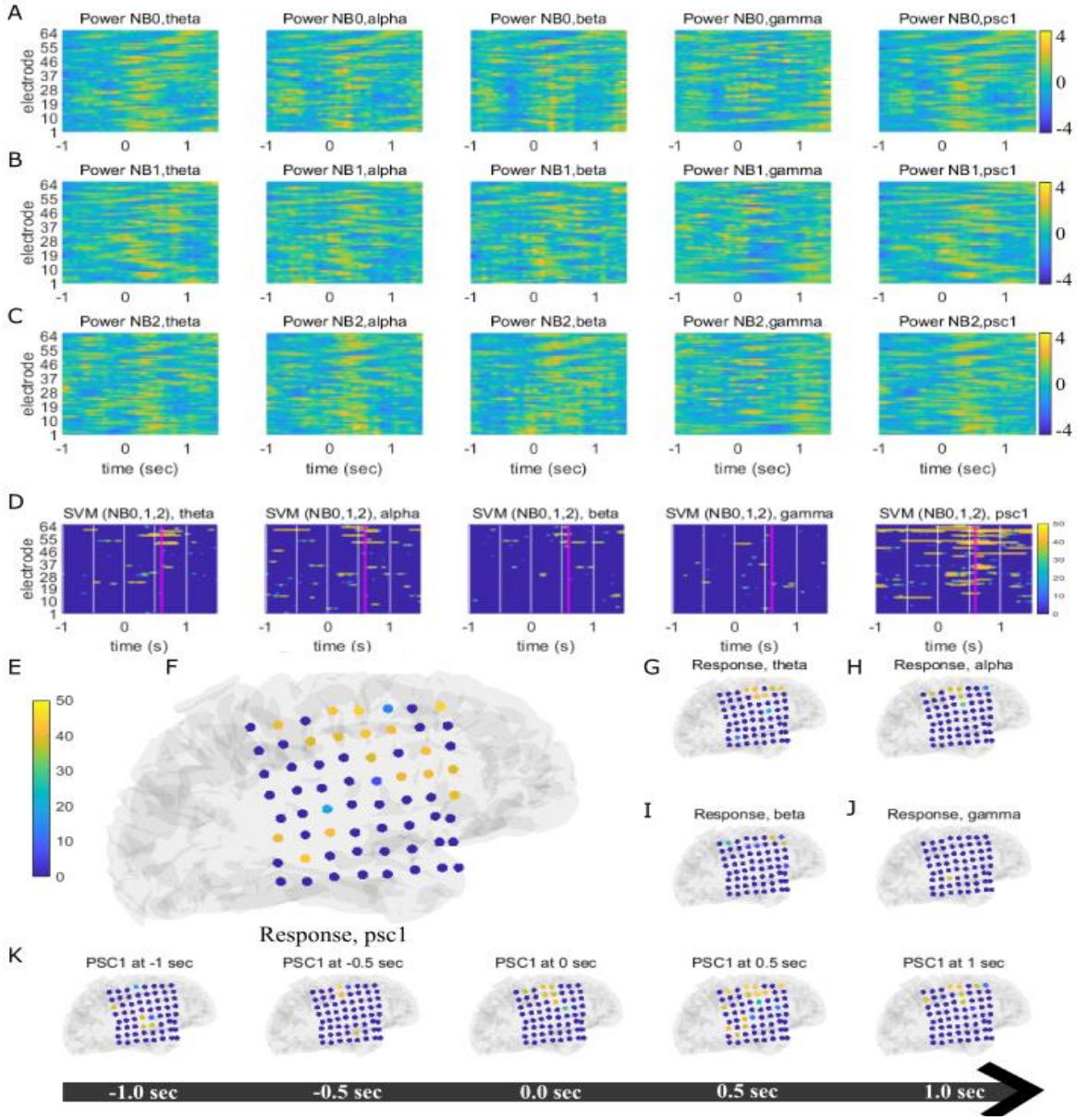

Figure 31 Subject CA - NBack task modality analysis. **(**A), (B), and (C) show the averaged power of all successful no match trials, normalized per electrode over time for theta, alpha, beta, gamma, and PSC1 for NBack0, NBack1, and NBack2 respectively. (D) shows the SVM classification accuracy of task difficulty over time (classes: NBack0, NBack1, NBack2) from individual electrodes for theta, alpha, beta, gamma, and PSC1. (E) displays the legend used for (D)-(K). The PSC1 (F), theta (G), alpha (H), beta (I), and gamma (J) classification accuracies are displayed on the cortex for the response time window (magenta vertical lines shown in (D)). (K) shows the PSC1 classification of task difficulty for each electrode on the cortex at times -1.0 sec, -0.5 sec, 0.0 sec, 0.5 sec, and 1.0 sec (white vertical lines shown in (D)).

window were significantly different (p-value < 0.01) and set to 0% otherwise.

5.4 Results

5.4.1 NBack Task Difficulty Analysis (subject CA)

The temporal evolutions per electrode of successfully completed no match trials for theta, alpha, beta, gamma, and PSC1 power levels were assessed, normalized per electrode over the period from 1 sec before to 1.5 sec after cue onset, and then graphically represented (NBack0: Figure 31A, NBack1: Figure 31B, NBack2: Figure 31C). The power level over time shows a similar pattern for many electrodes around the response time, with more interelectrode synchronization occurring as the task difficulty increases.

We then evaluated classification performance for each frequency band and PSC1 in determining the difficulty level of the NBack task over the trial duration, using the cue onset to align the successfully completed no match trials. For each moving window, we assessed the statistical differences between 3 classes (NBack0, NBack1, NBack2). If significant differences were found in this window (p-value < 0.01) the SVM classification accuracy was then evaluated otherwise, the accuracy was set to 0. Figure 31D shows the resulting statistical significance and classification accuracies over time for theta, alpha, beta, and gamma bands; and PSC1. The classification results, especially using the PSC1 feature, show many electrodes with significant differences depending on the task difficulty before and after the cue onset. This difference could be related to memory retention, or it could be influenced by stress or motor changes depending on cognitive requirements.

We further show the individual electrode classification accuracy during the response period on a

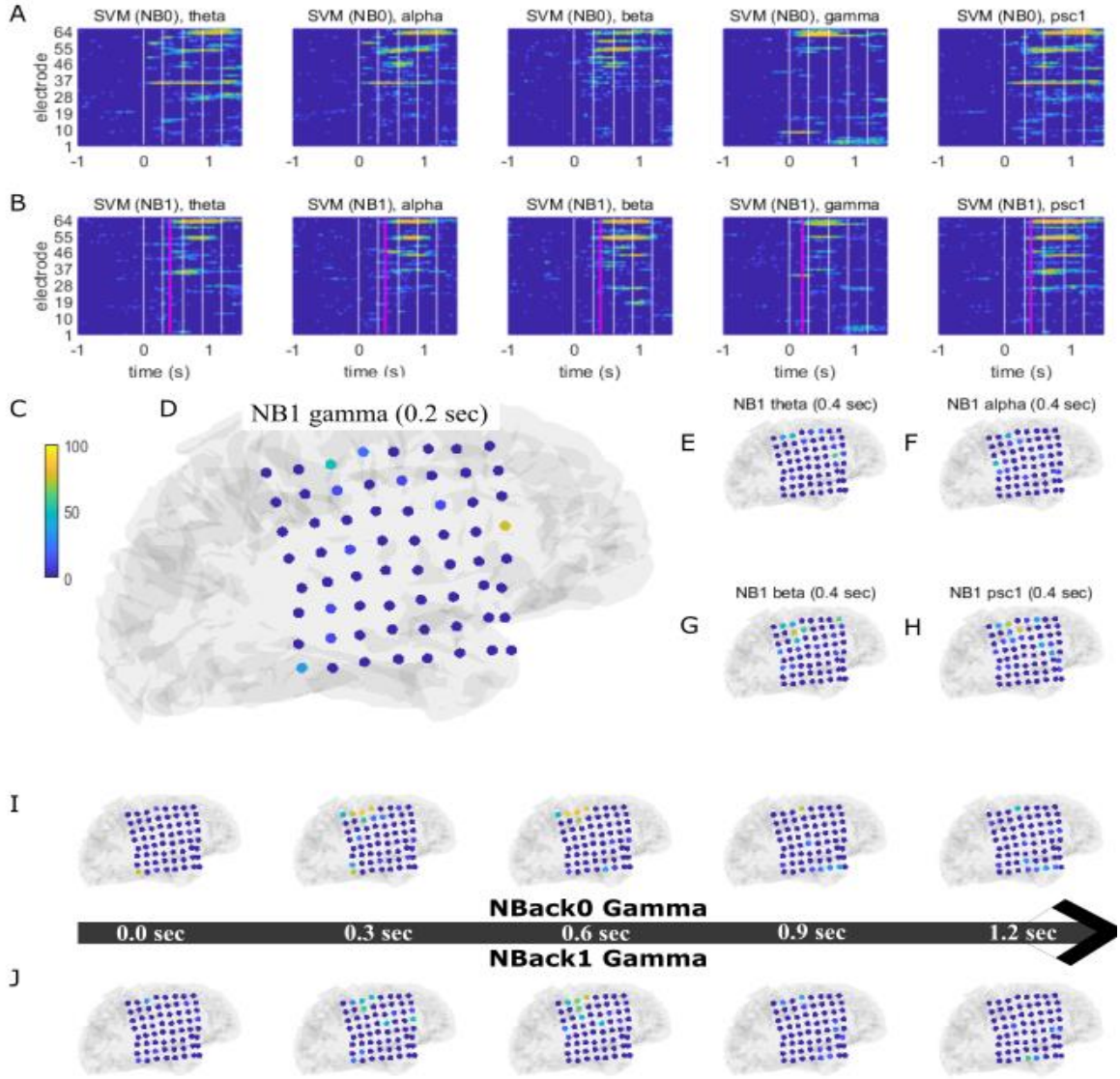

Figure 32 Subject CA - NBack match vs no match analysis. (A) and (B) show the SVM classification accuracy of the match vs no match successful trials over time from individual electrodes for theta, alpha, beta, gamma, and PSC1 of NBack0 (A) and NBack1 (B). (C) provides the legend indicating the decoding accuracy (%) utilized in this figure. (D) shows gamma classification accuracy of NBack1 match vs no match successful trials for each electrode on the cortex at time 0.2 sec (magenta vertical lines shown in (B)). (E)-(H) show the classification accuracy on the cortex at time 0.4 sec (magenta vertical lines shown in (B)) for theta (E), alpha (F), beta (G), and PSC1 (H). (I)-(J) show the gamma SVM classification accuracy per electrode at times 0.0 sec, 0.3sec, 0.6 sec, 0.9 sec, and 1.2 sec (white vertical lines shown in (A) and (B)) for NBack0 match vs no match successful trials (I), and NBack1 match vs no match successful trials (J).

template cortex using PSC1, and theta, alpha, beta, and gamma bands (Figures 31F, 31G, 31H, 31I, 31J respectively). As these figures show, the electrodes that have the most significant differences between task difficulty during the response are found in the premotor and prefrontal cortex (PFC) areas, especially for PSC1, theta, and alpha activity.

Using PSC1, we graphically displayed the classification accuracy on the cortex at different times during the trial (Figure 31K). It is noteworthy that certain electrodes (i.e., premotor area) exhibit activity that is significantly distinct between task difficulties at various times, both before and after the cue onset. The number of active electrodes peaks around the response time.

5.4.2 Analysis of NBack Match *vs* No Match trials (subject CA)

Another crucial aspect of the NBack task is the ability to decide if a cue matches the remembered one. Figures 32A-32B show the classification accuracy between match vs no match of all successful trials per electrode over time for NBack0 and NBack1 respectively (subject CA). As per previous analysis, SVM classification was set to 0% if the classes were not statistically different (p-value > 0.01). The results show that the electrodes involved in this decision are dependent on the task difficulty and the working memory requirement. A few electrodes showed significant differences between trials very quickly (i.e., NBack0 and NBack1 gamma), but most active electrodes could successfully classify the trials around the response time (windows starting 0.4 sec to 1.2 sec after cue onset). For this subject, the NBack0/NBack1 classification accuracy reached maximums of 82.0%/83.7% (theta), 83.9%/84.4% (alpha), 81.1%/87.3% (beta), 93.9%/80.9% (gamma) and 85.1%/88.4% (PSC1).

The gamma band feature, with the window starting 0.2 sec after cue onset, achieved the fastest

convergence to accurately classify 75% of the match versus no match trials (Figure 32D). Other features could be used to successfully classify the trials 0.4 sec after cue onset (Figures 32E, 32F, 32G, and 32H for theta, alpha, beta, and PSC1 respectively). Examining the gamma-related match *vs* no match classification accuracy over time for NBack0 and NBack1 (see Figures 32I-32J),

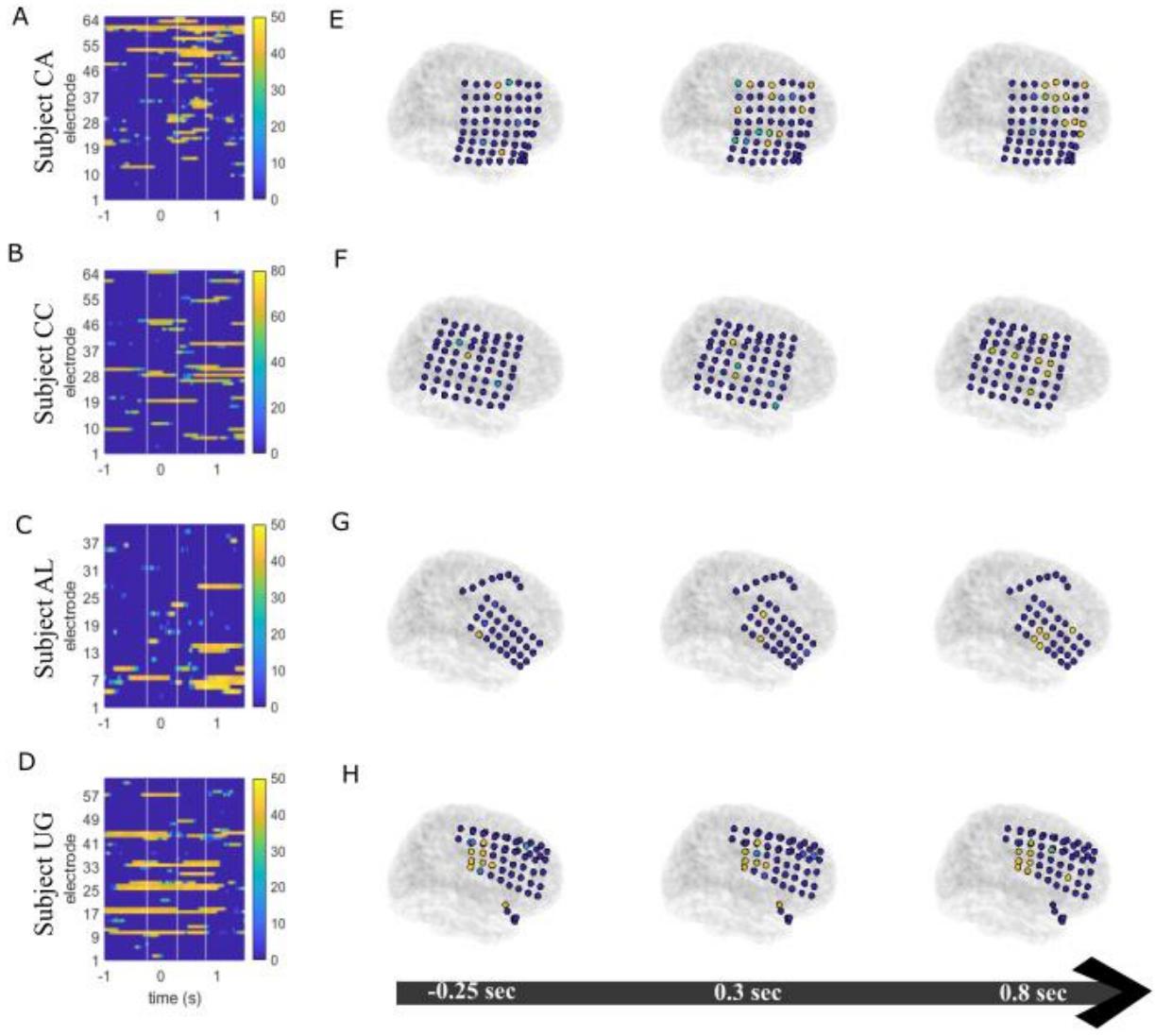

Figure 33 All Subject – PSC1 SVM classification of NBack task modality. The left column shows the PSC1 SVM classification accuracy of task difficulty from each electrode over time for subjects CA (A), AL (C), and UG (D) for classes: NBack0, NBack1, NBack2 and subject CC (B) for classes: NBack0, NBack1. (E), (F), (G), (H) show the task modality classification accuracy per electrode on the cortex at times -0.25 sec, 0.3sec, and 0.8 sec (white vertical lines shown in (A)-(D)) for subjects CA, CC, AL, and UG.

certain electrodes such as some from the premotor areas, achieved a high classification rate for both tasks. In contrast, some electrodes in the PFC areas, for example, show variability in

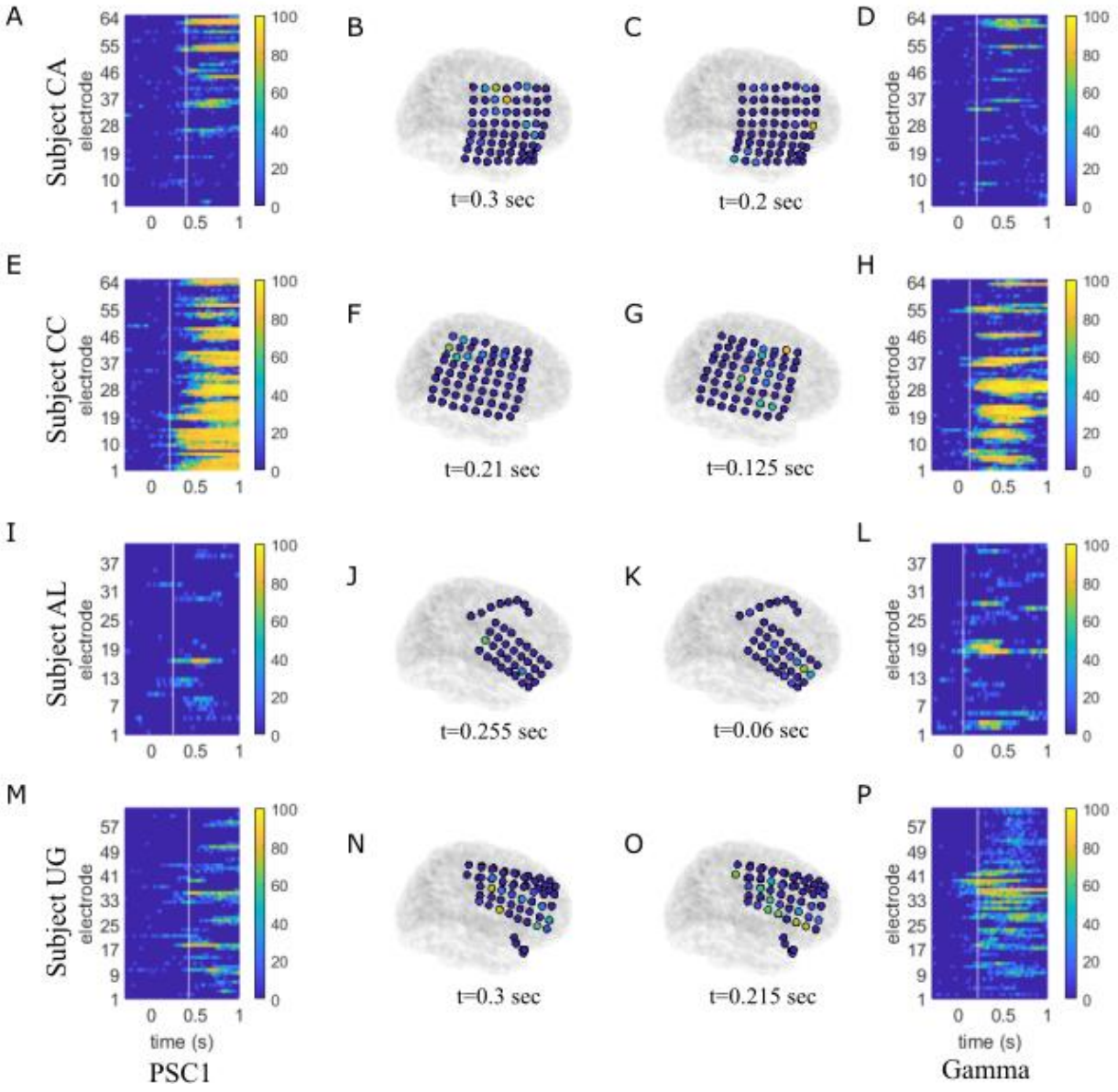

Figure 34 Match vs No Match classification. (A), (E), (I), and (M) show the SVM classification of NBack1 successful match vs no match trials using PSC1 for subjects CA, CC, AL, and UG respectively. (B), (F), (G), and (N) show the electrodes' PSC1 SVM classification accuracy at the time from cue onset when at least one electrode reached 75% for subjects CA, CC, AL, and UG. (C), (G), (K), and (O) show the electrodes' resulting gamma SVM classification accuracy at the time from cue onset when at least one electrode reached 75% for subjects CA, CC, AL, and UG. (D), (H), (L), and (P) show the SVM classification of NBack1 successful match vs no match trials using the gamma feature for subjects CA, CC, AL, and UG respectively.

classification performance based on the task difficulty level.

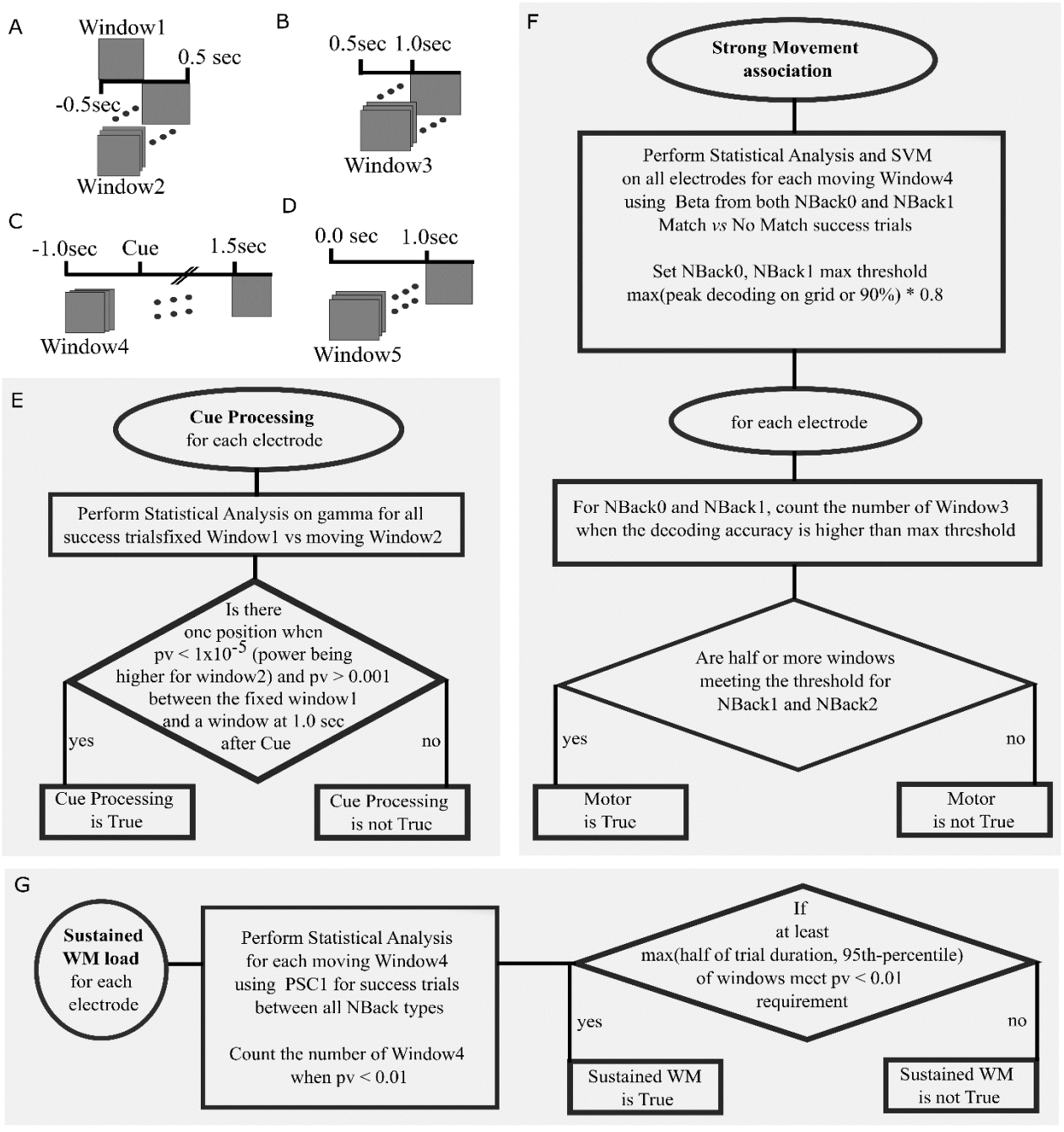

Figure 35 Identification of electrodes associated with cue processing, strong movement component, and sustained working memory load. (A), (B), (C), and (D) show the schematic of moving window timing used in the algorithms. (E) represents the flow chart used to identify electrodes involved in cue processing. (F) represents the flow chart used to identify electrodes strongly involved in movement. (G) represents the flow chart used to identify electrodes with sustained differences of activity depending on working memory load.

5.4.3 NBack Task Difficulty Analysis (all subjects)

Drawing insights from subject CA results, we opted to explore the classification of task difficulty for all subjects utilizing the PSC1 feature (Figure 33). For each moving window, we assessed the statistical differences between 3 classes (NBack0, NBack1, and NBack2 for subjects CA, AL, and UG) and 2 classes (NBack0, NBack1 for subject CC, refer to method section for further explanations). Figures 33A, 33B, 33C, and 33D illustrate the accuracy of NBack task difficulty level classification for individual electrodes, spanning the period from 1 sec to 1.5 sec after the cue onset. Several electrodes could classify above chance level (approximately 33%) at various points in time throughout the trial. The examination revealed that the time when decoding task difficulty was most actively undertaken for all subjects coincided with the response time.

We decided to visualize the electrodes involved in classifying the difficulty level of the NBack task using PSC1, given that this feature resulted in the highest number of electrodes proficient at this classification. This visualization was performed on the cortex model for each subject at various time points around the cue onset (-0.2 sec, 0.3 sec, and 0.8 sec). Figures 33E-33H illustrate some clusters of electrodes that are localized on the cortex (i.e., Figure 33H), some of the electrodes being involved before and after the cue onset.

5.4.4 Analysis of NBack Match *vs* No Match trials (all subjects)

To extend the analysis aimed at differentiating between successful match and no match trials for all subjects, and inspired by the results obtained for subject CA, we focused on the PSC1 and gamma features. The temporal evolution of each electrode classification accuracy using PSC1 is presented for subjects CA, CC, AL, and UG in Figures 34A, 34E, 34I, and 34M respectively. In

Figure 34, the second column (34B, 34F, 34J, and 34N for subjects CA, CC, AL, and UG) depicts

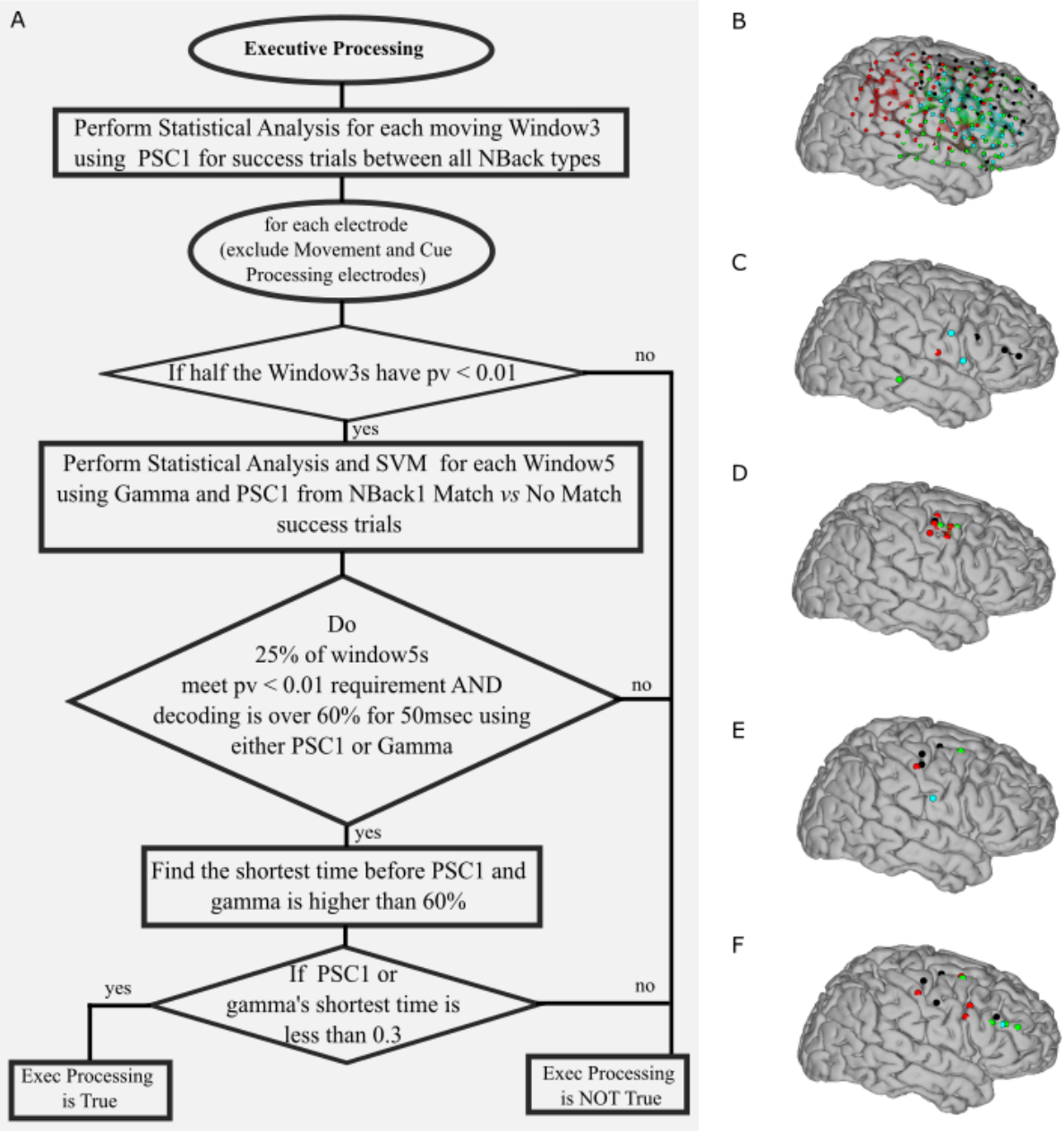

Figure 36 Identification of electrodes associated with cognitive activity functions. (A) represents the flow chart used to identify electrodes involved in executive working memory functions. (B) shows all analyzed electrodes for combined subjects on the standardized brain (CA (green), CC (red), AL (cyan), UG (black)). (C) identifies the cue processing electrodes for all subjects. (D) identifies the electrodes strongly associated with movement. (E) identifies the electrodes with sustained working memory load activity. (F) identifies the electrodes involved with executive memory functions.

the classification accuracy for each contact on the cortex model utilizing the PSC1 feature at the time when at least one electrode achieved a 75% classification accuracy. Correspondingly, the third and fourth columns present the classification accuracy results using the gamma feature (subjects CA, CC, AL, and UG in Figures 34C-34D, 34G-34H, 34K-34L, and 34O-34P respectively).

5.4.5 Cognitive Activity Location

Based on preceding analysis, algorithms were formulated to identify specific electrodes linked to cue processing (Figures 35A and 35E), movement (Figures 35B, 35C, and 35F), sustained activity variations contingent on the NBack task difficulty (Figures 35C and 35G), and executive working memory processing (Figures 35D and 36A).

In terms of cue processing, the algorithm is based on comparing the gamma power between a baseline window and windows around the cue onset. The electrodes implicated for all subjects (Figure 36C) were positioned on the ventral side of the grids, aligning with the visual perception pathway commonly referred to as the ventral stream (Coon and Schalk 2016).

To identify electrodes strongly associated with the flexing movement, our approach primarily relies on the efficacy of classifying matching trials, which necessitates movement, out of all successful trials using the beta feature. Predictably, the group of electrodes identified as significantly linked to the flexing movement was consistently situated around the hand knob area of the motor cortex for all subjects (Figure 36D).

Sustained working memory load activity was determined by monitoring the duration for which significant differences were detected in the PSC1 feature of no-match trials across different levels

of task difficulty. This threshold was established as the higher value between half of the trial

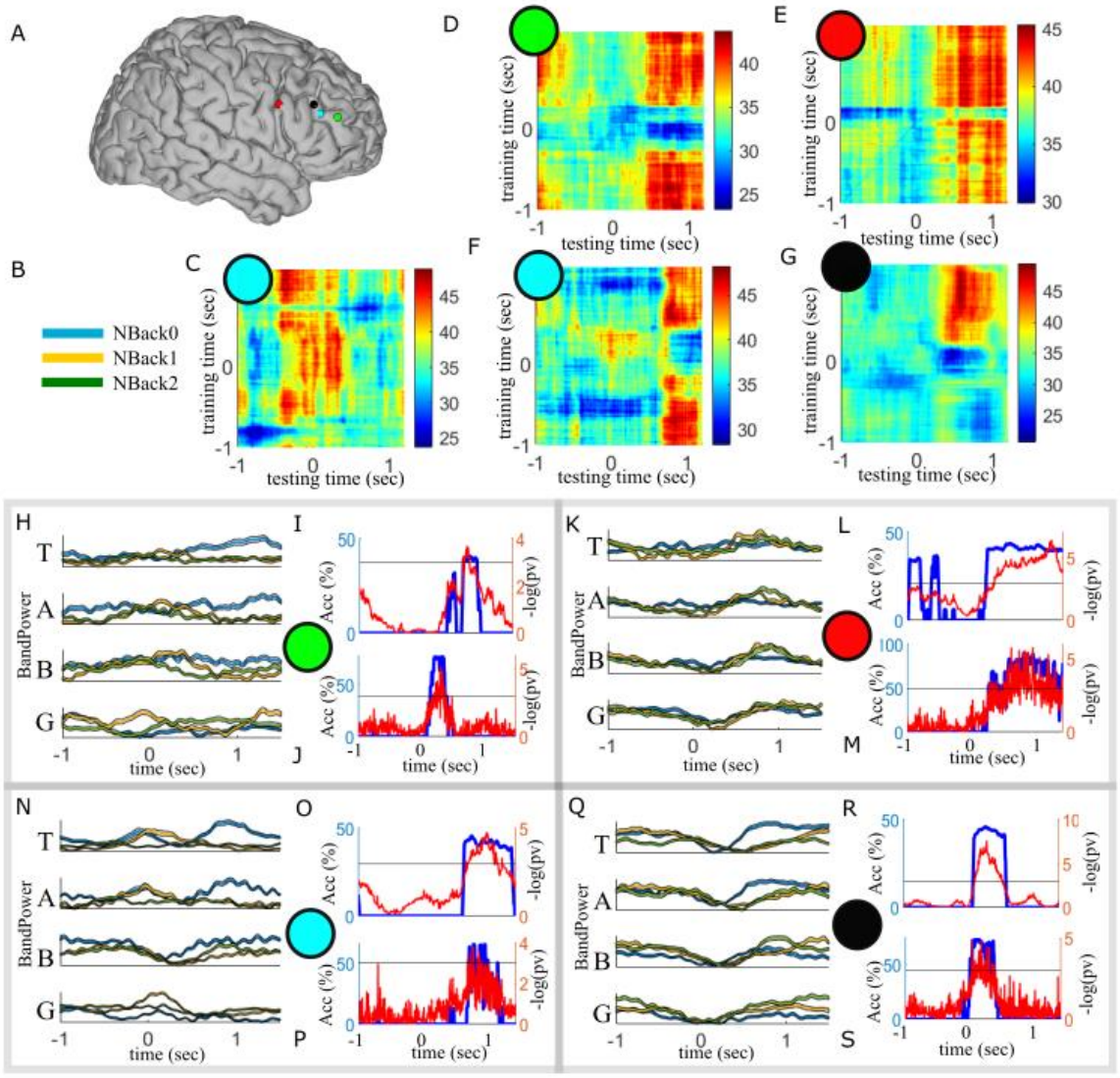

Figure 37 Selected electrodes analysis. (A) identifies the selected electrodes on the cortex for all subjects (CA (green), CC (red), AL (cyan), and UG (black)). (B) shows the color legend used to display the Band Power over time. (C)-(G) show the cross-temporal analysis where we trained an SVM model on classifying the successful no match trials from NBack0, NBack1, or NBack2, and tested the classification accuracy for individual trials at different times using a single feature set to gamma (C) or PSC1 (D)-(G). (H), (K), (N), and (Q) show for each selected electrode, the NBack0, NBack1, and NBack2 successful trials averaged theta, alpha, beta, and gamma power over time. (I), (L), (O), and (R) show the PSC1 classification accuracy for selected electrodes between NBack task types (blue) and the statistical significance (red, where the horizontal line is p-value = 0.001). (J), (M), (P), and (S) show the gamma classification accuracy of NBack1 match vs no match successful trials (blue) and the statistical significance (red, where the horizontal line is p-value = 0.001) for selected electrodes.

duration and a 95th percentile-based confidence interval of the dataset. The found electrodes engaged in sustained working memory load activity were clustered, predominantly concentrated in the postcentral region of the cortex near the hand knob (Figure 36E).

As detailed in the flow chart, the algorithm for identifying working memory executive functions involves evaluating the accuracy from SVM and the statistical differences in both, task difficulty and match *vs* no match trials. The electrodes linked to executive processing were not as spatially confined as the previously investigated activities, yet they yielded a more manageable set of locations for subsequent analysis (Figure 36F). Notably, a compact cluster of electrodes in the LPFC was selected as the focal point for our in-depth investigation.

5.4.6 Optimal MEA Implant Location

Examining the activity on the selected executive electrodes (Figure 37A), our initial step involved conducting a cross-temporal analysis. In this analysis, we trained an SVM model to classify successful no match trials among NBack0, NBack1, or NBack2. We subsequently tested the classification accuracy for individual trials using a single feature (gamma or PSC1) at various time points. The gamma classification results for the selected electrode from subject AL (Figure 37C) demonstrate notable stability of this feature around the cue onset. Figures 37D, 37E, 37F, and 37G depict the PSC1 outcomes of this analysis for the selected electrode on subjects CC, CA, AL, and UG respectively. These figures reveal some stability around the response, even when employing a model trained prior to the cue onset (subjects CA, CC, AL). However, a brief period around the cue proved challenging to accurately classify the task difficulty for all subjects.

The temporal evolution of averaged power in frequency bands for the no match successful trials

of NBack0, NBack1, and NBack2 was examined for each chosen electrode (refer to Figures 37H, 37K, 37N, 37Q). Apart from subject CA, where the chosen electrode was located more posteriorly, there is a consistent pattern of lower theta, lower alpha, and higher gamma power during more difficult tasks around the response phase.

Continuing with the in-depth analysis of selected electrodes, Figures 37I, 37L, 37O, and 37R portray the PSC1 classification accuracy between NBack task difficulty levels (depicted in blue) and the corresponding statistical significance (depicted in red, with the horizontal line representing a p-value of 0.001). The gamma classification accuracy of successful trials from NBack1 match *vs* no match is presented in Figures 37J, 37M, 37P, and 37S. Across all subjects, distinctions between the difficulty of the task and the NBack1 match *vs* no match classes are statistically significant following the cue onset.

5.5 Discussion

Our objective was to examine cognitive activities during the NBack task and identify the optimal location for a goal based iBCI implant. To achieve this, our initial step was to recognize changes in ECoG activity and associate them with the task requirement at different time points.

We analyzed the individual electrode average level of PSC1 and its power level for typical oscillatory band signals between NBack0, NBack1, and NBack2 task modalities. We noticed that many contact points on the grid are synchronized and peak around the response time of the experiment. For all task difficulties, the oscillations of the high-gamma frequency band were not as synchronized as the other bands and PSC1. The PSC1 level did not match one frequency band

for the duration of the trials but showed a similar pattern of activity with different bands at different times (i.e., theta during and after response, beta around response time).

Examining the potential SVM classification of task difficulty using a single feature for each electrode on all four subjects, we discovered that the PSC1 feature allowed for the most effective discrimination, with certain electrodes contributing for over 50% of the trial duration. The analysis revealed that the period during which discriminating the task difficulty engaged the highest number of electrodes corresponded with the response time. The ability to discriminate task difficulty levels does not necessarily imply that the contact is engaged in executive functions of working memory and decision-making. Instead, it could be associated with behavioral changes, such as heightened stress and attention, or variations in motor and eye movements.

To identify the electrodes implicated in decision-making, working memory, or movement preparation processes, we examined the classification of the match vs no match successful trials at a specific task difficulty level. We utilized the NBack1, as this task involves working memory, and across all subjects, we had at least 11% of the successful trials belonging to the matching class. This analysis showed that certain electrodes could successfully classify match vs no match trials shortly after the cue presentation, by using the gamma band feature. While other frequency bands and the PSC1 feature would allow some electrodes to also achieve high classification rates, their success occurred later, closer to the response epoch.

Based on findings from the preceding analysis, algorithms were formulated to identify the brain ECoG contacts associated with distinct activities, including cue processing, flexing movement, sustained working memory load, and the executive functions of working memory. As expected, our observations showed that electrodes in the visual perception pathway (for the subjects who

had contacts in this area) were engaged in early cue processing. By analyzing beta frequency band activity, we were able to locate the electrodes associated with hand flexing movement in the hand knob area across all subjects. The electrodes which showed significant differences between task difficulty levels throughout the trials were primarily situated in the postcentral area around the hand knob region. This observation suggests a potential indication that the subjects' motor and sensory processing may vary based on stress levels or changes in attention, depending on the modality. Our algorithm, designed to locate electrodes involved in the executive functions of working memory, primarily identified electrodes in and around the hand knob of the motor cortex, as well as in the PFC regions of the brain. Notably when visualizing all subjects on the same template brain model, a cluster of electrodes for most subjects was detected in the dorsolateral PFC which were the electrodes selected for the more detailed analysis.

During more challenging tasks around the response epoch, the selected electrodes exhibited a consistent pattern of reduced theta and alpha power, coupled with elevated gamma power. Leveraging the gamma feature, these electrodes demonstrated the ability to discern, shortly after cue presentation, whether the given cue matched the remembered one for the trials in NBack1 task modality. Furthermore, the cross-temporal SVM classification of task difficulty, utilizing the PSC1 feature, displayed some stability when the model was tested with time points following the cue presentation.

In the context of an iBCI programmed to use goal encoding factors, we determined that the chosen electrodes in the dlPFC would offer the most advantages and serve as an optimal location for an MEA implant. This discovery aligns with existing literature that links this region to various

cognitive functions in the NBack task (Owen et al. 2005), including the manipulation of working memory (Owen, 1997) and response selection (Rowe et al. 2000).

5.6 References

[1] Ajiboye AB, Willett FR, Young DR, Memberg WD, Murphy BA, Miller JP, et al. Restoration of reaching and grasping movements through brain-controlled muscle stimulation in a person with tetraplegia: a proof-of-concept demonstration. The Lancet [Internet]. 2017;389(10081):1821–30.

[2] Al-qaysi, ZT, Zaidan, BB, Zaidan, AA, & Suzani, MS. A review of disability EEG based wheelchair control system: Coherent taxonomy, open challenges and recommendations. Computer Methods and Programs in Biomedicine. 2018;164:221–237.

[3] Andersen RA, Aflalo T, Kellis S. From thought to action: The brain-machine interface in posterior parietal cortex. Proceedings of the National Academy of Sciences of the United States of America. 2019 Dec 26;116(52):26274–9.

[4] Andersen RA, Cui H. Intention, action planning, and decision making in parietal-frontal circuits. Neuron. 2009 Sep 10;63(5):568-83.

[5] Baddeley A. Working memory. Current Biology. 2009;20(4):136–40.

[6] Benabid AL, Costecalde T, Eliseyev A, Charvet G, Verney A, Karakas S, et al. An exoskeleton controlled by an epidural wireless brain-machine interface in a tetraplegic patient: a proof-of-concept demonstration. The Lancet Neurology [Internet]. 2019 Oct;0(0).

[7] Brzezicka A, Kamiński J, Reed CM, Chung JM, Mamelak AN, Rutishauser U. Working memory load-related theta power decreases in dorsolateral prefrontal cortex predict individual differences in performance. Journal of cognitive neuroscience. 2019 Sep 1;31(9):1290-307.

[8] Boulay CB, Pieper F, Leavitt M, Martinez-Trujillo J, Sachs AJ. Single-trial decoding of intended eye movement goals from lateral prefrontal cortex neural ensembles. Journal of Neurophysiology. 2016;115(1):486–99.

[9] Collinger JL et al. High-performance neuroprosthetic control by an individual with tetraplegia. Lancet. 2013; 381:557-564.

[10] Coon WG, Schalk G. A method to establish the spatiotemporal evolution of task-related cortical activity from electrocorticographic signals in single trials. Journal of Neuroscience Methods. 2016;271(1):76–85.

[11] Fan RE, Chang KW, Hsieh CJ, Wang XR, Lin CJ. LIBLINEAR: A library for large linear classification. Journal of Machine Learning Research. 2008;9:1871–4.

[12] Flint, RD, Lindberg EW, Jordan LR, Miller, LE, & Slutzky, MW. Accurate Decoding of Reaching Movements from Field Potentials in the absence of Spikes. Journal of Neural Engineering. 2012;9(4),1–22.

[13] Gold JI, Shadlen MN. The neural basis of decision making. Annual Review of Neuroscience. 2007;30:535–74.

[14] Hosman T, Hynes JB, Saab J, Wilcoxen KG, Buchbinder BR, Schmansky N, et al. Auditory cues reveal intended movement information in middle frontal gyrus neuronal ensemble activity of a person with tetraplegia. Scientific Reports [Internet]. 2021 Dec 11;11(1):98.

[15] Johnston R, Doucet G, Boulay C, Miller K, Martinez-Trujillo J, Sachs A. Decoding Saccade Intention from Primate Prefrontal Cortical Local Field Potentials Using Spectral, Spatial, and Temporal Dimensionality Reduction. International Journal of Neural Systems. 2021;31(6):1–19.

[16] Lundqvist M, Rose J, Herman P, Brincat SLL, Buschman TJJ, Miller EKK. Gamma and Beta Bursts Underlie Working Memory. Neuron [Internet]. 2016;90(1):152–64. Available from: http://dx.doi.org/10.1016/j.neuron.2016.02.028

[17] Manning JR, Jacobs J, Fried I, Kahana MJ. Broadband shifts in local field potential power spectra are correlated with single-neuron spiking in humans. Journal of Neuroscience. 2009;29(43):13613–20.

[18] Mendoza-Halliday D and Martinez-Trujillo JC. Neuronal population coding of perceived and memorized visual features in the lateral prefrontal cortex. Nature Communications. 2017;8:1–13.

[19] Miller EK, Erickson CA, Desimone R. Neural mechanisms of visual working memory in prefrontal cortex of the macaque. Journal of neuroscience. 1996 Aug 15;16(16):5154-67.

[20] Miller EK, Lundqvist M, Bastos AM. Working Memory 2.0. Neuron. 2018;100(2):463–75.

[21] Miller KJ. A library of human electrocorticographic data and analyses. Nat. Hum. Behav. 2019;3:1225–35.

[22] Miller KJ, Honey CJ, Hermes D, Rao RPN, denNijs M and Ojemann JG. Broadband changes in the cortical surface potential track activation of functionally diverse neuronal populations. NeuroImage. 2014;85:711–720.

[23] Miller KJ, Makeig S, Hebb AO, Rao RP and Ojemann, JG. Cortical electrode localization from X-rays and simple mapping for electrocorticographic research: The "Location on Cortex"(LOC) package for MATLAB. Journal of neuroscience methods. 2007;162(1-2): 303-308.

[24] Miller KJ, Zanos S, Fetz EE, denNijs M, and Ojemann, JG. Decoupling the cortical power spectrum reveals real-time representation of individual finger movements in humans. Journal of Neuroscience. 2009; 29(10): 3132–3137.

[25] Owen AM. The functional organization of working memory processes within human lateral frontal cortex: The Contribution of Functional Neuroimaging. European Journal of Neuroscience. 1997;9(2):1329–39.

[26] Owen AM, McMillan KM, Laird AR, Bullmore E. N-back working memory paradigm: A meta-analysis of normative functional neuroimaging studies. In: Human Brain Mapping. 2005. p. 46–59.

[27] Pandarinath C, Nuyujukian P, Blabe CH, Sorice BL, Saab J, Willett FR, et al. High performance communication by people with paralysis using an intracortical brain-computer interface. eLife [Internet]. 2017 Feb 21;6.

[28] Roux F, Uhlhaas PJ. Working memory and neural oscillations: Alpha-gamma versus theta-gamma codes for distinct WM information? Trends in Cognitive Sciences. 2014;18(1):16–25.

[29] Roux F, Wibral M, Mohr HM, Singer W, Uhlhaas PJ. Gamma-band activity in human prefrontal cortex codes for the number of relevant items maintained in working memory. Journal of Neuroscience. 2012;32(36):12411–20.

[30] Rouzitalab A, Boulay CB, Park J, Martinez-Trujillo JC, & Sachs AJ. Ensembles code for associative learning in the primate lateral prefrontal cortex. Cell Reports. 2023;42(5).

[31] Rowe JB, Toni I, Josephs O, Frackowiak RSJ, Passingham RE. The prefrontal cortex: response selection of maintenance within working memory? 2000;288(June):1656–60.

[32] Santhanam G, Ryu SI, Yu BM, Afshar A, Shenoy K V. A high-performance brain-computer interface. Nature. 2006;442(7099):195–8.

[33] Shanechi MM, Wornell GW, Williams ZM, Brown EN. Feedback-controlled parallel point process filter for estimation of goal-directed movements from neural signals. IEEE Transactions on Neural Systems and Rehabilitation Engineering. 2013;21(1):129–40.

[34] Smith EE, Jonides J. Storage and executive processes in the frontal lobes. Science. 1999;283:1657–61.

[35] Tremblay S, Doucet G, Pieper F, Sachs A, and Martinez-Trujillo J. Single-trial decoding of visual attention from local field potentials in the primate lateral prefrontal cortex is frequency-dependent. Journal of Neuroscience. 2015;35(24):9038–9049.

[36] Vansteensel MJ, Hermes D, Aarnoutse EJ, Bleichner MG, Schalk G, Van Rijen PC, et al. Brain-computer interfacing based on cognitive control. Annals of Neurology. 2010;67(6):809–16.

[37] Willett FR, Avansino DT, Hochberg LR, Henderson JM, Shenoy KV. High-performance brain-to-text communication via handwriting. Nature. 2021 May 13;593(7858):249-54.

Chapter 6

Discussion and Conclusion

6.1 Discussion

Brain-computer interface research is rapidly evolving towards robust and reliable real-time decoding of brain signals. The usual method to decode volitional movements is to extract parameters from single-neuron responses or from the population of neurons in the motor cortex (Shenoy et al. 2013). With the evolution in adaptive computer technology such as neuroprosthetic and intelligent wheelchairs, another option is to decode the goal of a BCI user to control these devices using the overall intention of the action (Andersen et al. 2012).

A possible BCI system with implants in prefrontal and motor cortices, could decode the user's intention based on, for example, the attended object in working memory correlated with motor execution activity. It would then start the activation of the prosthetic controller which would initiate and monitor the movement. The brain activity of the user would provide feedback to the prosthetic controller, mainly detecting if it is moving in the desired direction, by evaluating if the intention is still applicable and if the goal is being fulfilled.

The lateral prefrontal cortex has been associated with many of these goal encoding factors and was deemed a suitable signal source for a goal selective cognitive BCI (Boulay et al. 2016). Multiple behavioral studies on macaques have characterized local field potential (LFP) signals and spike activity of the neurons in this brain region but none in humans. However, there is strong homology in area 8A between primates, suggesting similar functional roles in humans could be expected.

Understanding the anticipated patterns of brain activity during tailored cognitive tasks can aid in

localizing a precise brain region where decoding factors such as target intention, spatial location, decision-making, and working memory is feasible. Future research should explore how different goal variables can be integrated to identify a BCI user's objective. The results presented in this thesis were all based on recorded sessions following specific and known task conditions. Analyzing task-independent states in more natural scenarios would be beneficial for integrating the proposed decoding methods into iBCI systems. Additionally, it would also be valuable to compare patterns of LFP-based activity at different spatial resolution, from EEG, ECoG, sEEG, and MEA electrodes.

6.2 Conclusion

The first chapter of this thesis provided the foundational knowledge essential for understanding the subsequent content. Following chapters delved into investigating the potential to use extracellular voltage fluctuations, in the form of local field potentials from the prefrontal cortex of primates, to decode both, saccade target intentions (Chapter 2), and saccade locations within a virtual maze (Chapter 3). These decoded factors could prove invaluable in a BCI system, providing essential data to steer an assistive device or an intelligent wheelchair.

After demonstrating the potential to decode valuable factors for controlling an assistive device from the prefrontal cortex of non-human primates (Chapters 2-3), we aimed to develop a method to precisely identify the optimal MEA position to maximize information about the user's intended action. A significant portion of this thesis's effort was intended for use during the NCC clinical trial (section 1.8.2), primarily to determine the optimal MEA implant locations in the prefrontal and motor cortices. The plan involved using microECoG electrodes to record brain activity associated with cognitive functions during the intraoperative phase of the trial. The

characterization and localization analysis of the brain activity would ultimately determine the best possible implant placements for a goal-based iBCI system. Due to recruiting difficulty causing delays in the NCC trial, the methodology, including signal processing tools to characterize and localize cognitive activity, was developed using EEG, sEEG (Chapter 4), and then validated with ECoG data (Chapter 5). It is now ready for use during the clinical trial when needed.

Deciphering the intended action of a BCI user is a complex challenge that involves the extraction and integration of cognitive factors. These factors include movement planning, working memory, visual spatial attention, and the decision state, collectively offering valuable insights into the user's anticipated action. Chapter 4 described a set of cognitive tasks and signal processing tools designed to explore and characterize brain activity. Examining LFPs from EEG and sEEG electrodes of participants engaged in tailored cognitive tasks showed the possibility to identify the electrodes involved in cognitive activity related to working memory, visual spatial attention, and delayed saccade tasks. The last chapter validated the methodology using the open-source library of human electrocorticographic data. This concluding analysis demonstrated the feasibility of utilizing ECoG signals to identify the specific electrodes modulated by cognitive activity associated with cue processing, movement execution, and executive functions related to working memory. Devoting time in meticulous preparation to identify the optimal brain regions for BCI implant locations will increase the likelihood of rich signal outcomes, thereby improving the overall BCI user experience.

6.3 References

[1] Andersen RA, Aflalo T, Bashford L, Bjanes D, Kellis S. Exploring Cognition with Brain-Machine Interfaces. Annual Review of Psychology. 2022;73:131–58.

[2] Boulay CB, Pieper F, Leavitt M, Martinez-Trujillo J, Sachs AJ. Single-trial decoding of intended eye movement goals from lateral prefrontal cortex neural ensembles. Journal of Neurophysiology. 2016;115(1):486–99.

[3] Shenoy KV, Sahani M, Churchland MM. Cortical control of arm movements: A dynamical systems perspective. Annual Review of Neuroscience. 2013;36:337–59.